©Copyright 2017
Mark Jankauski

Dynamic Modeling of Insect Flight Mechanisms

Mark Jankauski

A dissertation
submitted in partial fulfillment of the
requirements for the degree of

Doctor of Philosophy

University of Washington

2017

Reading Committee:

I-Yeu (Steve) Shen, Chair

Sawyer Fuller

Thomas Daniel

Program Authorized to Offer Degree:
Mechanical Engineering

University of Washington

Abstract

Dynamic Modeling of Insect Flight Mechanisms

Mark Jankauski

Chair of the Supervisory Committee:
Professor I-Yeu (Steve) Shen
Department of Mechanical Engineering

A dynamic model of an insect wing is developed treating the wing as a deformable body subject to three-dimensional finite rotation about a fixed point at the base of the wing. Discretization of a stationary wing is conducted via finite element analysis to determine the natural frequencies and mode shapes. By formulating and discretizing the kinetic and potential energy, the equation of motion governing the modal response of a flapping wing is derived using Lagrange's equation. The equation of motion indicates Coriolis, Euler, and centrifugal forces resulting from the finite rotation are responsible for the wings elastic deformation. Numerical integration reveals a beat phenomenon that arises from the Coriolis excitation in the first vibration mode. The beat phenomenon is insensitive to yaw amplitudes and non-zero initial conditions but diminishes in the presence of damping. The beat phenomenon can potentially be used to estimate gyroscopic forces.

Then, a two-axis rotation stage was constructed to replicate the large amplitude rotations of an insect wing and verify the inertial-elastic wing model. A wing was constructed with a strain gage mounted near the root to measure temporal strain. Single-axis rotations were considered, and multi-axis rotations were investigated to exploit phenomena related to geometric coupling. Experiments were conducted in air and vacuum to decouple aerodynamic and inertial-elastic forces. Aerodynamic forces constituted maximally 15% of the strain, suggesting the inertial-elastic model is appropriate in certain contexts. Inertial forces

were dominant in the pitch-roll and roll-yaw configuration, whereas gyroscopic forces were dominant in the pitch-yaw configuration. Theoretic predictions match experimental results fairly well. The inertial-elastic rotating model may be used to inform flapping wing micro aerial vehicle designers moving forward, particularly in the design of strain-based control systems.

Next, the relative role of aerodynamic and inertial moments on insect steering is investigated. Maneuvering in both natural and artificial miniature flying systems is assumed to be dominated by aerodynamic phenomena. To explore this, I develop a flapping wing model integrating aero and inertial dynamics. The model is applied to a semi-elliptical wing modeled after the forewing of the Hawkmoth *Manduca sexta* and realistic kinematics are prescribed. Stroke deviation phase is critically explored, as it relates to firing latency in insect steering muscles which has been correlated to various aerial maneuvers. Average resultant force production acting on the body predominately arises from wing pitch and roll and is insensitive to the phase and amplitude of stroke deviation. Inclusion of stroke deviation can generate significant averaged aerodynamic torques at steady-state and adjustment of its phase facilitates body attitude control. These claims are supported by biological evidence, where unilateral or symmetric actuation of steering muscles caused body pitching or banked turns in flying insects [1, 2]. Moreover, wing angular momentum varies with stroke deviation phase, implying a non-zero impulse during a time-dependent phase shift. Simulations show wing inertial and aerodynamic impulses are of similar magnitude during short transients whereas aerodynamic impulses dominate during longer transients. Additionally, inertial effects become less significant for smaller flying insects. Body yaw rates arising from these impulses are consistent with biologically measured values. Thus, I conclude (1) modest changes in stroke deviation can significantly affect steering and (2) both aerodynamic and inertial torques are critical to maneuverability, the latter of which has not widely been considered. Therefore, the addition of a control actuator modulating stroke deviation may decouple lift/thrust production from

steering mechanisms and provide inertial shaping benefits in flapping wing micro aerial vehicles.

Lastly, the effect of wing structural compliance on power expenditures in insect flight is characterized. I use the previously derived elastic structural wing model and rigid blade-element aerodynamic model. Inertial instantaneous power is derived by differentiating the sum of the kinetic and potential energy with respect to time. Aerodynamic instantaneous power is calculated by the dot product of the prescribed angular velocity vector with the determined aerodynamic moments. A simple case of a wing undergoing a single, small-amplitude rotation in vacuum is first considered. For this case, a large portion of the rigid power is abated by elastic power, thereby significantly reducing overall energetic requirements. The model is subsequently applied to a more realistic case of a wing undergoing three-dimensional rotation in air. An optimization routine determines optimal wing kinematics and fundamental frequency such that root-mean-square power is minimized and sufficient lift for hover is produced. The optimizer accurately predicts roll and stroke deviation amplitude compared to biologically measured values of the Hawkmoth *Manduca sexta* [3]. The optimized pitch amplitude was approximately 20° different from measured values; this discrepancy was attributed to the torsional flexibility of the wing, unaccounted for in the rigid aerodynamic model. Using the optimized parameters, our simulation suggests an elastic wing requires approximately 25% less power compared with a completely rigid wing. This suggests micro aerial vehicle wings have an power-minimizing optimal natural frequency, which can be readily tuned through conciseness wing design.

TABLE OF CONTENTS

LIST OF FIGURES

ACKNOWLEDGMENTS

This material is based upon work supported by the National Science Foundation under Grant No. CMMI-1360590. Any opinions, findings, and conclusions or recommendations expressed in this material are those of the authors and do not necessarily reflect the views of the National Science Foundation.

DEDICATION

To my family, for their unwavering love and support. To my friends, for sharing with me both the good times and the hard times. And lastly, to my loyal dog, Rajon, who has spent countless hours by my side, both in work and in play.

Chapter 1

INTRODUCTION

Micro aerial vehicles (MAVs) have garnered significant interest over the past few decades. The myriad of MAV applications appears limitless, including monitoring resource allocation on farms, rendering 3D maps of rapidly changing environments, tracking real-time development of tropical storms and performing autonomous package delivery [4, 5, 6, 7]. MAVs are relatively small and quiet, are capable of performing aggressive aerial maneuvers or stationary hovering, and are comparatively inexpensive versus their larger counterparts. These characteristics make them suitable candidates for indoor surveillance and reconnaissance missions, where discretion is paramount [8, 9, 10]. Consequently, the advancement of MAV technology is of considerable interest to various military branches.

Presently, there are a variety of MAV designs available which are typically categorized by lift production mechanisms. Some configurations use a single or multiple rotating blades (helicopters or quadcopters) while other configurations rely on traditional fixed wings to generate lift [11]. Other designs have experimented with balloons or reservoirs filled with gases lighter than air [12]. Recently, flapping-wing type micro air vehicles (FWMAVs) have become more prevalent, with notable examples being the Festo Smartbird, TU Delft Delfly, Aeroenvironment Nanohummingbird, and the Harvard Robobee [13, 14, 15, 16]. While the energy efficiency of fixed versus flapping wing MAVs is debated, flapping wing MAVs have other distinct advantages [17, 18, 19].

Perhaps the most marked advantage of the flapping-wing MAV is the capacity to be scaled to minuscule sizes. For traditional fixed wing MAVs, viscous forces tend to dominate lift forces at low Reynold's number, an inefficiency that establishes a lower bound on the attainable length scale [19]. Moreover, most small rotor-based fliers employ DC motors which

become inefficient at reduced scales due to increased heating in electromagnetic coils [20]. Coulomb frictional effects also scale with rotor surface area, which implies a large amount of friction per unit mass for small-scale rotor-based MAVs. Flapping-wing vehicles are also generally more maneuverable than the rotor-based aircraft; rotor-based vehicles may introduce a lag when performing aerial maneuvers due to spin-up/spin-down of motors.

On the other hand, nature has consistently demonstrated the feasible length scale for flapping wing insects is much smaller – members of the Mymaridae family have body lengths as small as 0.5 mm [21]. However, there are many challenges that accompany designing a flapping-wing MAV at insect scales, largely due to reduced payload capacity. In many cases, current battery and sensor (accelerometers, gyroscopes, cameras, etc.) technology are prohibitively massive, and traditional sensors cannot reliably produce high-fidelity signals due to severe operation conditions [22, 15, 23]. Moreover, on-board sensors may constitute a significant portion of the MAV total energy consumption. These challenges illuminate the necessity to optimize nearly every facet of the vehicle, including actuators, sensors, and structural components.

Inspiration from biology may help overcome some of these challenges of scaling. Flying insects are remarkably adept fliers, capable of performing agile maneuvers while effortlessly correcting for disturbances such as gusts of wind [24]. Due to their masterful flight, insects frequently serve as inspiration for engineered designs. The mechanics of wings, the mechanisms of actuation, energy storage, and sensorimotor control have all provided guidance for a range of engineered systems. For instance, the Harvard Robobee, boasting a total mass of 80 mg and wingspan of only 3 cm, was designed using the Diptera (true flies) as inspiration [25]. The robot is supplied power through tethers and is most reliably controlled using off-board visual tracking.

Much of this dissertation focuses on the insect forewing, a highly evolved structure that serves a variety of purposes. Flapping wings generate lift and thrust, the aerodynamic forces necessary for flight. However, describing the complicated mechanics of a flapping wing is a challenging task. As the wing flaps it undergoes structural deformation from

both aerodynamic and inertial-elastic loads [26]. This structural deformation positively influences aerodynamic performance, suggesting compliant wings may be beneficial to MAV performance [27]. Moreover, deformation induces significant temporal strains, which in turn activate mechanosensory cells distributed throughout the insect wing. Many researchers speculate this mechanosensory feedback provides information necessary to identifying flight status [28]. In particular, mechanosensory feedback may be essential in identifying body angular rates of rotation. Should an insect be able to interpret and react to strains induced by body rotations, they may be able to stabilize themselves in these presence of external perturbations such as wind gusts. Some insects, such as the housefly, have well-documented gyroscopic sensing organs called halteres [29]. Halteres are club-like structures attached to the thorax that are known to have evolved from hindwings. However, insects such as moths and butterflies do not have halteres which engenders the question – how does this class of insect receive analogous sensory information? The answer may lie within the mechanosensory cells of the forewing and hindwing.

In addition to better understanding the dynamics of an insect wing, studies surrounding the insect drivetrain may also help elucidate the physical principals governing flight. In most insects, the gross wing motion is generated by two sets of primary flight muscle sets in the thoracic cavity, termed dorsal longitudinal muscles (DLMs) and dorso-ventral muscles (DVMs) [30]. These muscles deform the thorax and, through a complex wing hinge system, indirectly actuate wings [31]. The DLMs drive wing down-strokes whereas the DVMs drive wing elevation. There is recent evidence that some control authority resides in these powerful flight muscles [32]. However, the dominant paradigm for control is thought to be relegated to small steering muscles that modify the wing trajectory by changing the articulation of the wing hinge, with the DLMs and DVMs providing the bulk of the power. This unique anatomical structure gives rise to an appealing hypothesis – perhaps gross wing motion is controlled by the power flight muscles whereas steering muscles fine-tune wing kinematics to induce aerial maneuvers. Thus, in this dissertation, I attempt to answer the question – how do small muscles produce large changes in body kinematics?

Furthermore, a detailed understanding on the insect drive train offers insight into the energetic requirements of flight. The thorax, wing and wing hinge all deform substantially during flight, storing potential energy in the process. This potential energy can be recruited to accelerate or decelerate the wing, thereby reducing the inertial costs associated with flapping [33, 34]. In fact, absent of elastic storage, flapping wings are conjectured to be no more efficient than rotating propellers [35]. It seems plausible FWMAV roboticists could develop biologically-inspired drivetrains, exploiting compliant components and elastic energy storage mechanisms to mitigate power consumption and extend flight time through improved battery life. However, we must first better understand how structural compliance affects energetic expenditures in flight.

Thus, there remain several open questions in regards to insect flight. The aim of this work is not only to better understand the mechanics of insect flight, but to extend the findings towards the enhancement of insect-scale MAVs. The remainder of this document is organized as follows. First, we develop a reduced-order model characterizing the dynamic response of a flapping, flexible insect wing. Next, we conduct experimental studies to validate the elastic flapping-wing model using a custom rotation stage in and out of vacuum conditions. We then derive an integrated aerodynamic/inertial-elastic model to investigate the relative contribution of inertial and aerodynamic moments to insect steering maneuvers. Lastly, we explore the effect of wing compliance on flight power requirements. Each chapter contains a stand-alone introduction and literature review relevant to the topics discussed in that chapter.

Chapter 2

INERTIAL-ELASTIC WING MODEL FORMULATION

Fully characterizing the deformation and corresponding strains of a flapping wing is difficult. The inherent unsteady flow of air around the wing makes a computational fluid dynamic (CFD) model computationally rigorous, particularly when considering fluid-structure interaction. As a result, researchers have employed two-dimensional models of the wing to garner physical insight into both aerodynamic performance and wing deformation. However, such models cannot fully explore physical phenomena that may be inherent to the fully three-dimensional rotating structure.

These constraints render a high-fidelity wing model including both aerodynamic and inertial-elastic loads impractical. However, should aerodynamic forces be negligible compared to inertial-elastic forces, a dynamic model of the forewing may be more easily realized. In an effort to identify the contribution of each force on structural deformation, Combes and Daniel performed an experiment in which they actuated the wings of a Hawkmoth *Manduca sexta* in both air and in helium (15% the density of air) [26]. They found the overall deformation was only modestly affected, suggesting the bending of the wing was predominately due to inertial-elastic forces.

Leveraging this assumption, this chapter focuses on developing an inertial-elastic wing model treating the wing as an elastic body subject to three-dimensional rotation. This chapter is organized as follows. First, existing kinematic and dynamic models of the forewing are described. Then, a newly proposed dynamic model is formulated using Lagrange mechanics. The model is applied to a fictitious *Manduca sexta* forewing, revealing a beat phenomenon in the first two modes caused by the interaction of gyroscopic and centrifugal forces with the free vibration of the wing. Various factors that may affect the presence of the beat phenomenon

are investigated, including initial conditions, yaw rotation amplitude, and damping. Lastly, the physical implications of these findings are discussed.

2.1 Existing and Proposed Models

Several models have previously been developed to describe the complex dynamics of an insect wing during flight. Many kinematic and dynamic models treat the insect body and wings as several connected rigid bodies. For example, a kinematic model developed by Roccia et al.[11] treats the wing as a rigid body subject to three-dimensional rotation about a fixed point on the insect body. An alternative dynamic model developed by Orlowski and Girard also treats the insect forewing as a rigid body, and considers aerodynamic loading as a generalized force acting on the wing [36]. Such kinematic and dynamic models can be used to effectively estimate wing velocity and aerodynamic force production while retaining a lower number of degrees of freedom. By treating the wing as a rigid body, such models are unable to provide information about localized strains and therefore limited in estimating wing mechanical feedback.

Alternatively, researchers have developed finite element analysis (FEA) based models [37]. FE models are capable of estimating localized strains on a deformed wing for each mode shape. However, such models are limited to infinitesimal rotation and cannot describe the entire time-dependent strain response of a flapping wing. The large rigid body motion and rotation of the wing generate a time-varying stiffness matrix $\mathbf{K}(t)$ which will have to be re-meshed during each time step of analysis, resulting in a large number of degrees of freedom. The significant number of degrees of freedom makes a direct FEA model computationally impractical. Physical insights, such as the contribution of gyroscopic forces, may also be lost.

Each of these models are capable of independently describing aspects of insect flight, such as aerodynamic force production and temporal strain. However, there remains a necessity to unify these models such that all their positive attributes can be fully realized. By synthesizing characteristics from each of these models, we develop a reduced-order model of a

flapping insect wing with the following important characteristics. First, the model is capable of predicting strain components under finite rotation. Second, the model retains a low order to maintain computational feasibility, thereby facilitating parametric studies. Lastly, the model discretizes the wing via FEA, so arbitrary geometry can be implemented readily. For this model formulation, effects of aerodynamics and aeroelasticity are neglected. It is assumed elastic deformation of the wing is solely a result of inertial-elastic effects [26].

2.2 Formulation

The model treats the wing as an elastic body subject to three-dimensional rotation about a point fixed on the insect's body. The displacement of any point on the wing is described by two finite rotations (pitch and roll), one small rotation (yaw), and one infinitesimal out-of-plane deflection. The rigid body displacement can readily be determined by establishing a rotating coordinate frame with prescribed kinematics. The out-of-plane deflection is a dynamic response and must be calculated by solving the equations of motion derived through energy methods. This section includes a summarized version of the derivation. For the complete derivation, please refer to Appendix A.

2.2.1 Kinematics

The wing is placed into a fixed reference frame, with the origin representing the fixed point of rotation and I, J, K being three orthogonal unit vectors associated with the fixed reference frame. (Fig 2.1). For this formulation, I, J, K are also referred to as coordinate axes. A rotating reference frame that pitches and rolls but does not yaw with the wing is established. The first rotation (roll) has an amplitude α and occurs about the I-axis, transforming the reference frame to the $I^{'} - J^{'} - K^{'}$ coordinate system. The second rotation (pitch) has an amplitude of β and occurs about the $J^{'}$-axis, transforming the reference frame to the $I^{''} - J^{''} - K^{''}$ coordinate system. Both of these rotations are assumed to have large and finite amplitudes. The third rotation corresponds to the yaw rotation, and is denoted by γ. The

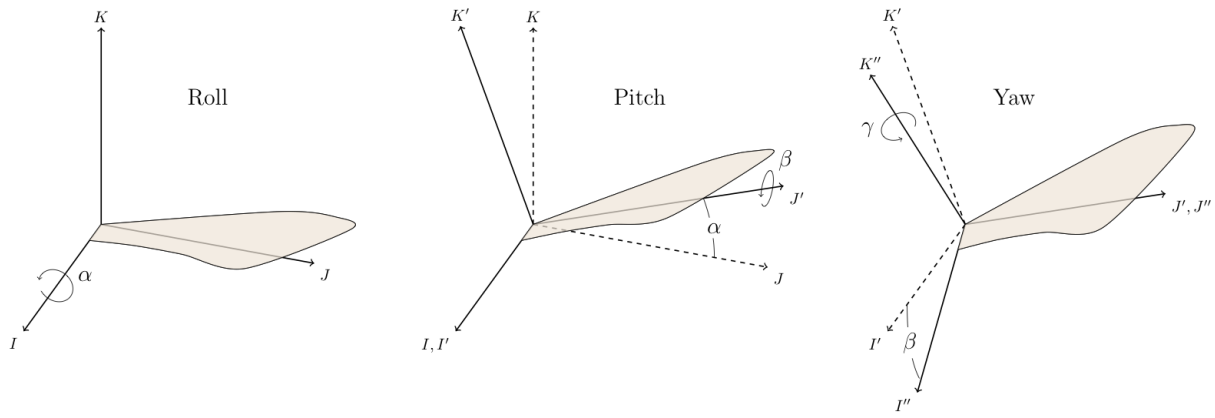

Figure 2.1: Development of rotating reference frame

yaw rotation (Figure 2.2) is assumed small, and consequently small angle approximations are employed. The yaw rotation occurs within the rotating reference frame. Through simple geometric analysis, the angular velocity $\vec{\Omega}$ of the rotating coordinate frame $I'' - J'' - K''$ is:

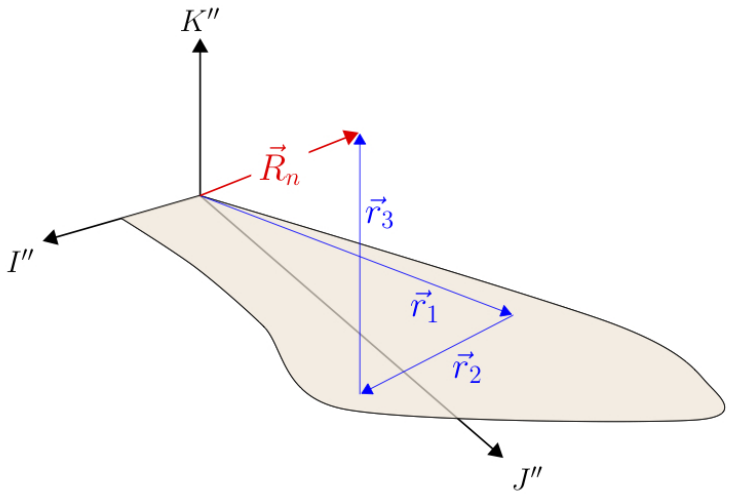

Figure 2.2: Position vectors and yaw rotation

$$\vec{\Omega} = \dot{\alpha} cos\beta I^{''} + \dot{\beta} J^{''} + \dot{\alpha} sin\beta K^{''} \tag{2.1}$$

With the rotating coordinate frame established, a position vector $\vec{R}_n$ (Fig 2.2) is drawn in the $I^{''} - J^{''} - K^{''}$ reference frame from the point of rotation to a differential mass dm on the wing geometry. $\vec{R}_n$ is the sum of three intermediate position vectors, $\vec{r}_1, \vec{r}_2$, and $\vec{r}_3$ ($\vec{R}_n = \vec{r}_1 + \vec{r}_2 + \vec{r}_3$), where $\vec{r}_1$ represents the position of the differential mass without yaw, $\vec{r}_2$ represents the contribution of the yaw rotation to the position, and $\vec{r}_3$ represents the out-of-plane elastic deformation of the wing. In-plane deformation neglected. Specifically, $\vec{r}_1, \vec{r}_2$, and $\vec{r}_3$ are described in both Cartesian and cylindrical coordinates as follows:

$$\vec{r}_1 = xI^{''} + yJ^{''} = r\vec{e}_r \tag{2.2}$$

$$\vec{r}_2 = \gamma(-yI^{''} + xJ^{''}) = \gamma r\vec{e}_\theta \tag{2.3}$$

$$\vec{r}_3 = W(\vec{r}_1, t)K^{''} = W(\vec{r}_1, t)\vec{e}_z \tag{2.4}$$

Above, x and y are the coordinates of the differential mass and $W(\vec{r}_1, t)$ is the elastic deformation dependent on both time and position. The position vector $\vec{R}_n$ is differentiated with respect to time to determine the velocity of the differential mass. As dm exists in a rotating coordinate frame, the chain rule must be applied to account for the time derivative of the coordinate frame. The resulting expression for the differential mass velocity $\dot{\vec{R}}_n$ is:

$$\dot{\vec{R}}_n = \vec{\Omega} \times \vec{R}_n + \dot{\vec{r}}_2 + \dot{\vec{r}}_3 \tag{2.5}$$

2.2.2 Kinetic and Potential Energies

The kinetic energy T of the wing is

$$T = \frac{1}{2}\int_m \dot{\vec{R}}_n \cdot \dot{\vec{R}}_n \, dm = \frac{1}{2}\int_m [\vec{\Omega} \times \vec{R}_n + \dot{\vec{r}}_2 + \dot{\vec{r}}_3] \cdot [\vec{\Omega} \times \vec{R}_n + \dot{\vec{r}}_2 + \dot{\vec{r}}_3] \, dm \tag{2.6}$$

where Equation 2.6 is integrated over the domain of the wing. The potential energy V is

$$V = \frac{1}{2}\int_v S(W,W)dv \tag{2.7}$$

where $S(W,W)$ represents a quadratic and symmetric strain energy density function, i.e., $S(a,b) = S(b,a)$, and the domain of integration is the volume of the wing. Use of the strain energy density function allows this formulation to be applied for any elastic body with complex geometry, assuming the structure deforms linearly.

2.2.3 Discretization

The unknown deformation of the wing $W(\vec{r}_1,t)$ can be expressed via an eigenfunction expansion

$$W(\vec{r}_1,t) = \sum_{k=1}^{\infty} \phi_k(\vec{r}_1)q_k(t) \tag{2.8}$$

where $\phi_k(\vec{r}_1)$ is the k^{th} mode shape and $q_k(t)$ is its modal response to be determined. Moreover, the mode shapes $\phi_k(\vec{r}_1)$ are normalized with respect to total mass satisfying the following orthonormal conditions,

$$\int_m \phi_k\phi_e \, dm = \delta_{ke} \tag{2.9}$$

where δ_{ke} is the Kronecker delta. Similarly, $\phi_k(\vec{r}_1)$ experiences orthogonality via the strain energy density function,

$$\int_v S(\phi_k,\phi_e) \, dv = \omega_k^2 \, \delta_{ke} \tag{2.10}$$

where ω_k is the natural frequency of the k^{th} mode shape. The advantage to the eigenfunction expansion is that the mode shape $\phi_k(\vec{r}_1)$ and the natural frequency ω_k may be determined using finite element modeling. Therefore, this formulation is valid for any arbitrary wing shape. Moreover, the boundary conditions of the wing are accounted for directly in the finite element analysis, and need not be evaluated explicitly for development of the equations of

motion.

Two geometric vectors useful to the derivation of the equations of motion are defined as follows

$$\vec{a}_k = \int r\phi_k(\vec{r}_1)\vec{e}_r dm = \int \phi_k(xI'' + yJ'')dm \tag{2.11}$$

$$\vec{b}_k = \int r\phi_k(\vec{r}_1)\vec{e}_\theta dm = \int \phi_k(-yI'' + xJ'')dm \tag{2.12}$$

where $\vec{a}_k$ represents a weighted geometric vector corresponding to the position of the inertial force center of the k^{th} mode shape relative to the point of rotation, and $\vec{b}_k$ (Equation 2.12) represents a 90° counter-clockwise rotation from $\vec{a}_k$.

2.2.4 Equation of Motion

To develop the equations of motion, kinetic and potential energy terms are discretized via Equation 2.8 and then subjected to Lagrange's equation. The modal response of the k^{th} mode, $q_k(t)$, is the generalized coordinate. Since the kinetic energy expansion is complicated, it is first expanded and subsequently leads to the following terms in Lagranges equation.

$$\frac{1}{2}\int_m [\vec{\Omega}\times\vec{R_n}]\cdot[\vec{\Omega}\times\vec{R_n}]dm = \frac{1}{2}\vec{\Omega}\cdot\vec{I_o}\cdot\vec{\Omega} \longrightarrow (\dot{\alpha}^2 cos^2\beta + \dot{\beta})q_k(t) - \vec{\Omega}\cdot(\vec{a_k} + \gamma\vec{b_k})(K''\cdot\vec{\Omega}) \tag{2.13a}$$

$$\frac{1}{2}\int_m (\dot{\vec{r_2}}\cdot\dot{\vec{r_2}})dm = \frac{1}{2}\int_m (\dot{\gamma}r\vec{e_\theta}\cdot\dot{\gamma}r\vec{e_\theta})dm = \frac{1}{2}\dot{\gamma}^2 I_{zz} \longrightarrow 0 \tag{2.13b}$$

$$\frac{1}{2}\int_m (\dot{\vec{r_3}}\cdot\dot{\vec{r_3}})dm = \frac{1}{2}\int_m [\dot{W}(\vec{r}_1,t)\vec{e_z}]\cdot[\dot{W}(\vec{r}_1,t)\vec{e_z}]dm = \frac{1}{2}\sum_{k=1}^{\infty}\dot{q_k}^2(t) \longrightarrow \ddot{q_k}(t) \tag{2.13c}$$

$$\int_m [\vec{\Omega}\times\vec{R_n}]\cdot\dot{\vec{r_2}}\,dm = \int_m [\vec{\Omega}\times\vec{R_n}]\cdot[\dot{\gamma}r\vec{e_\theta}]dm = \dot{\gamma}\int_m \vec{\Omega}\cdot[\vec{R_n}\times\vec{e_\theta}]r\,dm \longrightarrow -\dot{\gamma}\,\vec{\Omega}\cdot\vec{a_k} \tag{2.13d}$$

$$\int_m [\vec{\Omega}\times\vec{R_n}]\cdot\dot{\vec{r_3}}\,dm = \int_m [\vec{\Omega}\times\vec{R_n}]\cdot[\dot{W}(\vec{r}_1,t)\vec{e_z}]\,dm = \vec{\Omega}\cdot\sum_{k=1}^{\infty}\dot{q_k}(t)[\gamma\vec{a_k} - \vec{b_k}] \longrightarrow \frac{d}{dt}(\vec{\Omega}\cdot[\gamma\vec{a_k} - \vec{b_k}]) \tag{2.13e}$$

$$\int_m \dot{\vec{r_2}} \cdot \dot{\vec{r_3}}\, dm = \int_m [\dot{\gamma} r \vec{e_\theta}] \cdot [\dot{W}(\vec{r}_1, t)\vec{e_z}] dm \longrightarrow 0 \tag{2.13f}$$

$$\frac{1}{2}\int_v S[W(\vec{r}_1, t), W(\vec{r}_1, t)] dv \longrightarrow \omega_k^2\, q_k(t) \tag{2.13g}$$

In Equations 2.13a-2.13g, the terms to the left side of the "$\longrightarrow$" correspond to the expanded terms from the kinetic or potential energy, which lead to the right side of the "$\longrightarrow$" , corresponding to the terms derived from Lagranges equation. For an extensive derivation, please refer to Appendix A . The terms from Equations 2.13a-2.13g are combined and reorganized to develop the equation of motion (excluding damping) describing the modal response $q_k(t)$.

$$\ddot{q_k} + [w_k^2 - (\dot{\alpha}^2 cos^2\beta + \dot{\beta}^2)]q_k = -\dot{\vec{\Omega}} \cdot (\gamma \vec{a_k} - \vec{b_k}) - (K'' \cdot \vec{\Omega})[\vec{\Omega} \cdot (\vec{a_k} + \gamma \vec{b_k})] - 2\dot{\gamma}\vec{\Omega} \cdot \vec{a_k} \tag{2.14}$$

Equation 2.14 is a linear, time-varying second order ordinary differential equation. Time-variance is introduced in the stiffness coefficient, $[w_k^2 - (\dot{\alpha^2} cos^2\beta + \dot{\beta})]$, as a direct result of centrifugal softening. From a physical standpoint, the stiffness is at a minimum when the wing is at its extreme positions and at a maximum when then wing passes the $I - J$ plane.

Three forcing terms appear on the right hand side of Equation 2.14, indicating a self-excited system. These excitations result from wing rotation. Three forces typical in rotating coordinate frames are identified: Coriolis, Euler, and centrifugal forces. In general, the Coriolis force occurs when there is relative motion in a rotating coordinate frame. Specific to the wing, the relative motion is induced by the yaw rotation. The Euler force is due to the acceleration of the rotating coordinate frame. The centrifugal force is generated by the continuously changing inertia vector, and tends to draw the body away from the center of rotation. Each of these forces has a corresponding vector projection that is described in terms of $\vec{a_k}$ and $\vec{b_k}$. Table 2.1 shows a comparison between the typical form of each forcing term and their vector projection specific to the wing.

Table 2.1: Summary of Excitation Terms

Forcing Term	Typical Representation	Projected Representation
Euler Force	$-m(\dot{\vec{\Omega}} \times \vec{R})$	$-\dot{\vec{\Omega}} \cdot (\gamma \vec{a_k} - \vec{b_k})$
Centrifugal Force	$-m(\vec{\Omega} \times [\vec{\Omega} \times \vec{R}])$	$-(K'' \cdot \vec{\Omega})[\vec{\Omega} \cdot (\vec{a_k} + \gamma \vec{b_k})]$
Coriolis Force	$-2m(\vec{\Omega} \times \vec{V})$	$-2\dot{\gamma}\vec{\Omega} \cdot \vec{a_k}$

In Table 2.1, $\vec{R}$ is a position vector, m is a mass, and $\vec{V}$ is the relative velocity as seen from the rotating coordinate frame. These are presented purely for comparison purposes. Due to the linearity of Equation 2.14, solutions for $q_k(t)$ may be determined independently for each forcing term outlined in Table 2.1. This result is meaningful, as it allows direct comparison between the generalized coordinate response $q_k(t)$ for each type of force.

2.3 Example

The derived model is now applied an idealized forewing of the hawkmoth *Manduca sexta*. The *Manduca sexta* is an ideal subject for insect flight study due to the small variation between individual specimens [38] and the abundance of available research. To apply Equation 2.14, a finite element model is constructed to determine the mode shapes and natural frequencies of a *Manduca sexta* forewing. Next, assumed rotation profiles are presented for the insect in forward and hovering flight regimes. Forward flight is emphasized. Excitation terms and generalized coordinate responses for the first two mode shapes are analyzed. Finally, the effects of initial conditions, yaw rotation amplitudes, and damping on generalized coordinate responses are explored.

2.3.1 Finite Element Modeling

Finite element modeling is used to find mode shapes and natural frequencies of the wing. Published research has determined the natural frequencies and mode shapes of the *Manduca*

sexta forewing via finite element analysis, and the results agree closely with experimental results [39]. These finite element models serve as a benchmark for the finite element model developed for this research.

There exist numerous inherent complexities when designing such a finite element model. First, the real *Manduca sexta* forewing has complex geometry and venation patterns. Venation patterns are difficult to model, particularly when coupled with the cambered wing geometry. Second, the material properties of the wing membrane and vein structure are speculative. While several good estimates of these material properties are available, they must be used with some hesitation. Material properties are frequently measured using a wing extracted from the live insect, and are subject to variation over time as the wing begins to dry and stiffen. Moreover, membrane thickness tends to vary spatially along the wing. Given these difficulties, the proposed finite element model is designed assuming a paper wing of uniform thickness. The material properties of this wing are given in Table 2.2. The aim of the finite element model is to match closely the first two mode shapes and natural frequencies of the wing.

Table 2.2: Assumed material properties for the finite element paper wing

Symbol	Description	Value	Units
t	Thickness	81	μm
E	Young's Modulus	10	MPa
ρ	Density	0.86	g/cm^3
ν	Poisson's Ratio	0.3	-

The procedure outlined by Sims is used to construct the model wing geometry [40]. The finite element model is constructed using ABAQUS FEA software. First, a cambered surface corresponding to about 13% of the wing chord length is constructed using shell elements. A

planar section of the wing is then drawn to-scale using computed tomography (CT) images of the wing. The planar wing section is then projected onto the camber surface, and any additional material is removed. The result is a geometrically to-scale wing including camber effects. Wing camber has the notable effect of providing support to the first bending mode, thereby increasing the fundamental frequency. This result is significant, as the camber results in a structurally stiffer wing in the spanwise direction without significantly altering the mass distribution or total wing mass.

With the wing geometry constructed, material properties are defined in ABAQUS (Table 2.2). A section assignment is made to the wing geometry to assign thickness and material properties. A step is created (Linear Perturbation- Frequency) for modal analysis. One must select the "normalize with respect to mass matrix" option during this step to remain consistent with the derived equation of motion. Fixed boundary conditions (no translation or rotation, denoted by "Encastre" in ABAQUS) are applied where the wing meets the insect body. The model is then solved to determine the mode shapes and natural frequencies corresponding to the paper wing.

The natural frequencies determined by the finite element model are shown in Table 2.3, and the corresponding mode shapes are shown in Figure 2.3. The natural frequencies of the first two mode shapes agree within 4.5% of the reported values, indicating that the paper wing can adequately describe the modal properties of an actual *Manduca sexta* forewing. Furthermore, the mode shape classifications of the paper wing are consistent with those of an actual *Manduca sexta* forewing.

Table 2.3: Comparison of paper wing natural frequencies and reported *Manduca sexta* natural frequencies [39]

Natural Frequency	Determined Value	Reported Value	Mode Shape Classification
ω_1	62.5 Hz	60 Hz	Spanwise Bending
ω_2	86.9 Hz	84 Hz	Spanwise Torsion

$$\vec{a}_k = \sum_{i=1}^{j} \phi_{i,k}(x_i, y_i)[x_i I'' + y_i J'']dm_i \tag{2.15}$$

$$\vec{b}_k = \sum_{i=1}^{j} \phi_{i,k}(x_i, y_i)[-y_i I'' + x_i J'']dm_i \tag{2.16}$$

Vectors $\vec{a}_k$ and $\vec{b}_k$ are then determined numerically from the mode shapes pictured in Figure 2.3 using the above approximation. The i index denotes the i^{th} node of the finite element model and the j index represents the total number of nodes. Therefore, x_i and y_i represent the $x - y$ coordinates of the i^{th} node, $\phi_{i,k}(x_i, y_i)$ represents the out-of-plane displacement of the k^{th} mode shape at the i^{th} node, and dm_i represents the nodal mass of the i^{th} node. The nodal mass dm_i must be determined from the finite element model. As this quantity is not available in most commercial FEA packages, an alternative approach is taken. Beginning with the existing model, all preexisting boundary conditions are removed and any steps specific to the modal analysis deleted. Next, all degrees of freedom are fixed at each node using the Encastre boundary condition. A distributed unit load is the applied in the negative z directions, and the reaction forces at each node are calculated. These reaction forces correspond to the nodal mass (Fig. 2.4), and can in turned be used to numerically

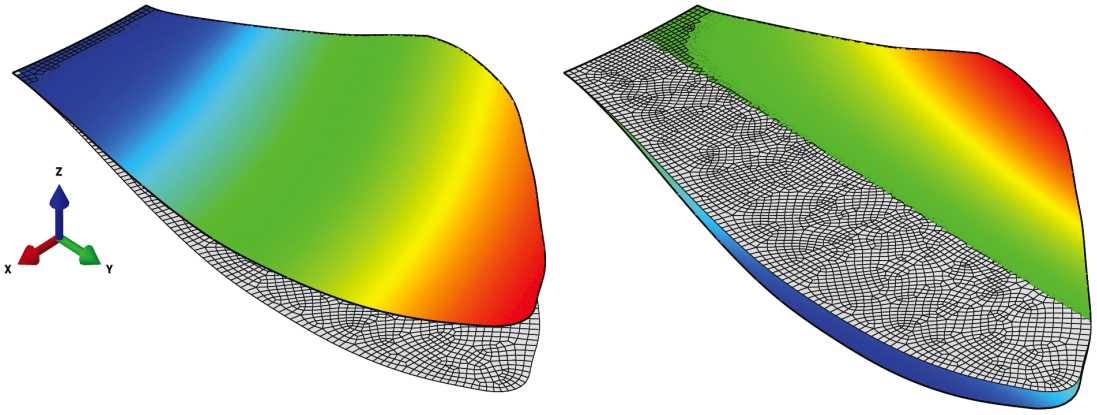

Figure 2.3: First two mode shapes of the paper wing- (Left) First Spanswise Bending, (Right) First Spanwise Torsion

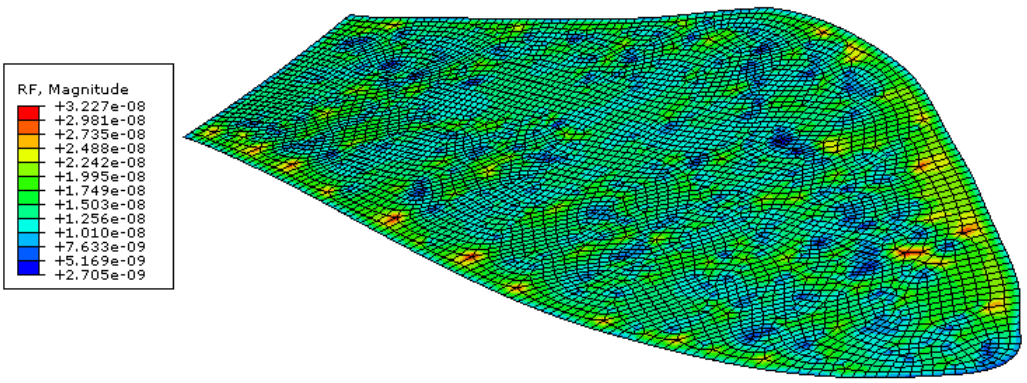

Figure 2.4: Reaction forces to unit load representing mass at each node of the wing

evaluate $\vec{a}_k$ and $\vec{b}_k$.

Table 2.4 shows the geometric vectors $\vec{a}_k$ and $\vec{b}_k$ for the first two modes. In general, $\vec{a}_k$ and $\vec{b}_k$ are very small. Therefore, a second set of vectors $\vec{a}'_k$ and $\vec{b}'_k$ is defined in Table 2.4, where $\vec{a}'_k$ and $\vec{b}'_k$ are normalized with respect to the largest component of vectors $\vec{a}_k$ and $\vec{b}_k$. For predictions of physical quantities (i.e., strain distribution), $\vec{a}_k$ and $\vec{b}_k$ will be used. For comparison of modal responses, $\vec{a}'_k$ and $\vec{b}'_k$ will be used due to the convenience of their magnitudes.

Table 2.4: Geometric Vectors for first two mode shapes- Paper Wing FEA model

Vector	I''	J''	Normalized Vector	I''	J''
$\vec{a}_1$	0.7552×10^{-5}	0.0934×10^{-5}	$\vec{a}'_1$	1.0	0.123
$\vec{b}_1$	-0.0934×10^{-5}	0.7552×10^{-5}	$\vec{b}'_1$	-0.123	1.0
$\vec{a}_2$	-0.1728×10^{-5}	-0.0033×10^{-5}	$\vec{a}'_2$	-0.2289	-0.0044
$\vec{b}_2$	0.0033×10^{-5}	-0.1728×10^{-5}	$\vec{b}'_2$	0.0044	-0.2289

2.3.2 Rotation Profiles

Equation 2.14 allows for any function to describe pitch, roll, and yaw rotations independently. In this example, each rotation is assumed sinusoidal and periodic with a frequency of $\omega_d = 25$ Hz representing the flap frequency of the *Manduca sexta*. Mathematically, the roll rotation takes the form $\alpha = \alpha_0 \sin(\omega_d t)$, where α_0 denotes the rotation amplitude in radians. The pitch and yaw rotations take the same form, with their amplitudes described by β_0 and γ_0 respectively. Phase angles are not considered in this example.

The flight of the *Manduca sexta* is divided into two principal regimes— forward flight and hovering flight. In each of these regimes, rotation amplitudes α_0, β_0 and γ_0 exhibit vastly different characteristics. Typical rotation amplitudes for a *Manduca sexta* hovering and traveling forward at a speed of 5 m/s are shown in Table 2.5 [38]. Please note that the sinusoidal rotation is an idealized trajectory.

Table 2.5: Rotation Amplitudes for Hovering and Forward Flight (5 m/s)

Rotation Amplitude Parameter	Forward Flight (rad)	Hovering Flight (rad)
α_0	0.8	1.0
β_0	0.5	0.1
γ_0	0.2	0.03

In this example, the forward flight regime is considered, and all rotation amplitudes correspond to the forward flight regime described in Table 2.5.

2.3.3 Time/Frequency Domain of System Parameters

Prior to solving the equation of motion, each of the system parameters is investigated in time and frequency domains. The system parameters correspond to the time-varying stiffness and excitation terms of Equation 2.14. Figure 2.5 shows each of the system parameters as a function of time for the first mode shape. From Figure 2.5, it can be seen that the Euler

Force has the largest magnitude, the Coriolis Force has the second largest magnitude, and the centrifugal force has the smallest magnitude. Both the stiffness and Coriolis force vary nearly sinusoidally in sync with a frequency of approximately twice the flap frequency. The Euler and centrifugal forces appear to have more complicated forms. To determine the frequency content of each of these system parameters, a power spectral density (PSD) algorithm is employed. The offset occurring at $\omega = 0$ for the stiffness, Coriolis, and Euler terms is neglected. The results of the PSD analysis are shown in Figure 2.6 for the first mode shape.

PSD effectively decomposes each of the system parameters into its frequency components. The Coriolis Force and stiffness indeed oscillate at a frequency close to $2\omega_d$. The Centrifugal force oscillates predominately at $3\omega_d$, with lesser components at ω_d. The Euler force oscillates at ω_d, with depreciating components at $2\omega_d$, $3\omega_d$, etc. Interestingly, the oscillation frequencies of the Coriolis force occurs near the first natural frequency ω_1, and oscillation frequencies of

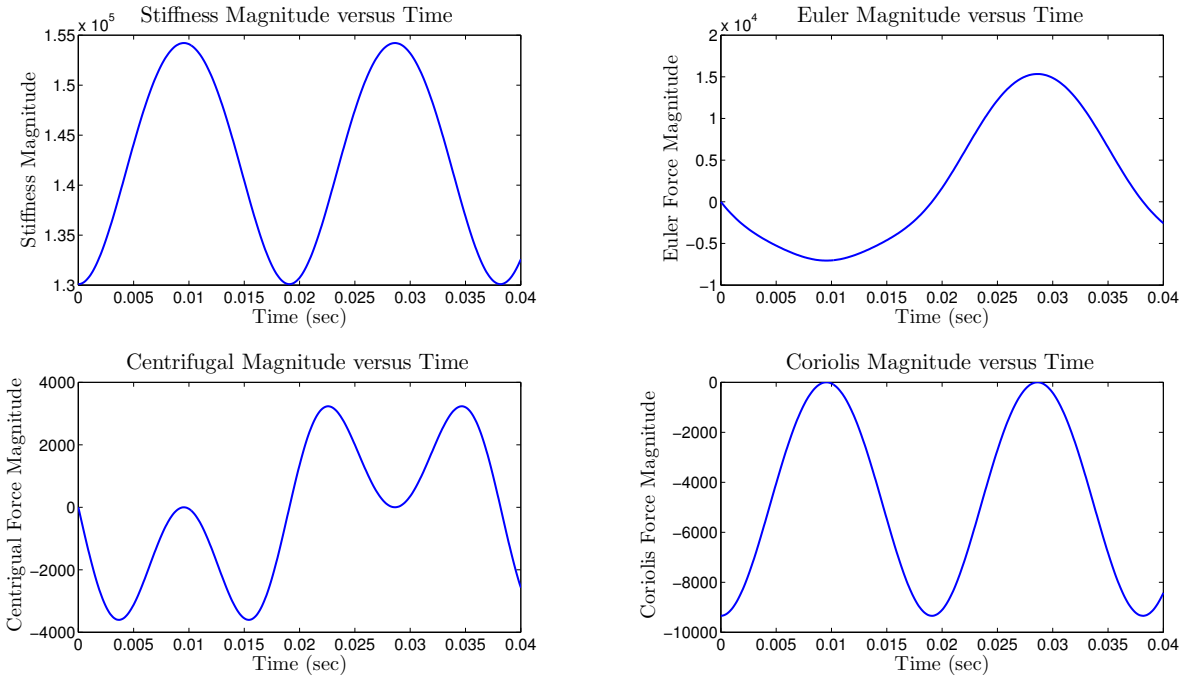

Figure 2.5: Systems parameters in the time domain, first vibration mode

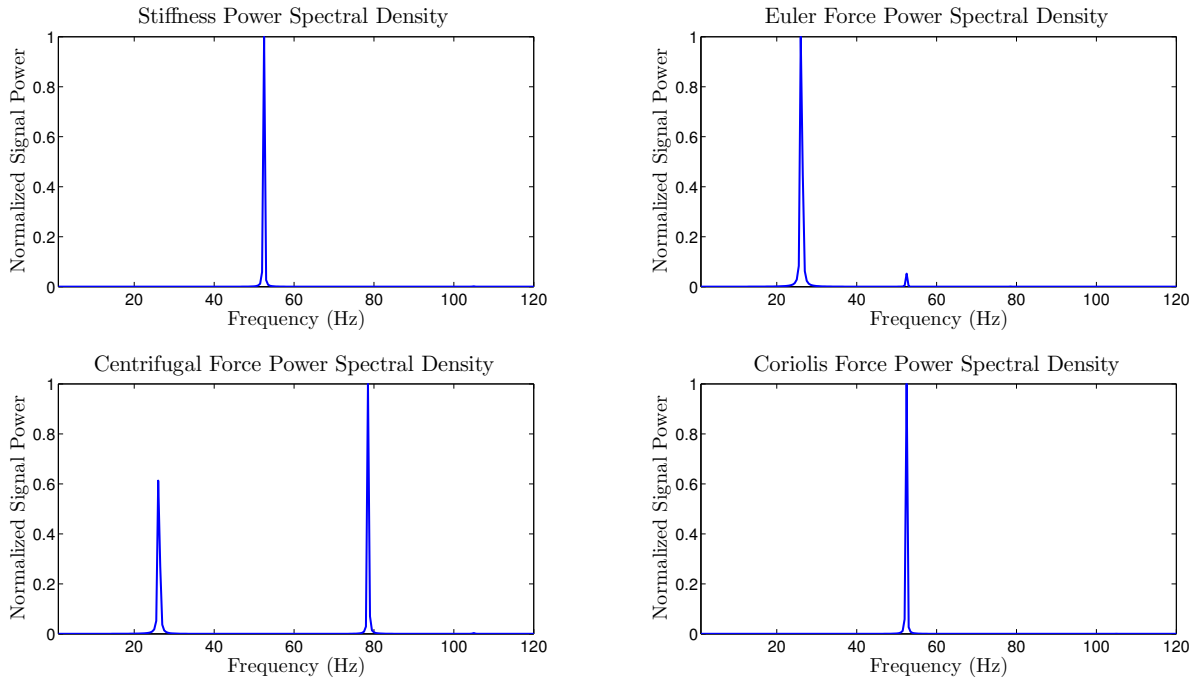

Figure 2.6: Systems parameters in the frequency domain, first vibration mode

the centrifugal force occur near the second natural frequency ω_2. The proximity to natural frequencies may have a marked effect on the generalized coordinate responses.

2.3.4 Generalized Coordinate Responses

Equation 2.14 is solved assuming zero initial conditions ($q_k(0) = 0, \dot{q}_k(0) = 0$). The response subject to each excitation term is solved individually, and due to linearity, the results are summed to determine the overall system response. In this section, all responses are solved numerically using Matlab. The results for the first mode are shown in Figure 2.7.

The generalized coordinate responses for the first mode provides interesting results. First, despite having the largest magnitude, the Euler force generates only the second largest response. The Euler force generates oscillations predominately at a frequency ω_d, roughly half the natural frequency of the first mode ω_1. On the other hand, the Coriolis force oscillates

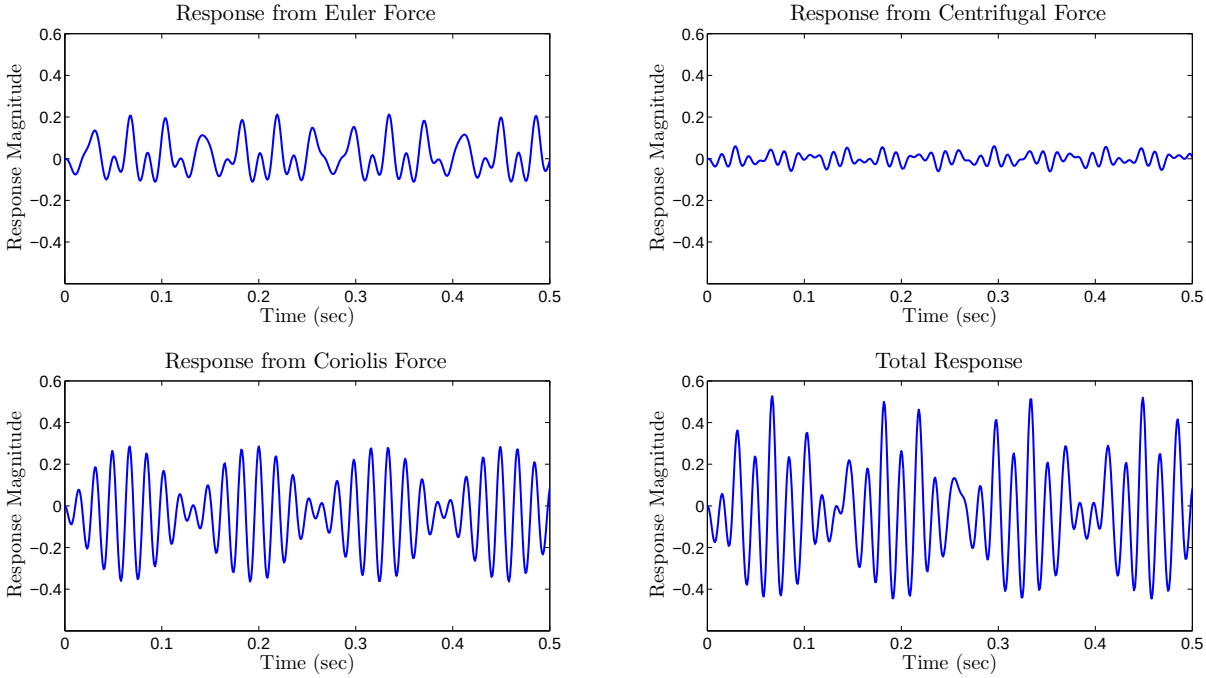

Figure 2.7: Generalized coordinate responses to excitation, first vibration mode

at $2\omega_d$, which is close to ω_1. As a result, the Coriolis force generates a larger response due to operating near resonance despite having a lesser magnitude than the Euler force.

Second, a clear beat phenomenon exists in the Coriolis response. The beat phenomenon occurs between the $2\omega_d$ oscillation frequency of the Coriolis force and effective natural frequency ω_1 of the first mode shape. Lastly, the centrifugal force appears to have a very minor contribution to the response of the first mode shape. This is due to the relatively low magnitude of the centrifugal force coupled with the fact that dominant oscillations occur away from the first natural frequency.

Next, the response of the second mode shape is solved. The results are shown in Figure 2.8. Similar to the Coriolis force for the first mode shape, the centrifugal force oscillates near the second natural frequency ω_2. The result is a significant contribution to the generalized coordinate response, as well as the presence of a beat phenomenon occurring between

$3\omega_d$ and the effective natural frequency of the second mode shape. Both the Euler force and Coriolis force oscillate away from resonance, and therefore have comparatively low contributions to the response.

2.3.5 Time-Invariant Approximation

The time-varying stiffness coefficient is contingent on time-varying parameter $[\omega_k^2 - (\dot{\alpha}^2 cos^2\beta + \dot{\beta}^2)]$. Therefore, if α_0 and β_0 become large, the time-varying stiffness will have a substantial impact. However, in the context of insect flight, α_0 and β_0 typically fall within the domain of $[0, \frac{\pi}{2}]$. Consequently, the time-variance caused by the centrifugal softening tends to have a small effect on the stiffness magnitude. Therefore, a stiffness averaged over one period of the wing beat is defined as ω_{avg} and may replace the time-varying stiffness coefficient in Equation 2.14. Mathematically, the average stiffness can be calculated by

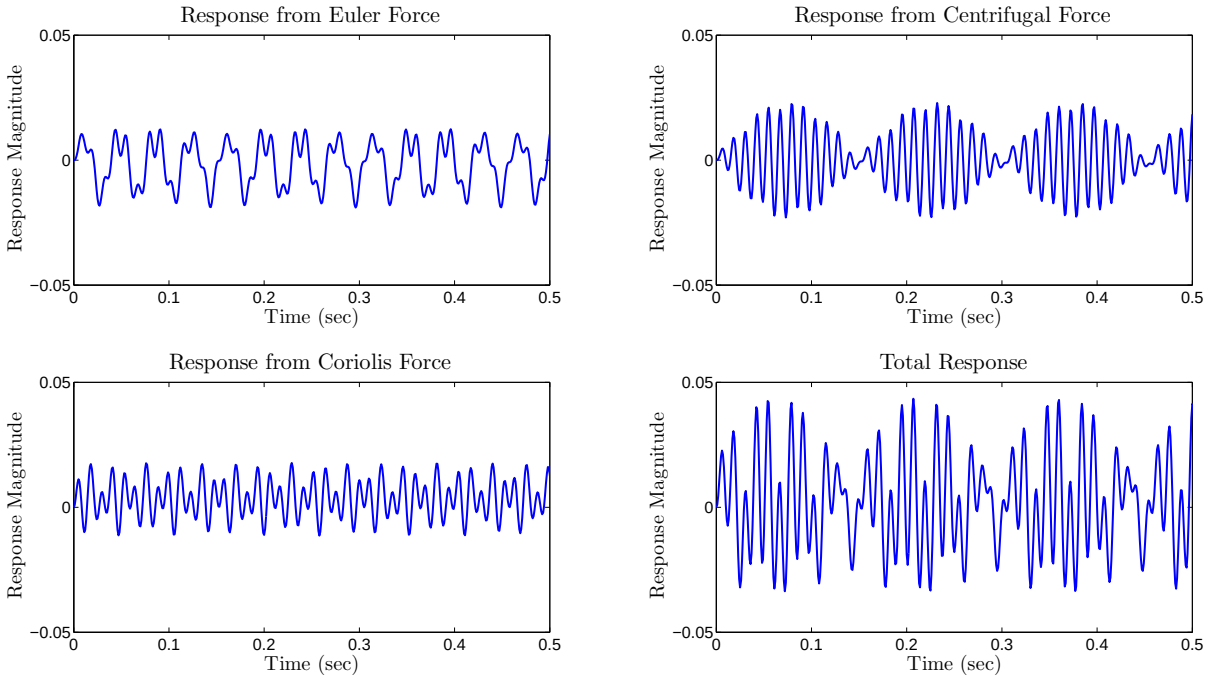

Figure 2.8: Generalized coordinate responses to excitation, second vibration mode

$$\omega_{avg}^2 = \int_0^{\frac{2\pi}{\omega_d}} [\omega_k^2 - (\alpha_0^2 \cos^2(\omega_d t)\cos^2(\beta) + \beta_0^2 \cos(\omega_d t))]dt \tag{2.17}$$

$$\omega_{avg}^2 = w_k^2 - 0.5(\alpha_0^2 + \beta_0^2)\omega_d^2 \tag{2.18}$$

The value of ω_{avg} is then substituted into Equation 2.14 resulting in the following modified linear time-invariant equation.

$$\ddot{q_k} + \omega_{ave}^2 q_k = -\dot{\vec{\Omega}} \cdot (\gamma \vec{a_k} - \vec{b_k}) - (K'' \cdot \vec{\Omega})[\vec{\Omega} \cdot (\vec{a_k} + \gamma \vec{b_k})] - 2\dot{\gamma}\vec{\Omega} \cdot \vec{a_k} \tag{2.19}$$

The impact of removing the time-variance of the system is that approximate analytic solutions can now be determined. Approximate analytic solutions have two distinct advantages compared to exact numeric solutions. First, numeric solutions must be calculated through

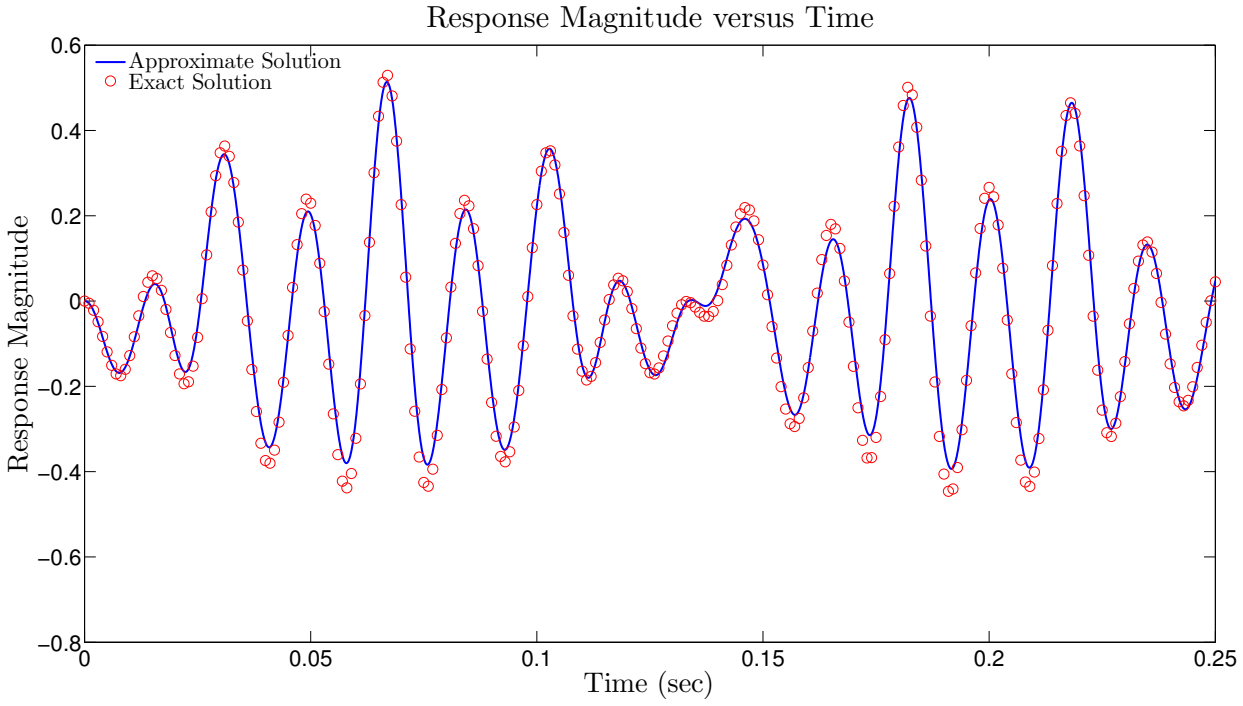

Figure 2.9: Analytic and Numeric Solutions of the Total Response

software, which involves solving several differential equations. Should numeric solutions be used to conduct parametric studies, the computational load will be substantial. On the other hand, approximate analytic solutions allow parametric studies to be performed with ease. Second, approximate analytic solutions serve as a basis of comparison to numerical simulations. This closed-form solution helps identify physical insights observed in the numeric solution, such as the beat phenomenon.

Each of the excitation terms in Equation 2.19 contains some factor of $cos(\beta)$ or $sin(\beta)$. As β itself is a sinusoidal function, this presents some complications in determining analytic solutions. It is desirable to represent $cos(\beta)$ or $sin(\beta)$ in terms of an infinite-series expanded using Bessel functions J_n. As contributions for Bessel functions J_2 and higher are determined to have negligible contributions, the approximation of $cos(\beta)$ and $sin(\beta)$ can be written as Equations 2.20-2.21.

$$cos\beta \approx J_0(\beta_0) + \sum_{n=2,even}^{\infty} 2J_n(\beta_0)cos(n\omega_d t) \approx J_0(\beta_0) \tag{2.20}$$

$$sin\beta \approx \sum_{n=1,odd}^{\infty} 2J_n(\beta_0)sin(n\omega_d t) \approx 2J_1(\beta_0)sin\omega_d t \tag{2.21}$$

Operating under the above assumptions, approximate analytic solutions for the linear time invariant system can be calculated. These approximate solutions are compared to the exact numerical solutions. For the example outlined in this section, Figure 2.9 shows a comparison of analytic and numeric total responses of the first mode.

Figure 2.9 indicates that the analytic and numeric solutions agree reasonably well, with the numeric response having a slightly larger magnitude at the response peaks. The reason for the slight discrepancy is the approximation of $cos(\beta)$ and $sin(\beta)$, as well as the approximation of the averaged stiffness ω_{avg}. However, the error is small enough such that the approximate analytic solutions may be used with confidence moving forth.

2.4 Beat Phenomenon

Numeric simulations indicate the beat phenomenon occurs in the first and second modes as a response to Coriolis and centrifugal forcing, respectively (Fig 2.7-2.8). This response suggests interactions between similar frequencies resulting in constructive and destructive interference, thereby causing a beating effect. The time-invariant approximation of the wing differential equation (Eq. 2.19) may help identify the physical cause of the beat phenomenon.

While the total time-invariant solution is relatively complicated, aspects of the solution identify the cause of the beat phenomenon. As an example, consider the response of the first mode (i.e., Equation 2.19 with $k = 1$) subject to partial Coriolis excitation $-2\dot{\gamma}\Omega_j a_j$, where Ω_j is the j-component of $\vec{\Omega}$ and a_j is the j-component of $\vec{a}_1$. Let $q_c(t)$ be the corresponding response subject to initial conditions $q_c(0) = 0$ and $\dot{q}_c(0) = 0$. Equation 2.19 is then reduced to

$$\ddot{q}_c + \omega_{avg}^2 q_c = -2\dot{\gamma}\Omega_j a_j \tag{2.22}$$

With $\beta = \beta_0 \cos\omega_d t$ and $\gamma = \gamma_0 \cos\omega_d t$, Equation 2.22 results in

$$\ddot{q}_c + \omega_{avg}^2 q_c = -2C_1 \cos^2(\omega_d t) = -C_1[1 + \cos(\omega_d t)]; \qquad C_1 = a_j \gamma_0 \beta_0 \omega_d^2 \tag{2.23}$$

$$q_c(t) = C_1 \left[\frac{\cos(\omega_{avg} t) - \cos(2\omega_d t)}{\omega_{avg}^2 - 4\omega_d^2}\right] + C_1 \left[\frac{\cos(\omega_{avg} t) - 1}{\omega_{avg}^2}\right] \tag{2.24}$$

Applying a trigonometric identity to the first term in Equation 2.24,

$$\frac{C_1}{\omega_{avg}^2 - 4\omega_d^2}[\cos(\omega_{avg} t) - \cos(2\omega_d t)] = \frac{-2C_1}{\omega_{avg}^2 - 4\omega_d^2} \left[\sin\left(\frac{\omega_{avg} + 2\omega_d}{2} t\right) \sin\left(\frac{\omega_{avg} - 2\omega_d}{2} t\right)\right] \tag{2.25}$$

Consequently, the form of $q_c(t)$ suggests the Coriolis force oscillating with a frequency of $2\omega_d$ will interact with the free vibration of frequency ω_{avg}, thereby generating a beat phenomenon in the first mode shape. If $2\omega_d$ and ω_{avg} have similar values, the beating effect will

become more pronounced. By the same procedure, the time-invariant solution can be used to show the beat phenomenon in the second mode as a result of centrifugal forcing. In doing so, the frequency content of the excitation terms shown in Figure 2.6 is implicitly verified.

The beat phenomenon as revealed in Equation 2.25 can also be used as a way to detect gyroscopic forces. The beat amplitude is proportional to constant C_1, which, in terms, is proportional to the yaw amplitude γ_0. The beat phenomenon, both in frequency and magnitude, may potentially allow insects to detect such gyroscopic forces.

Frye hypothesizes that the frequency content generated by the stretch receptor in the *Manduca sexta* forewing plays a vital role in the neural feedback used by the insect to interpret flight status [41]. It seems plausible then that the beat phenomenon has biological significance in providing neural feedback during insect flight. As the total generalized coordinate response exhibits a beat response, the strain components in the wing will also reflect a beat response. Should the insect be capable of interpreting beat effects in the first two modes, the rotations α,β and γ may be identified. As these rotations have a direct correlation to aerodynamic parameters (e.g. lift, drag), the beat amplitudes may be used to identify flight status. Consequently, it is possible that MAV design could implement strain-based control systems rather than accelerometer-based control systems. This may potentially reduce both the weight and the power consumption of the MAV.

Motivated by the potential applications of the beat phenomenon, we determine the sensitivity of the beat response in the first mode subject to Coriolis forcing. Both the hovering and flight regimes described by Table 2.5 are considered.

2.4.1 Sensitivity to Yaw Amplitude

The amplitude of the yaw rotation, γ_0, has been found to have a tremendous influence on the magnitude of the Coriolis force. While the typical yaw amplitudes for hovering and forward flight (Table 2.5) are relatively consistent, it is possible individual specimens deviate slightly

from these values. Therefore, the contribution of each forcing term to the wing response is determined as a function of γ_0. To remain consistent with the small angle approximation, a range of yaw amplitude $0 \leq \gamma_0 \leq 0.3$ is considered. The linear time-invariant equation of motion (Eq. 2.19) is solved independently for the Coriolis, Euler and centrifugal forces over the entire range of γ_0 assuming zero initial conditions. The square sum of each partial response is divided by the square sum of the total response to determine the contribution of each forcing term as a percentage. The results of the simulation are shown in Figure 2.10.

At the operation points of γ_0 described in Table 2.5, the contribution of the Coriolis force to the total response is substantially larger than the contribution from the other two forces. In the forward flight regime, even large variations of γ_0 will cause only a minor change in the Coriolis contribution. In the hovering flight regime, increases in γ_0 result in only a minor change in Coriolis contribution, while decreases in γ_0 cause the Coriolis contribution to decay rapidly. Thus, in both cases, an increase of γ_0 results in the amplification of the beat phenomenon. This study also shows the beat phenomenon can serve as an effective way

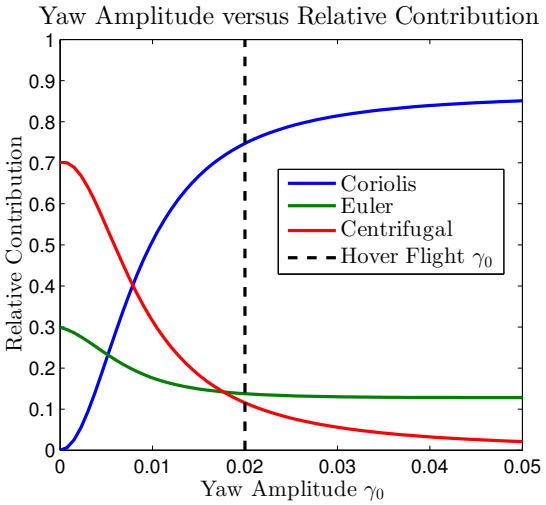

Figure 2.10a: Hovering Flight

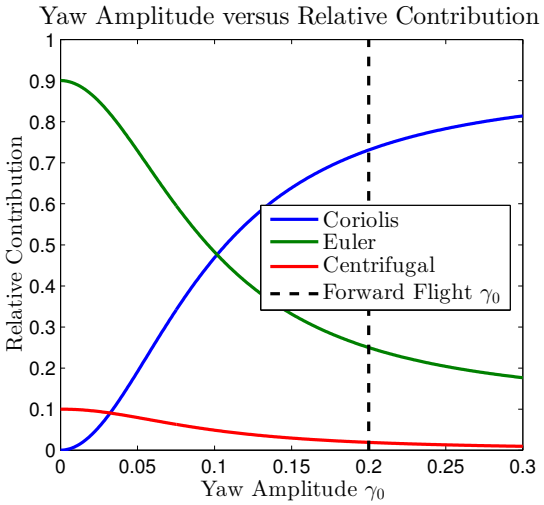

Figure 2.10b: Forward Flight

Figure 2.10: Relative contribution of forcing terms to response as a function of γ_0

to obtain $\dot{\gamma}$ from the wing response.

2.4.2 Sensitivity to Initial Conditions

According to Equation 2.25, the beat phenomenon results from an interaction between the forced vibration of the Coriolis force with frequency $2\omega_d$ and the free vibration of the wing with frequency ω_{avg}. From a mathematical standpoint, there exists a set of initial conditions that will cause the free vibration of the wing to disappear from the response. If there is no free vibration of the wing to interact with the forced vibration, the beat phenomenon will no longer be present.

Consequently, it is prudent to look at the Coriolis contribution as a function of non-zero initial conditions. To identify an allowable set of initial conditions, Equation 2.14 is solved assuming zero initial conditions. For both the forward and hovering flight regimes, the maximum and minimum values of $q(t)$ and $\dot{q}(t)$ constitute the upper and lower bounds of allowable initial conditions. Mathematically, this takes the form $q(t)_{min} \leq q(0) \leq q(t)_{max}$ and $\dot{q}(t)_{min} \leq \dot{q}(0) \leq \dot{q}(t)_{max}$. The Coriolis contribution is then determined by solving Equation 2.14 over the entire set of initial conditions using the time-dependent formulation. The results are shown in Figure 2.11.

Figure 2.11 shows the Coriolis contribution has similar sensitivity to various initial conditions in the forward and hovering flight regimes. For either regime, the contribution of the Coriolis force is more than 60% for most initial conditions. Even for extreme initial conditions, the contribution of the Coriolis force still constitutes about 33% of the total contribution. In this scenario, all three forces generate approximately equal contributions. Thus, some non-zero initial conditions may cause the beat phenomenon to become less distinct, but it will never entirely be removed from the total response.

2.4.3 Damping

As the beat phenomenon relies partially on the free vibration of the wing, structural damping may have the effect of diminishing the beat over time. To determine the significance of these effects, structural damping of 1% ($\zeta = 0.01$) is introduced into Equation 2.14. The response subject to Coriolis forcing is then determined numerically for the first mode shape (Figure 2.12). As the free vibration of the wing dissipates as a result of damping, the beat phenomenon gradually becomes less pronounced. After several seconds, the Coriolis force causes only the forced vibration of the wing, which oscillates sinusoidally at $2\omega_d$.

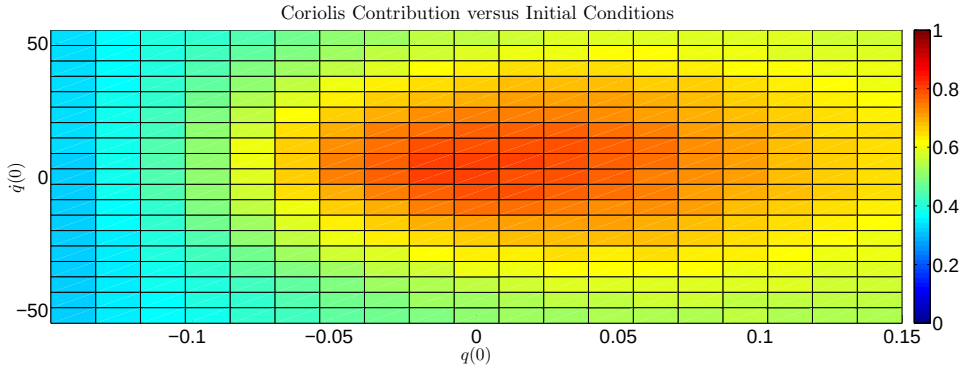

Figure 2.11a: Hovering Flight

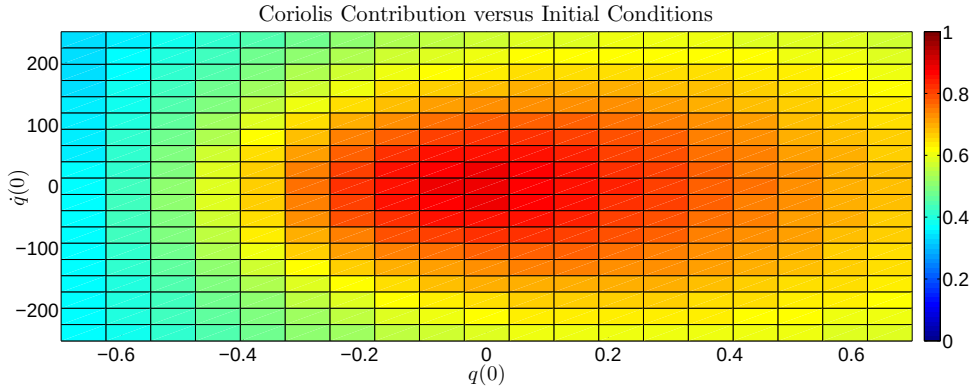

Figure 2.11b: Forward Flight

Figure 2.11: Relative contribution of Coriolis response to various initial conditions

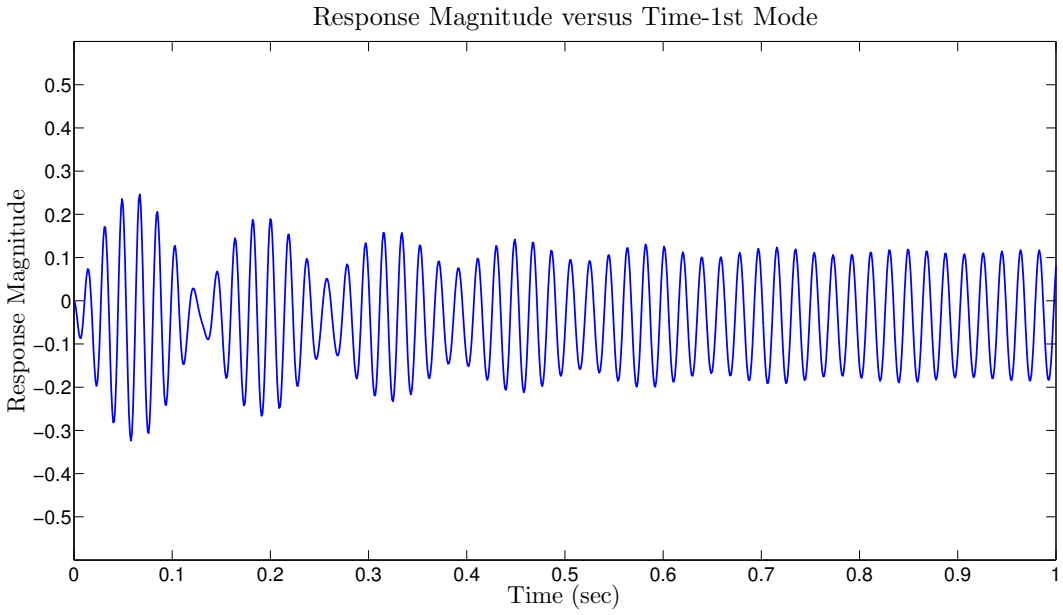

Figure 2.12: Damped generalized coordinate response to Coriolis forcing, first vibration mode

For insects, there exist a number of ways in which the beat phenomenon may be preserved in the response despite structural damping. First, rotation amplitudes may be randomized slightly from their mean values to better represent flapping of a real insect. Subtle variations, particularly in the yaw amplitude, allow the beat phenomenon to be maintained. Second, unmodeled body translations may reinvigorate wing free vibration, thereby reestablishing the beat phenomenon. This suggests that it is desirable for an insect to move frequently to preserve feedback generated by deformation of the forewing.

2.4.4 Strains

Consider a point of interest on the wing $P(x, y)$. Let ϵ_x be the normal strain in the x-direction, ϵ_y be the normal strain in the y-direction, and τ_{xy} be the shear strain in the xy plane at $P(x, y)$. The strain components can be represented by

$$\epsilon_x(x,y,t) = \sum_{k=1}^{\infty} \epsilon_{x,k}(x,y) q_k(t) \tag{2.26}$$

$$\epsilon_y(x,y,t) = \sum_{k=1}^{\infty} \epsilon_{y,k}(x,y) q_k(t) \tag{2.27}$$

$$\tau_{xy}(x,y,t) = \sum_{k=1}^{\infty} \tau_{xy,k}(x,y) q_k(t) \tag{2.28}$$

where $\epsilon_{x,k}$ is the normal strain in the x-direction of the k^{th} mode, $\epsilon_{y,k}$ is the strain in the y-direction of the k^{th} mode, and $\tau_{xy,k}$ is the shear strain in the xy plane of the k^{th} mode. Figures 2.13-2.14 show the strain components for the first and second modes, respectively. The first mode is a spanwise bending mode, resulting in significant strain at the center of the wing base. The second mode is a spanwise torsion mode, and results in large strains at the leading and trailing edge of the wing base. A point $P(x,y)$ is selected near the base of the wing (Fig. 2.13, top). The strain components are determined by finite element analysis for the first two mode shapes as shown in Table 2.6.

Table 2.6: Modal strains at $P(x,y)$, first two vibration modes

Strain component	First Mode ϕ_1	Second Mode ϕ_2
ϵ_x	-256	161
ϵ_y	1577	-96.7
τ_{xy}	-691	-1710

$q_1(t)$ and $q_2(t)$ are calculated by numerically solving Equation 2.14 assuming zero initial conditions and using the $\vec{a}_k$ and $\vec{b}_k$ vectors. The total time-dependent strain is determined using the strain values from Table 2.6 and applying Equations 3.1-2.28. The results are shown in Figure 2.15. The shear strain τ_{xy} has the largest magnitude, while the x-component of strain ϵ_x and the y-component of strain ϵ_y have comparatively negligible magnitudes. For all strain components, the beat phenomenon is loosely observed.

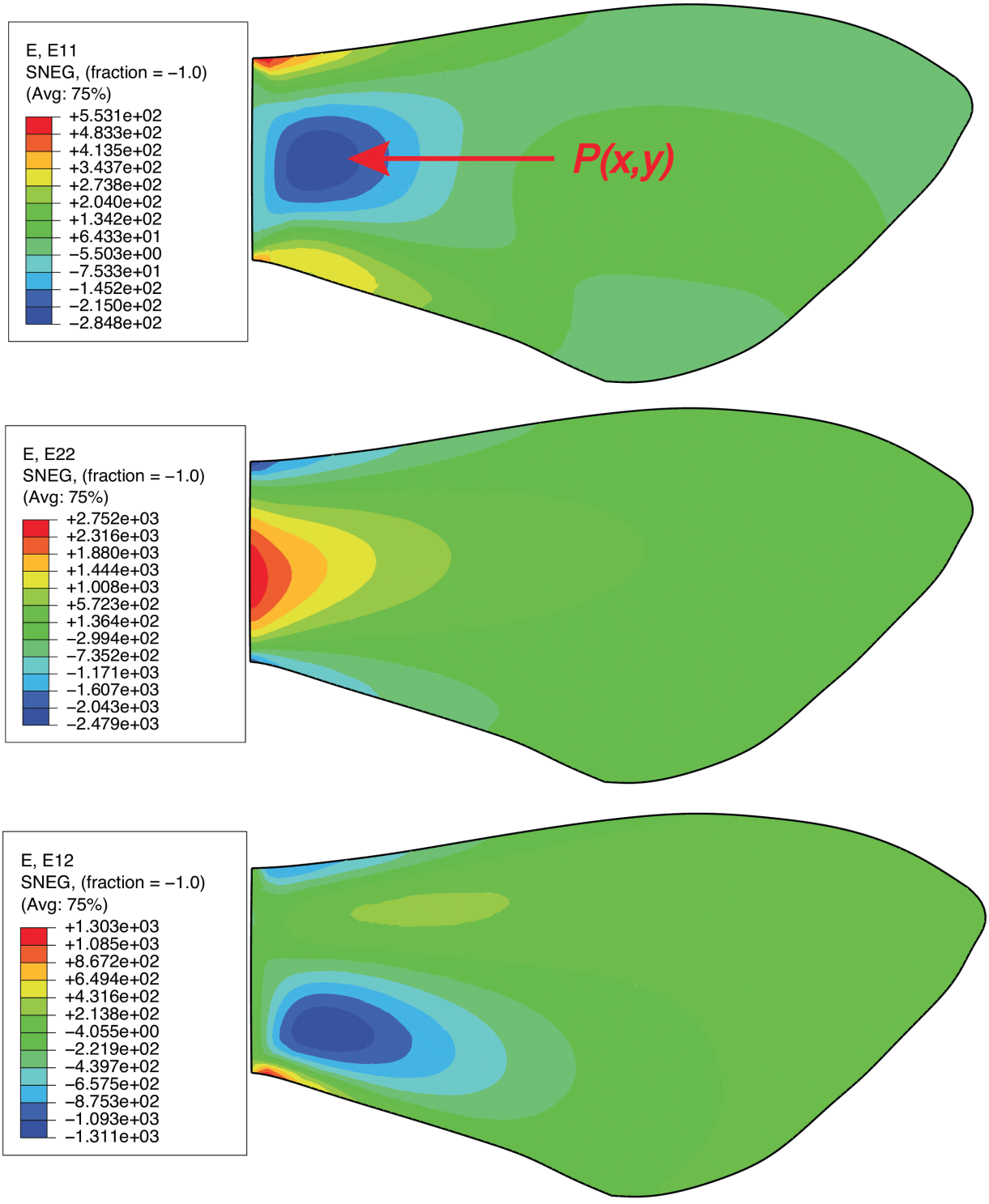

Figure 2.13: Strain components, First Mode Shape- (Top) ϵ_x, (Center) ϵ_y, (Bottom) τ_{xy}

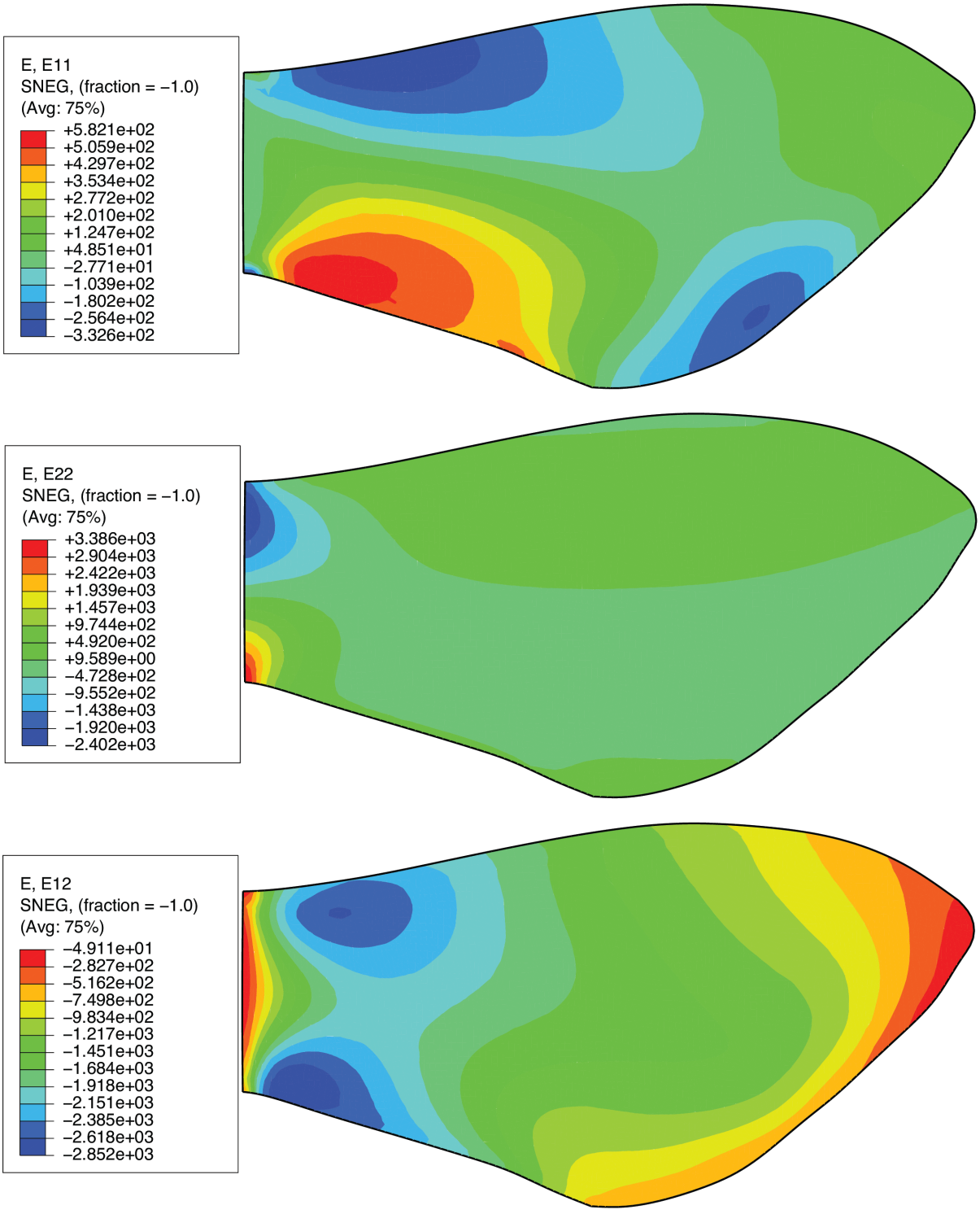

Figure 2.14: Strain components, Second Mode Shape- (Top) ϵ_x, (Center) ϵ_y, (Bottom) τ_{xy}

2.5 Discussion

A comprehensive dynamic model of an insect wing is developed treating the wing as a deformable body subject to three dimensional rotation about a fixed point on the insect's body. A coordinate frame that rotates with the finite pitch and roll rotations is established. A third yaw rotation is assumed small and rotates independently of the coordinate frame. Kinetic and potential energies are formulated, and the set of uncoupled differential equations describing the time response of each mode shape (determined by finite element analysis) is determined by Lagrange's equation. There are several advantages to such a formulation. First, the model is able to estimate the time-dependent strain components on the wing. Second, the model allows any complex geometry to be implemented readily. Third, the resulting model has reduced order— the order of the model is the number of mode shapes retained.

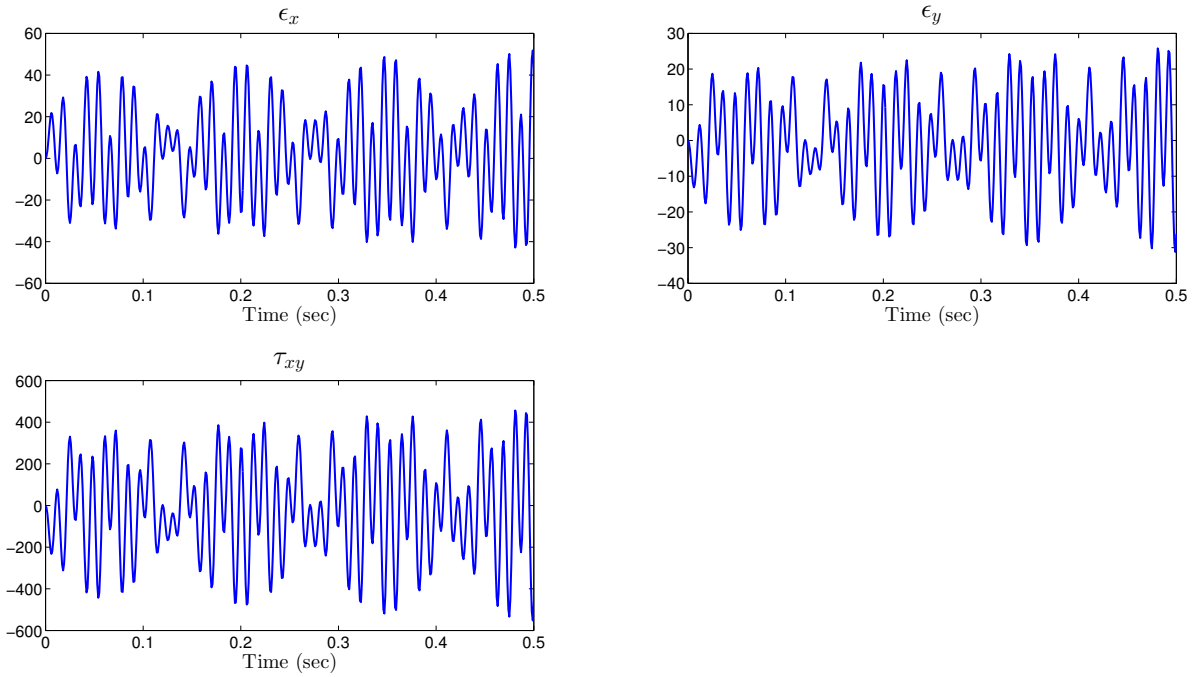

Figure 2.15: Time dependence of strain components at $P(x, y)$

The model is then applied to the forewing of the *Manduca sexta*. Coriolis, Euler, and centrifugal forces excitations cause the elastic deformation of the wing. The Coriolis force tends to dominate the first mode whereas the centrifugal force tends to dominate the second mode. Numerical integration indicates a beat phenomenon occurs in both the first and second modal responses. A time-invariant approximation shows the beat phenomenon is a result of the interaction of free vibration and Coriolis forcing in the first mode, and the interaction of free vibration and centrifugal forcing in the second mode. The sensitivity of the beat phenomenon in the fundamental mode is explored. The beat phenomenon is relatively insensitive to various yaw amplitudes and non-zero initial conditions, but decays gradually in the presence of damping. Resetting of initial conditions or slight variations of the yaw amplitude cause the beat phenomenon to persist even in the presence of damping.

The total temporal normal and shear strain components are calculated at a point of interest near the base of the wing. The shear strain component is determined to be significantly larger than the normal strain components. In all cases, the strain components exhibit a beat phenomenon. This result suggests the *Manduca sexta* may use strain frequency data associated with the beat phenomenon to help identify flight status. In the context of MAVs, similar strain-based control systems may be developed to replace or supplement traditional acceleromater-based control systems. This can potentially increase MAV performance by reducing weight, size, and power consumption.

Chapter 3

EXPERIMENTAL VALIDATION OF WING MODEL

Several researchers have attempted to experimentally characterize the complex mechanics the insect forewing, typically treating the wing as a rotating structure. The majority of such experiments are intended to evaluate the aerodynamic performance of flapping wings. In a study by Seshadri et al., a four-bar linkage mechanism was used to generate large amplitude three-dimensional rotation of a flexible wing [42]. A six-component transducer was used to measure aerodynamic forces as the wing flapped. Single-axis vacuum tests were performed to decouple inertial and aerodynamic forces. Another study by Deng et al. characterized the aerodynamic performance of the DelFly Micro [43]. The wings of the DelFly Micro were actuated by a motor-driven linkage mechanism, and the body orientation was varied via a motorized strut. Experiments were conducted both in a wind tunnel and vacuum to decouple inertial and aerodynamic forces. Lift and thrust of the DelFly Micro were evaluated over a large parameter space. Both of these studies have significantly advanced the knowledge on aerodynamic wing performance and the decoupling of aerodynamic and inertial forces while considering realistically large rotation angles. However, wing root strain was not explicitly investigated in either study, thereby limiting their utility in the development of strain-based control mechanisms. Moreover, the rotation trajectories in both cases were limited by the use of linkage mechanisms to drive the wings.

In a smaller subset of experimental work, researchers have sought to characterize the temporal strain in flapping wings. Standord et al. utilized a single-degree of freedom actuator to flap a flexible wing in air at large amplitudes [44]. Digital image correlation (DIC) was used to measure the wing-tip deformation. By limiting the experiment to a single-degree of a freedom, effects of multi-rotational coupling cannot be explored. In experimental work

by Eberle et al., a two-axis rotation stage was used to generate rotations of a thin plate of uniform thickness in air [45]. The primary axis was used to simulate the flapping motion of the wing, whereas the secondary axes was used to simulate a yaw body rotation. Strain at the wing root was measured using a strain gage. However, the flap amplitude use was considerably smaller than the realistically large amplitudes found in insect flight. Furthermore, the pitch rotation was not considered, which is an important mechanism in generating lift and thrust in both insects and FWMAVs [46] and may significantly impact the wing root strain. Lastly, the experiment was conducted in air so that the contributions of aerodynamic, inertial and gyroscopic forces could not be easily decoupled.

The experimental work discussed in this chapter serves to synthesize the desirable characteristics of the aforementioned experimental work while simultaneously validating the model described in Chapter 2. A two-axis rotation stage is constructed to allow investigation of a wing subject to realistically large amplitude coupled rotations. Independent control of each motor allows for highly precise and extremely versatile rotation profiles. During rotation, strain is measured at the wing root, thereby facilitating parametric studies that may be beneficial in designing strain-based control mechanisms in FWMAVs. Tests are conducted both in air and vacuum to provide a clear deconvolution of aerodynamic forces from inertial forces.

The remainder of this chapter is organized as follows. First, a detailed description of the experimental set-up is then given. Experimental results are presented and meaningful trends are discussed. Finally, concluding remarks are made on how this inertial-elastic wing model may benefit FWMAV designers moving forth.

3.1 Experimental Set-up

To conduct the experimental validation of the model, a custom two-axis rotation stage is constructed (Fig. 3.1). Because the stage only allows for two simultaneous rotations, the model will be validated two rotation configurations at a time (i.e., pitch-yaw, roll-yaw, pitch-roll). All structural components of the rotation stage are constructed of 6061-T6 aluminum.

The components of the structure are thick and rigid to mitigate potential vibrations of the rotation stage itself. A mechanism is fixed to the primary axis of rotation to provide a clamped boundary condition for the wing.

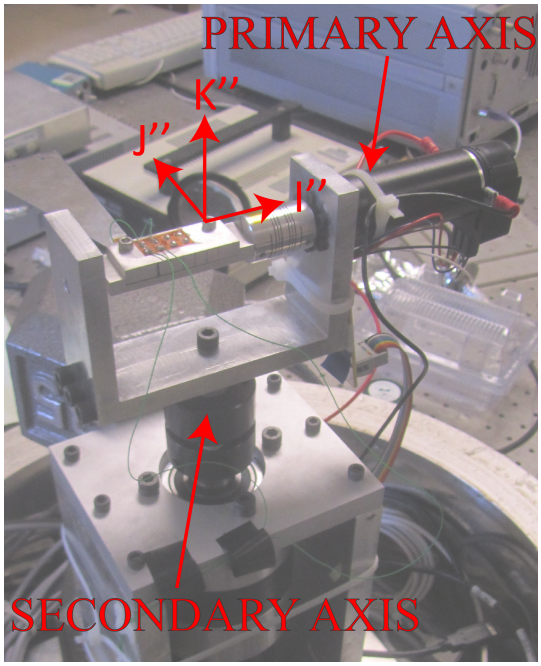

Figure 3.1: Picture of two-axis rotation stage.

Two high quality brushed DC motors purchased through Maxon Motors generate the motion of the rotation stage. The primary motor is a 60 W, 24 VDC (part. no. 310007) with a nominal speed and torque of 8050 rpm and 85.6 mNm, respectively. The secondary motor is a 250 W, 48 VDC (part. no. 353297) with a nominal speed and torque of 3340 rpm and 722 mNm, respectively. The secondary motor is equipped with a ceramic planetary gearhead (part. no. 110408) with a gear reduction ratio of 3.7, allowing a nominal torque of 2671 mNm and reducing the nominal speed to 903 rpm. Both motors are equipped with HEDS optical encoders with a resolution of 2000 qc/revolution.

The high level actuation/measurement structure of the experiment is shown in Figure 3.2. First, the actuation structure of the experiment will be discussed. A Lenovo W530 running

Labview software is used to monitor all inputs and outputs of the system. A more detailed description of the Labview Virtual Instrument (VI) is given Section 3.1.1. The PC is connected to one of two positioning motor controls via USB. The first motor controller is an EPOS2 24/5 (part. no. 367676) and allows for a 5A nominal current draw at 24 VDC. This controller is powered by a 24 VDC, 5A regulated power supply, and is responsible for communicating with the 60 W motor. A second motor controller communicates with the first via a high-speed CAN-CAN connection. This controller is an EPOS2 70/10 (part. no. 375711) and allows for a nominal current draw of 10A at 48 VDC. This controller is powered by a 48 VDC, 10A regulated power supply, and communicates with the 250 W motor. The ground

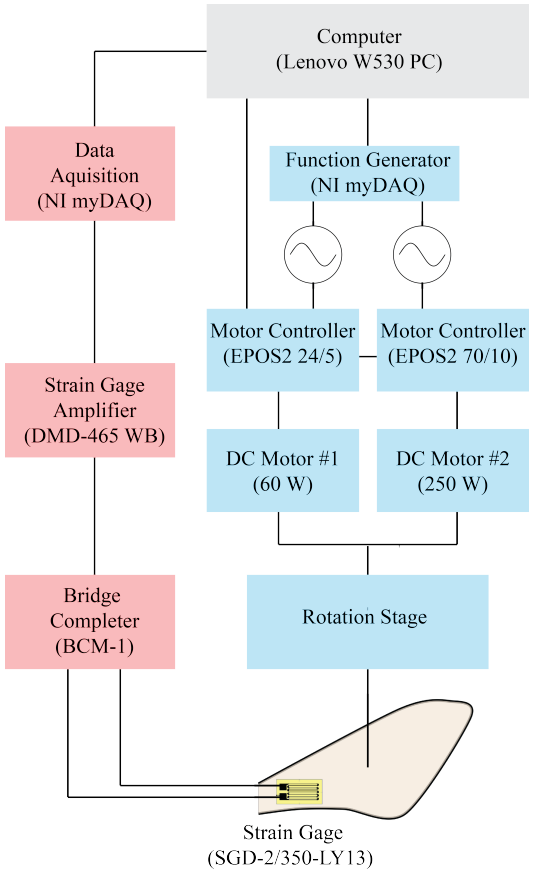

Figure 3.2: Flow chart describing actuation (blue) and measurement (red) structures of experiment.

terminal of each power supply are connected together- doing so was found to minimize signal noise.

Both controllers allow for PID position control of their respective motors. The PID gains are determined automatically using provided Maxon EPOS Studio software. Furthermore, velocity and acceleration feed-forward control are implemented to compensate for inertial loads and speed-dependent friction. The controllers receive position information from the HEDS optical encoders mounted on each motor shaft at a rate of 1 kHz. Analog position commands are sent to each controller as a voltage signal (between 0-5 V) using the National Instruments NI myDAQ function generator. This actuation scheme was found to produce highly repeatable and fairly accurate rotation profiles of the two-axis rotation stage.

The measurement structure of the system is now described. All strain measurement components are provided by Omega Engineering. A uniaxial, two-lead, 350Ω strain gage (part. no. SGD-2/350-LY13) is bonded to a wing near the base in the spanwise direction. The specifics of the wing are discussed in the next section. As the system operates in ambient conditions and the lead wires are relatively short, no temperature or lead wire compensation was implemented. The two lead wires of the strain gage are attached to a bridge completion module (part. no. BCM-1) to complete the quarter-bridge Wheatstone bridge circuit. The zero knob on the BCM-1 is used to balance the bridge and define the no strain condition.

The output of the BCM-1 is attached to the input of a strain gage amplifier (part. no. DMD-465WB) to amplify the voltage signal. The strain gage amplifier is capable of measuring frequencies up to 2 kHz, and is fitted with a 200 Hz analog low-pass filter. After the BMC-1 is balanced, the amplifier offset is set to zero for the no strain condition. A shunt resistor is then applied to the BCM-1 to simulate a full-scale load and the amplifier gain is adjusted to provide increased sensitivity. A wiring schematic between the strain gage, amplifier and bridge completion module is shown in Figure 3.3.

The output of the amplifier is connected to a data acquisition module (NI myDAQ). Voltage measurements are acquired at a sampling rate of 1 kHz. The acquired voltage data

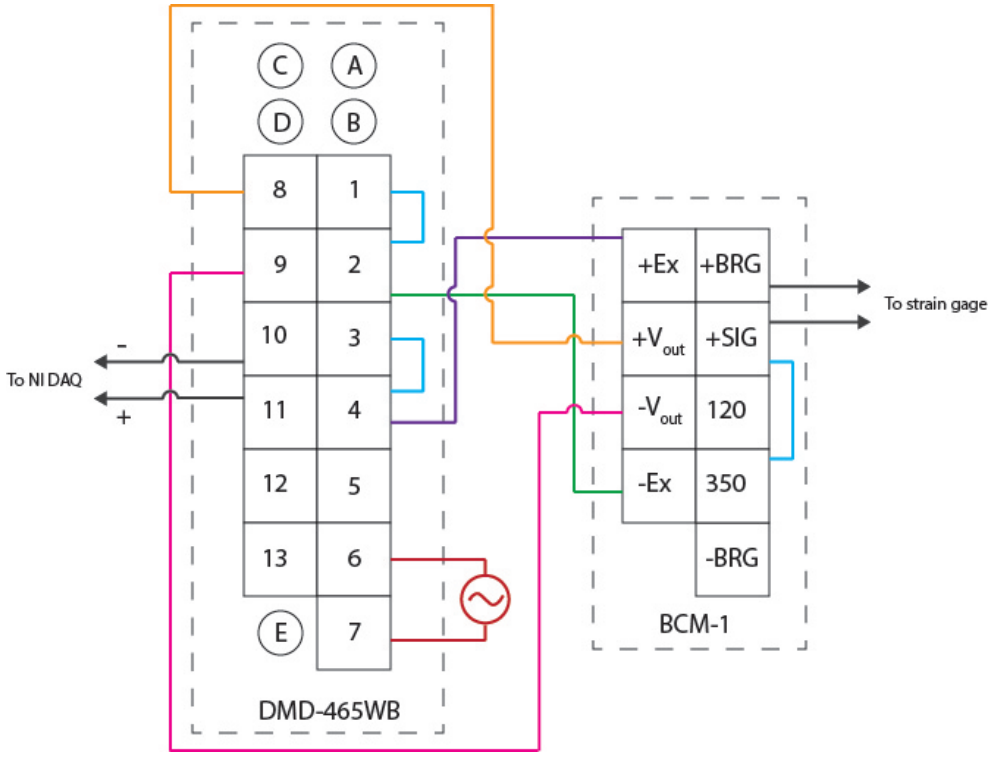

Figure 3.3: Wiring schematic of strain measurement equipment

can the be interpreted into strain data by

$$\epsilon = \frac{4V}{(BV)(GF)(AG)} \tag{3.1}$$

where the variables above and their corresponding values are described by Table 3.1.

Lastly, a custom vacuum chamber operating at a nominal pressure of 200 milliTorr houses the entire experimental apparatus, including instrumentation (Fig. 3.4). Power feed-through ports are used to provide DC and AC power to the motor controllers and strain gage amplifier, whereas USB feed-through ports are used to communicate with the motor controllers and DAQ. All vacuum components are provided by Kurt J. Lesker company.

Symbol	Description	Value
BV	Bridge Excitation Voltage	5 V
GF	Gage Factor	2.14
AG	Amplifier Gain	175
V	Output Voltage	Variable

Table 3.1: Strain Gage Measurement Settings

3.1.1 Labview VI

The Labview VI is necessary for running the experimental set-up. The VI is made up of two parts- the front panel and the block diagram. The front panel is where high-level commands are input, such as motor frequency, rotation amplitude, etc. Should a user want to repeat the

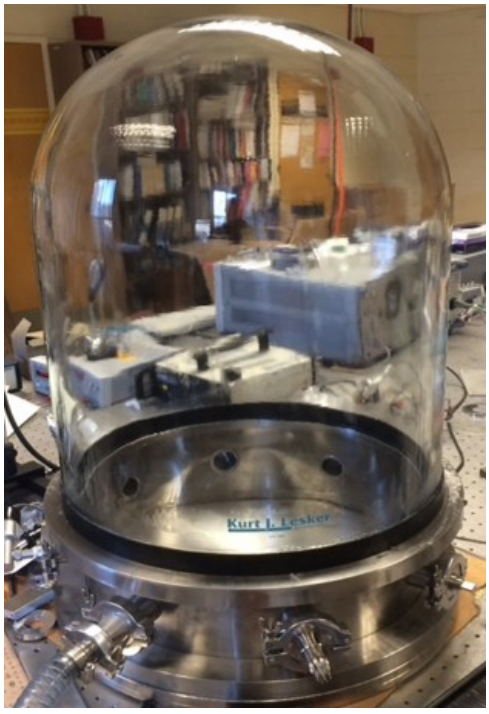

Figure 3.4: Vacuum enclosure to house rotation stage

experiment outlined in this chapter, the user need only to interact with the VI front panel. The block diagram is where low-level commands are implemented. The block diagram is where the motors and controllers are initialized, analog voltage commands to the DAQ are created, and measurement settings are established.

The VI front panel is shown in Figure 3.5. The "communication settings in" tab configures the parameters necessary to communicate with the two EPOS motor controllers. Assuming the USB connection is used, the default settings shown are appropriate. The "nodeID" box immediately below the communication settings are used as an identifier for the motor-1 corresponds to the primary motor, whereas 2 corresponds to the secondary motor. The "profile position" tab sets a maximum and velocity for the initial motion of the motor. That is, when the experiment is initialized, the motors will slowly return to the default position

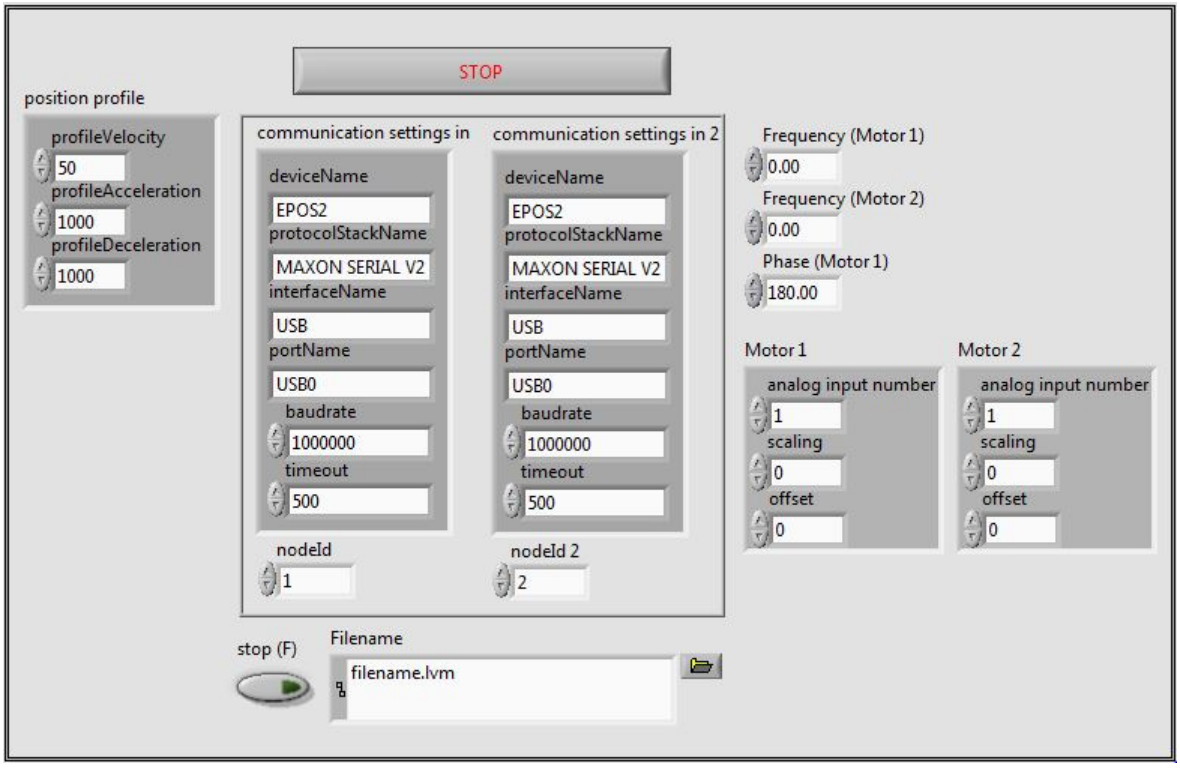

Figure 3.5: Front panel of the experimental Labview VI

at a velocity dictated by the "position profile" tab. The default position of the motors is the configuration the motors are in when power is initially supplied to the motor controllers. Again, it is recommended the default values be used. The "filename" box is where a unique file name should be input. The resulting file is generated automatically as the VI is run and will include voltage data corresponding to strain as well as pertinent motor information (position, velocity and current draw).

The "frequency" inputs independently control the oscillation frequency in Hz of each motor. The default frequency is set to 0 Hz, and must be set to the desired frequency (in this case, 5 Hz) prior to running the experiment. The "phase" tab modulates the phase of the primary motor, and can be used to introduce a phase difference (in degrees) between the two rotations. Due to the specifications of the motors and the physical design of the rotation stage, a phase of 180° corresponds to a case where the motors are completely in-phase and a phase of 0° corresponds to a case where the motors are completely out-of-phase. The "scaling" and "offset" tabs are used to configure the rotation amplitude. The "scaling" tab identifies to entire rotation range divided by the maximum analog input voltage (5 V) of the DAQ to the motor controller. For example, if a rotation amplitude of 100 qc is desired (corresponding to a total range of 200 qc), where 2000 qc = 2π rad, the scaling tab should be set to 40 qc/V. The "offset" tab is then used to set the initial position of the motor corresponding to zero voltage. As the analog voltage varies between 0-5V, the "offset" should correspond to the minimum position of the motor. Again, assuming a rotation amplitude of 100 qc is desired, the "offset" tab should be set to -100 qc such 0 V corresponds to -100 qc, 2.5 V corresponds to 0 qc and 5 V corresponds to 100 qc. It should be noted that the secondary motor is equipped with a planetary gearhead with a reduction ratio of 3.8:1- this must be taken into account when considering the rotation amplitude of this motor. After all desired settings are established and the experimental set-up has been powered on, simply hit "run" on the VI. The motors will begin to move and strain data will be collected automatically. The green stop button will halt data collection, whereas the red stop button will halt the motors.

Should the user want to modify the experiment, it will be necessary to modify the block diagram shown in Figure 3.6. The block diagram is broken into four components, separated by a flat sequence structure. The sequence structure simply means all commands within a cell must be completed before the VI executes the subsequent cell. The block diagram consists of many subVI's, some of which are standard to Labview, others which are provided through the Maxon EPOS motor controller library.

Cells 1-3 in Figure 3.6 represent the actuation structure of the VI. In cell 1, the communication settings from the front panel are used to initialize each motor using the "initialize" subVI. Next, all errors are cleared and the motor is set to the enabled state using the "EnableAxis" subVI. The status LEDs on the EPOS motor controllers will turn from red to green

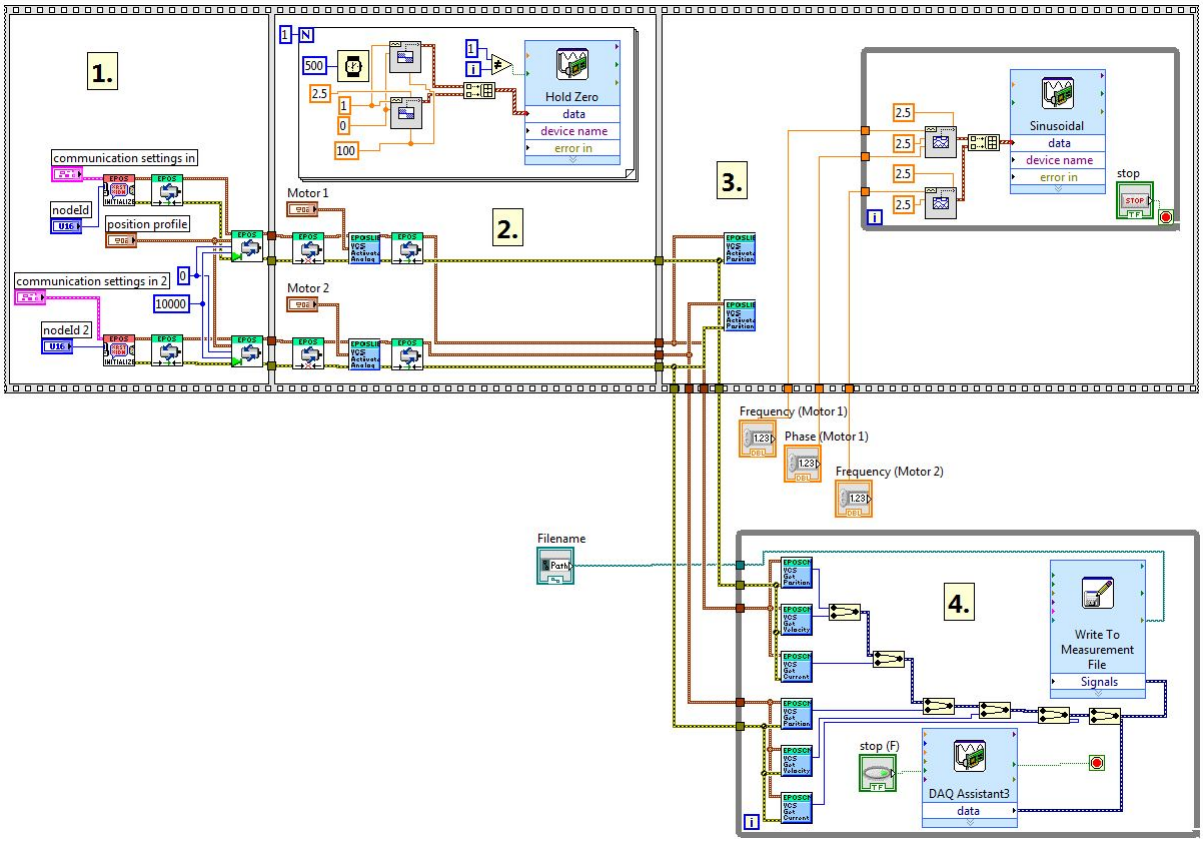

Figure 3.6: Block diagram of the experimental Labview VI

if all errors are resolved. With both axes enabled for motion, the "MoveToAbsolutePosition" VI is employed to return the motors to their positions. The velocity at which this motion occurs is limited by the position profile settings on the front panel.

After cell 1 has completely executed, the commands in cell 2 are initialized. Both axes are temporarily disabled with the "DisableAxis" VI. Disabling the axes allows for the analog position setpoint configuration, which are dictated by the "scaling" and "offset" parameters on the front panel. After the analog setpoint parameters are initialized, the axes are the re-enabled. During this process, a constant 2.5 V is supplied to the motor controllers from the DAQ using a for-loop with a single iteration that last 500 ms. This is achieved by sending a square wave with a 100% duty cycle and 2.5 V offset and 0 V amplitude to the "DAQ Assistant" VI. It is important that this 2.5 V be maintained moving into cell 3- otherwise, an initial zero voltage will cause the motors to jump to their extreme positions rather than remaining at their default position.

Moving into cell 3, the analog position mode for each motor is enabled using the "ActivatePositionMode" subVI. The motors are now permitted to move when subjected to an analog voltage. A while-loop is introduced in this cell, which includes the software function generator controlling the voltage signal produced by the "DAQ Assistant" VI. A sinusoidal signal with an offset of 2.5 V and amplitude of 2.5 V is produced by the DAQ, creating a sine wave oscillating between 0 and 5 V. The frequency and amplitude of the resulting motor rotation are functions of the frequency and scaling inputs found on the front panel. The motors will continue oscillating sinusoidally until the while-loop is terminated by pressing the red stop button on the front panel.

Cell 4 includes the measurement structure of the Labview VI, and operates in parallel to Cell 3. Axes wires from the flat sequence structure are connected to subVI's in cell 4 to record the position, velocity and current draw of both of the motors. Furthermore, the same "DAQ Assistant" VI is used to take voltage measurements from the strain gage amplifier. Voltage measurements are acquired at 1 kHz, whereas motor measurements are taken at a rate of 100 Hz. It is important to recognize that the motor data may become distorted in

time if all parameters (position, velocity and current draw) are requested. This distortion can be alleviated by removing one or more of the requests. Nonetheless, the acquired motor data serves as a good indicator for peak values, such as peak rotational position. Cell 4 also occurs within a while-loop, and therefore will continue recording data until the green stop button on the front panel is pushed. It will not begin recording data until the motors begin moving in Cell 3.

3.1.2 Motor Harmonic Characterization

One challenge in this experimental work is characterizing the higher-order harmonic vibrations induced by the motors and/or the shaft coupling. While the position/velocity following capabilities are quite accurate, the motor angular acceleration tends to cause higher-order harmonic vibrations at integer multiples of the driving frequency. These harmonics are observed in the wing strain both in air and in vacuum and are approximately proportional to the harmonics of the motor current, which strongly suggests they are induced by electromotive forces (EMF). Harmonics associated with the angular acceleration term are consistent with the research presented by Seshadri et al [42]. Moreover, asymmetric shafts tend to generate vibrations at twice the spin speed. These vibrations are more pronounced if the shaft couple between the secondary motor and the U-bracket is not perfectly rigid.

As the work in this paper intends to characterize forces acting at twice the driving frequency, a baseline for the motor related harmonics must be established. Growth of the second harmonic above this baseline is assumed to be due to gyroscopic forces. To determine the baseline for a multi-rotational configuration, the primary motor is actuated independently at the flap frequency, and the magnitude of the second harmonic is recorded. Both motors are then actuated together, with the secondary motor at the flap frequency, and the primary motor a reduced frequency. The magnitude of the second harmonic of the driving frequency in this state is assumed to be due to the secondary motor. The contribution to the second harmonic from each motor is summed together to establish a baseline value. All reported values in this work show the growth of the second harmonic peak above this baseline.

3.2 Results

In this section, the results of the experiment are presented. All rotations are purely sinusoidal with a driving frequency of ω=5 Hz and occur in-phase. The rotation amplitudes are discussed in each subsection. The FFT of the strain signal is taken, and the magnitude of the strain components are evaluated. Each data point represents the average value of five trials. Each set of trials were found to be extremely consistent and repeatable with a low standard deviation. Therefore, no error bars are shown on the results. After the results are presented, a separate section discusses potential sources of error.

3.2.1 Structural Modeling

In practice, most insect wings have complex geometry and spatially varying stiffness [47]. As a result, a real insect wing is not conducive to the experimental validation of this model. Instead, a thin aluminum triangular wing is constructed with the geometry and material properties shown in Table 3.2.

Symbol	Description	Value	Units
E	Young's Modulus	68.9	GPa
ν	Poisson's Ratio	0.33	-
ρ	Density	2700	kg/m^3
W	Chord Width	3.8	cm
L	Span Length	11.4	cm
t	Thickness	0.42	mm

Table 3.2: Triangular wing material properties and geometry

A finite element model is created using Abaqus CAE to determine the natural frequencies, mode shapes and modal strains of the described wing. A fixed boundary condition was

created to simulate the clamped edge, which clamps the entire triangular area approximately 1.9 cm from the wing base.

For the purposes of this experiment, only the first two structural modes of the wing are considered. Higher modes were determined to have a negligible effect on the strain in the spanwise direction. Finite element analysis predicts the first mode as a bending mode and the second mode as a torsional mode (Fig. 3.7), with natural frequencies of $\omega_1 = 20.5$ Hz and $\omega_2 = 146$ Hz, respectively. To validate the accuracy of the finite element results, a test was performed by deflecting the wing tip and allowing the wing to vibrate freely in air. No significant change in natural frequency was found in vacuum. The results are shown in Figure 3.8. The experimentally determined natural frequencies are $\omega_1 = 20.0$ Hz and $\omega_2 = 140.6$ Hz, which agree reasonably well with the finite element predictions. Experimental natural frequencies are used in the theoretical model.

3.2.2 Single-Axis Rotations

An initial set of single-axis rotation tests are conducted to assess how well the strain magnitudes agree with theoretic predictions. In these tests, only inertial and aerodynamic forces are present. The wing is held in a vertical orientation during both tests. The primary motor

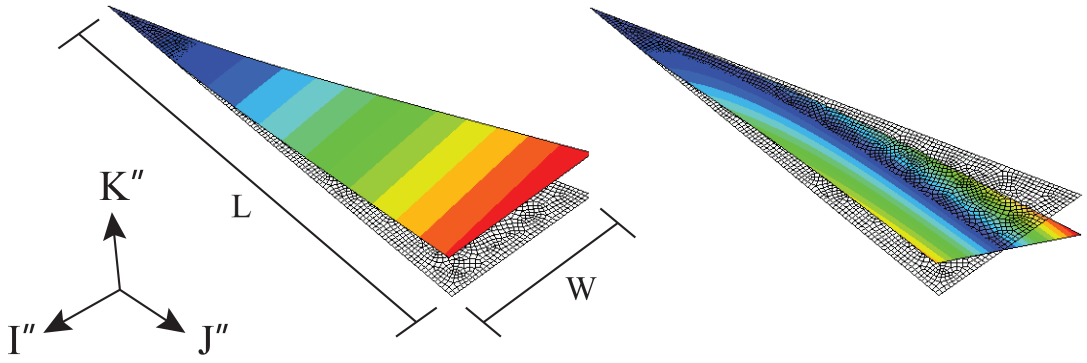

Figure 3.7: First bending mode (left) and first torsional mode (right) of triangular wing superimposed on undeformed geometry.

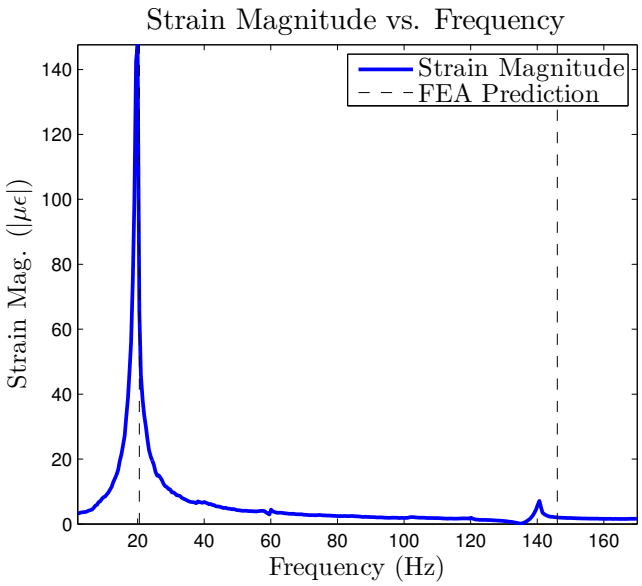

Figure 3.8: Free vibration strain magnitude plot with FEA natural frequency predictions.

controls roll, whereas the secondary motor controls pitch. The wing is offset 2.5 cm from the center of rotation in the negative I'' direction, which does not affect the strain magnitude of the roll rotation but significantly increases inertial forces of the pitch rotation. The pitch amplitude is varied from 0°-35° while the roll amplitude is varied from 0°-60° to reflect the large amplitude rotations of the *Manduca sexta* forewing. Strain magnitude is evaluated as a function of the rotation amplitude. Results are shown in Figure 3.9-3.10.

The experimental results agree well with theoretic predictions for the pitch rotation, with a maximum errors of 9.4% and 15.7% in air and vacuum, respectively. Theoretic predictions for the roll rotation are less accurate, with maximum errors of 20.8% in air and 17.7% in vacuum. This disparity is believed to be due to gravity, and will be discussed further in the error analysis section.

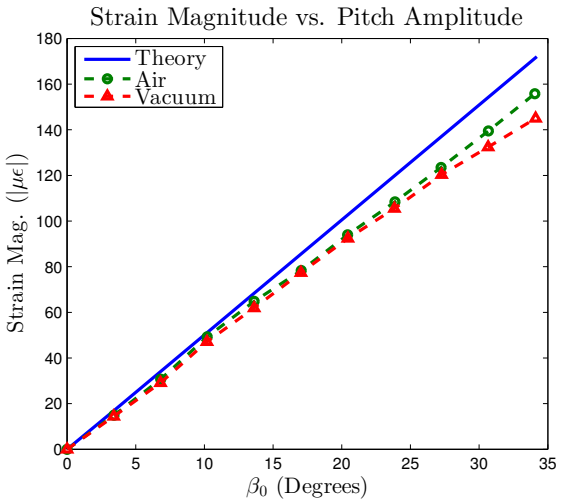

Figure 3.9: Pitch orientation.

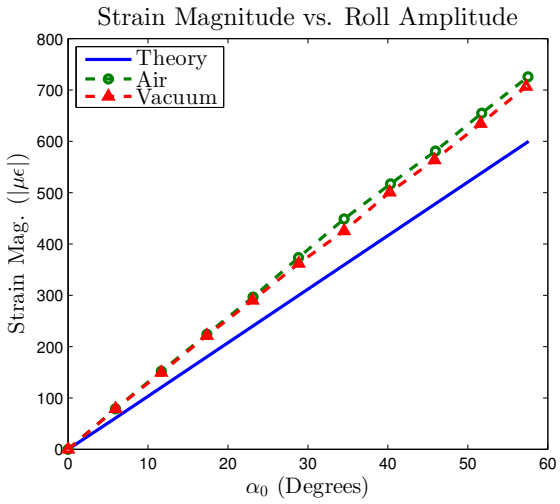

Figure 3.10: Roll orientation.

3.2.3 Pitch-Roll Orientation

In the pitch-roll orientation, our theory suggests dynamic bending will arise from inertial forces at a frequency of ω with a minor contribution of the centrifugal force at 3ω. For this reason, only the trends of the inertial forces will be verified.

The wing is offset 2.5 cm in the negative I'' direction and held upright. The primary motor controls roll while the secondary motor simultaneously controls pitch. The roll amplitude is set to a constant 29° and the pitch amplitude is varied between 0°-23°. The magnitude of the inertial force at ω is evaluated for each pitch angle (Fig.3.11). Inertial forces dominate aerodynamic forces in this configuration, with aerodynamic forces contributing only 5% to the total strain magnitude.

3.2.4 Roll-Yaw Orientation

Next, the roll-yaw orientation is considered. In this configuration, the theory predicts both gyroscopic and inertial forces will be present, with gyroscopic forces generated by the yaw rotation at 2ω. The wing is rotated into the horizontal position such that the secondary

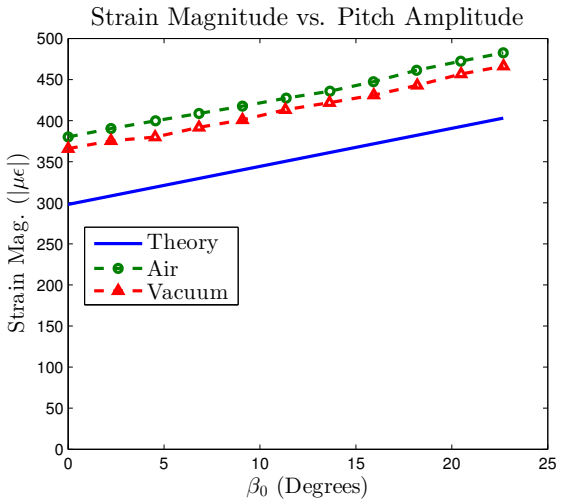

Figure 3.11: Pitch-Roll orientation.

motor now actuates the yaw rotation while the primary motor still drives the roll rotation. The same boundary condition is maintained between pitch-roll and roll-yaw trials to ensure consistent results. The 2.5 cm offset in the negative I'' direction serves to amplify gyroscope forces. The roll amplitude is maintained at 29°, and the yaw amplitude is varied from 0°-23°. The magnitude of the strain at ω and 2ω are evaluated as a function of the yaw amplitude (Fig. 3.12).

The agreement between theoretical and experimental results for the ω magnitude are fairly accurate, while the error for the 2ω magnitude is more significant. The purported cause of the discrepancy is interaction between the gyroscopic forces and the unavoidable harmonics generated by the EMFs of the motors. This will be discussed in detail in the error analysis section. Consistent with the other results, the vacuum tends to decrease the magnitude of the strain by a small percentage, both at ω and 2ω frequencies.

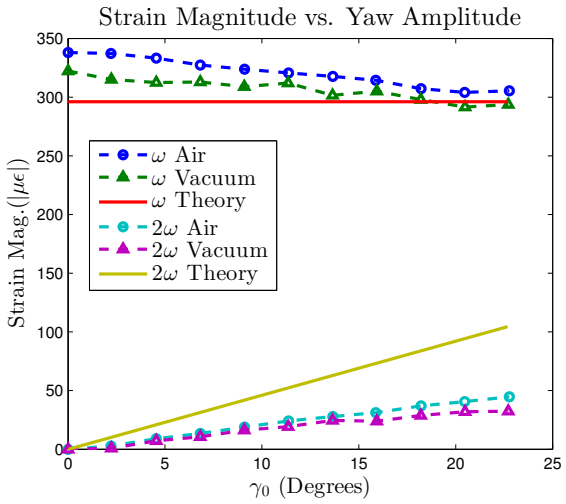

Figure 3.12: Roll-Yaw orientation.

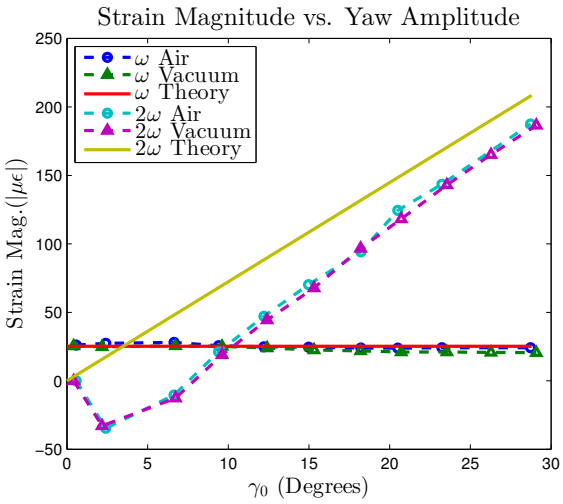

Figure 3.13: Pitch-Yaw orientation.

3.2.5 Pitch-Yaw Orientation

The final orientation considered is the pitch-yaw orientation. In this orientation, inertial and gyroscopic forces are predicted by theory. As the yaw amplitude increases, gyroscopic forces are expected to dominate inertial forces.

An adapter added to the clamping mechanism is used to hold the wing upright and perpendicular to the primary axis (Fig. 3.15). The adapter causes an offset 1.9 cm in the positive J'' direction and 0.5 cm in the negative I'' direction. In this configuration, the primary motor controls yaw, whereas the secondary motor controls pitch. A pitch angle of 18° is maintained, and the yaw angle is varied between 0°-29°. The magnitude of the strain at ω and 2ω are evaluated as a function of the yaw amplitude (Fig. 3.13).

In the pitch-yaw configuration, the model accurately predicts the inertial forces at frequency ω, with maximum percent errors of 12% and 25% in air and vacuum, respectively. The maximum errors occur at relatively large yaw amplitudes, which are unrealistic in actual insect flight. Within the typical yaw range of the *Manduca sexta*, the agreement is much stronger. Interestingly, the 2ω component of strain drops below the baseline for small yaw amplitudes, suggesting destructive interference between gyroscopic forces and other unac-

counted for vibrations. This will be discussed in detail in the error analysis section. Again, the vacuum chamber only slightly reduces magnitude of the strain at ω and 2ω, indicating inertial/gyroscopic forces tend to dominate aerodynamic forces.

3.2.6 Error Analysis

While most the experimental results match theoretic predictions fairly well, there are some potential sources of error. For example, gravity effects seem to amplify the strain when the wing is held in the vertical configuration although no nonlinear trends are observed (Fig. 3.11). This in part suggests why the pitch agreement is better, as gravity will have a lesser impact on the strain (Fig. 3.9). To corroborate this assertion, a simple static FEA simulation was conducted holding the wing at 60° from the vertical under the influence of gravity (Fig. 3.14). The simulation shows a strain of nearly 60×10^{-6} at the strain gage location, which may significantly affect the agreement between theoretical predictions and experimental results.

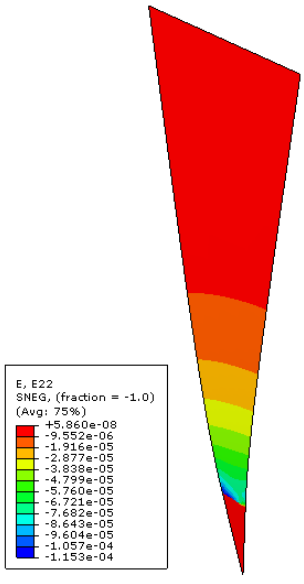

Figure 3.14: Static FEA simulation.

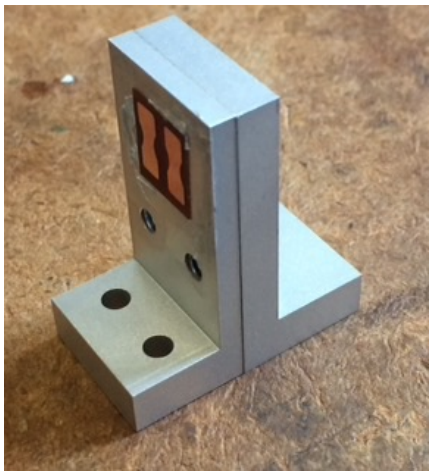

Figure 3.15: Pitch-Yaw adapter.

Next, some nonlinear behavior is observed in the strain at ω in Figure 3.9. It is estimated that during the trials the wing-tip deflection is as large as 11 mm, which is significantly larger than the wing thickness. As a result, structural stiffness softening behavior is likely occurring, particularly with large amplitude rotations.

Lastly, there is a consistent over prediction of the strain magnitude at 2ω in the roll-yaw and pitch yaw configurations (Fig. 3.12,3.13). The purported reason for this discrepancy is destructive interference between the U-bracket (Fig. 3.1) and the gyroscopic forces acting at 2ω. In fact, this interference causes the perceived gyroscopic forces to fall below the baseline value for small yaw amplitudes in the pitch-yaw configuration (Fig. 3.13). Two approaches are used to reconcile these differences. First, for both the pitch-roll and roll-yaw configurations, the primary rotation frequency is maintained at 5 Hz while the yaw frequency is reduced to 3 Hz. In this case, the gyroscopic splitting predicts strain at 2 Hz and 8 Hz, which fall at different frequencies than the U-bracket vibrations. A simple in-air test is conducted using these parameters, and the results are shown in Figure3.16. The prediction of the strain induced by gyroscopic forces is significantly better, indicating bracket vibrations indeed interfere with gyroscopic forces when the motors are at the same frequency.

Alternatively, the phase difference between the U-bracket and the gyroscopic forces can be explored. This is a challenging task, as the only measure of the gyroscopic force is from the strain which also includes the contribution from the vibrating bracket. The vibrations from the bracket are measured directly by fixing a piezoelectric accelerometer to the outer edge of the bracket. The pitch-yaw configuration is used in air, with a pitch amplitude of 18° and a yaw amplitude of 2.5°. First, the primary motor is driven at the 3 Hz while the secondary motor is driven at 5 Hz. Then, both motors are driven at 5 Hz. Fourier fits of both the strain and bracket acceleration data are taken, and the phase difference is investigated for both cases. Figure 3.17 shows a phase jump of 2π rad at 10 Hz, showing the

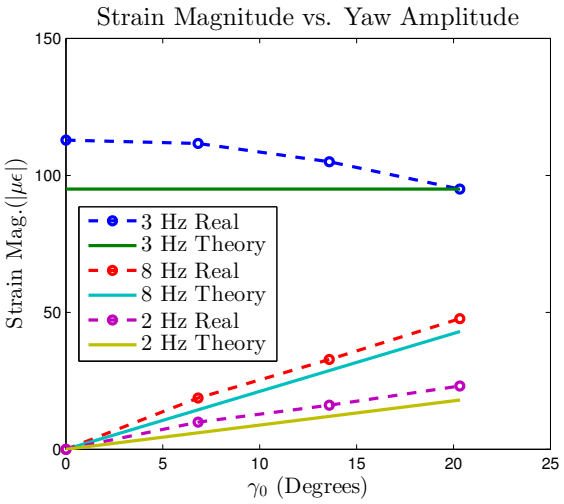

Figure 3.16a: Roll-yaw orientation

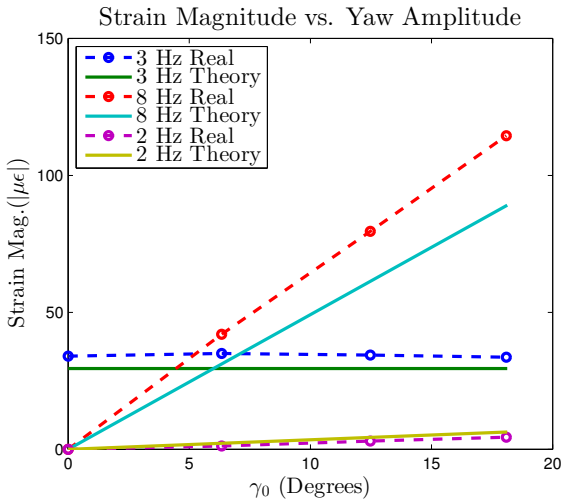

Figure 3.16b: Pitch-yaw configuration

Figure 3.16: In-air trials with primary rotation at 3 Hz and secondary 5 Hz predicting gyroscopic splitting at 2 Hz and 8 Hz

bracket vibrations and strain are in phase in this configuration. This suggests that all 10 Hz frequency content in the strain is a result of bracket vibrations. Figure 3.2.6 shows a phase jump of approximately 2.36 rad when both motors are driven at 5 Hz, indicating there is some phase difference between the gyroscopic forces and bracket acceleration. This in part describes why the 2ω peak falls below the baseline value in Figure 3.13.

3.3 Discussion

There are numerous important implications of the experimental research presented. First, the work suggests that an inertial-elastic approximation of a wing provides reasonable quantitative strain estimates in certain contexts. While the wing discussed is not representative of an actual insect wing and is driven at lower flap frequencies, there exists evidence in biology that suggests inertial forces tend to dominate aerodynamic forces in some insect wings [26].

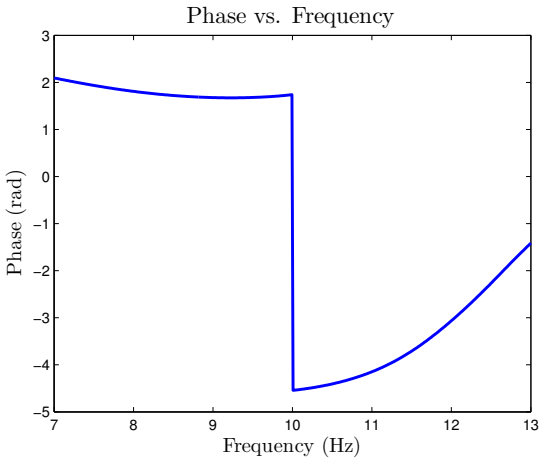

Figure 3.17a: Primary motor at 3 Hz

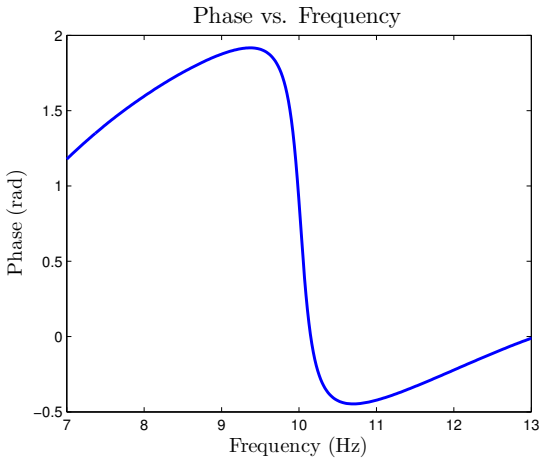

Figure 3.17b: Primary motor at 5 Hz

Figure 3.17: Phase difference between strain and bracket acceleration for motors at unmatched driving frequency (a) and matched driving frequency (b)

Consequently, the inertial-elastic model presented may serve as a good approximation in determining strain, either in the study of real insects or insect-inspired FWMAVs.

Secondly, the reduced-order model described utilizes only two degrees-of-freedom to estimate the strain within reasonable accuracy. This is a dramatic improvement over a rigorous FEA approach, which requires excessive computational resources. The inertial-elastic model may be beneficial in studies where a large parameter space is considered and minimizing computational load is preeminent. Moreover, the model may be extended to include more complex geometries, namely the geometry of a FWMAV forewing.

Lastly, it has been shown that gyroscopic forces indeed have a substantial effect on dynamic bending. While gyroscopic forces do excite torsional modes, the results presented show a more significant contribution of gyroscopic forces to bending modes, particularly as a result pitching. These gyroscopic forces related to the yawing wing were shown to occur at twice the driving frequency, which falls near the first resonance frequency of the *Manduca sexta* [39]. Even without the resonance phenomena, the experimental work shows gyroscopic

forces are as much as four times the inertial forces in the pitch-yaw orientation. Should the resonance phenomena be leveraged in the design of a FWMAV wing, it may be plausible to realize a highly sensitive strain-based gyroscope.

Chapter 4

THE EFFECT OF AERODYNAMIC AND INERTIAL TORQUES ON STEERING

There exists a plethora of observational evidence in biology that strongly correlates steering muscle activity to various changes in body orientation. For instance, bilateral actuation of the third axillary muscles (3AXM) in moths has been found to adjust body pitch angle [1, 48]. Asymmetric stimulation of the 3AXM muscle in beetles in free flight was found to induce banked turns [2]. Balint and Dickinson [49] observed steering muscle activity correlated to variations in the stroke deviation angle in blowflys. Similarly, variant steering muscle firing patterns were found to modulate stroke deviation in hawkmoths [48]. By extension, it seems steering muscles and consequently the stroke deviation angle have pronounced influence on body attitude.

The literature aerodynamic models describe the complex unsteady flow past flapping wings [50, 51, 52]. These models have been used to describe various aerial maneuvers, claiming shifts in the wings pressure center relative to the insect center of mass can be used to pitch the insect body forward, for example. However, these models often neglect the stroke deviation angle [53, 54], and the role of inertial moments on the insect body orientation has not been explored in great detail. There exist at least some biological precedents which suggest inertial forces facilitate posture control in various organisms. For example, bats are believed adjust their heading angle by creating imbalances in inertial forces between their wings [55]. Dyhr et al. concluded abdominal flexion in the Hawkmoth *Manduca sexta* can effectively redirect lift forces [56]. Thus, there exists at least some evidence that inertial forces can play an important role in airborne insect steering – the relative role of inertial and aerodynamic forces that arise from changes in stroke deviation remains unexplored.

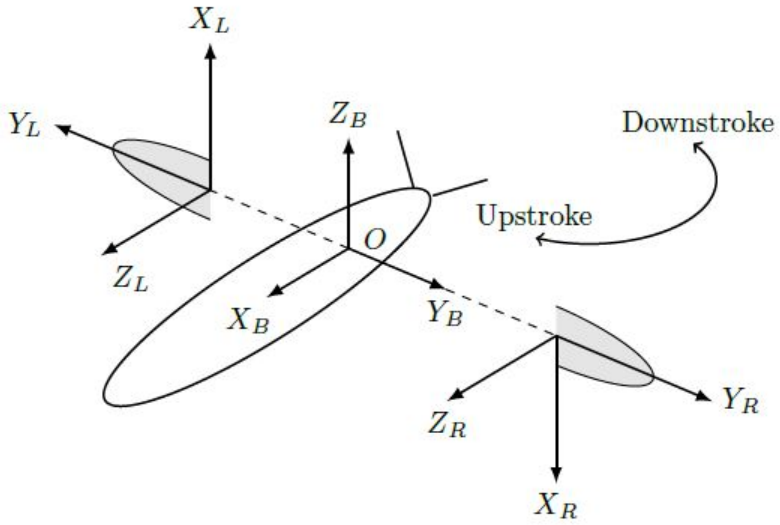

Figure 4.1: Left wing, right wing and body inertial coordinate frames.

This chapter examines the effect the stroke deviation angle has on net torque production during turning. To do so, a simple model that integrates aerodynamic and inertial dynamics of two rigid wings rotating about a single fixed point is developed. The effect stroke deviation phase has on net force and moment production is explored in depth. Temporal shifts in stroke deviation phase are looked at such that aerodynamic and inertial impulses and insect body yaw rate can be compared for various timed phase transitions. Finally, the results are compared to observational results in biology and some concluding remarks are made on how these findings may benefit FWMAV drive-train and control system design.

4.1 Methods

We establish an idealized relationship between two wings and the insect body, leveraging a wing-bound reference frame to prescribe kinematics. Inertial moments are derived through the wing angular momentum. A simplified blade element aerodynamic model is introduced to estimate aerodynamic forces and moments. The integrated aerodynamic/inertial model is linearized about the infinitesimal stroke deviation angle such that order analysis can be

employed.

4.1.1 Wing-Body Inertial Frames

Three sets of coordinate frames as shown in Figure 4.1 are introduced to represent the inertial frame of the left wing ($X_L Y_L Z_L$), right wing ($X_R Y_R Z_R$) and insect/FWMAV body frame ($X_B Y_B Z_B$). Both wings attach to the body at a fixed point O – they are shown offset from the body in Fig. 4.1. This idealization serves as an approximation for estimating how forces and moments acting on the wings are transmitted to the body. Given the fixed point O on the insect body, this configuration most closely resembles hovering flight. For brevity, the equations of motion will only be formulated for the right wing. For the remainder of the paper, unless otherwise specified, the inertial frame of the right wing is labeled XYZ. Symmetry arguments are employed to determine how the moments and forces generated by the left wing affect the net moments and forces acting on the body at fixed point O.

4.1.2 Reference Frame Kinematics

A body-fixed reference frame that rotates with the rigid wing about a fixed point O is established (Fig. 4.2). An inertial reference frame (XYZ) is rotated about the positive X axis by an amplitude α, where α denotes wing roll. The subsequent reference frame ($x''y''z''$) is rotated about the positive y'' axis by an amplitude β, where β denotes wing pitch. A final rotation of amplitude γ occurs about the positive z' axis in the $x'y'z'$ frame, where γ represents the stroke deviation angle. The result of the transformation is the wing-bound xyz reference frame. The angular velocity $\vec{\Omega}$ of the reference frame is expressed as

$$\vec{\Omega} = \dot{\alpha}\hat{e}_{x''} + \dot{\beta}\hat{e}_{y'} + \dot{\gamma}\hat{e}_z \tag{4.1}$$

where $\hat{e}_n$ represents a unit vector in the n direction. It is convenient to relate unit vectors in intermediate coordinate frames to unit vectors in the fully rotated xyz reference frame such that $\vec{\Omega}$ can be represented in terms of $\hat{e}_x - \hat{e}_y - \hat{e}_z$. In relating the unit vectors, the

expression for the angular velocity becomes

$$\vec{\Omega} = \underbrace{(\dot{\alpha}\cos\beta\cos\gamma + \dot{\beta}\sin\gamma)}_{\omega_x}\hat{e}_x + \underbrace{(\dot{\beta}\cos\gamma - \dot{\alpha}\cos\beta\sin\gamma)}_{\omega_y}\hat{e}_y + \underbrace{(\dot{\gamma} + \dot{\alpha}\sin\beta)}_{\omega_z}\hat{e}_z \tag{4.2}$$

Determining quantities (angular momentum, aerodynamic moments, etc.) in the fully rotated coordinate frame is relatively straightforward, whereas doing so in the inertial reference frame is challenging. However, in order to understand the relative forces/moments acting on the insect body, it is more suitable to represent quantities in a fixed inertial frame. An arbitrary vector quantity $\vec{A}$ can be represented in the inertial frame by the transformation

$$(\vec{A})_{XYZ} = \mathbf{R}^T(\vec{A})_{xyz} \tag{4.3}$$

where the rotation matrix $\mathbf{R}$ is given by

$$\mathbf{R} = \mathbf{R}_z\mathbf{R}_{y'}\mathbf{R}_{x''} \tag{4.4}$$

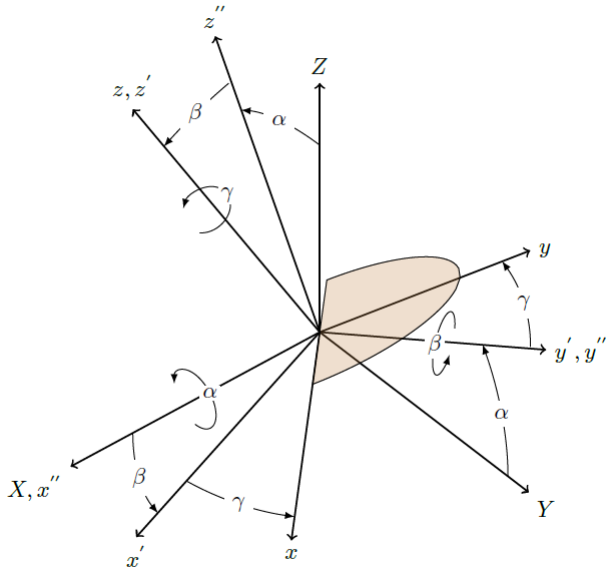

Figure 4.2: Establishing a wing-fixed reference frame

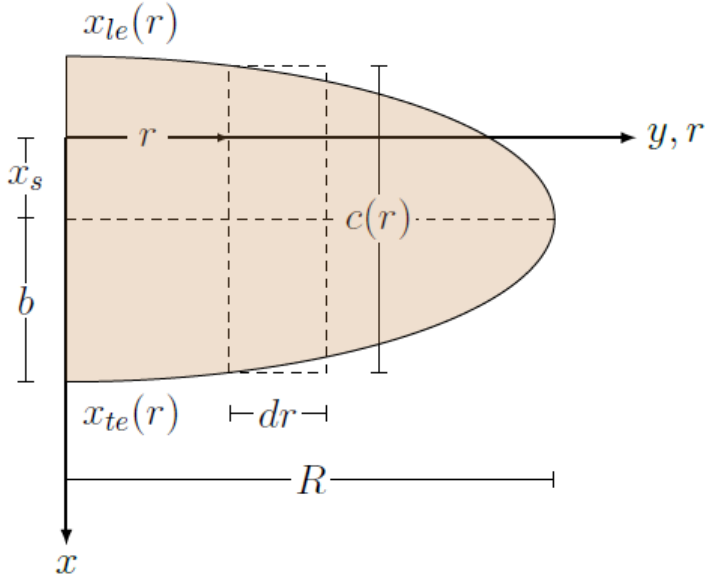

Figure 4.3: Schematic of wing with dimension definitions

$$\mathbf{R}_{x''} = \begin{bmatrix} 1 & 0 & 0 \\ 0 & \cos\alpha & \sin\alpha \\ 0 & -\sin\alpha & \cos\alpha \end{bmatrix} \quad \mathbf{R}_{y'} = \begin{bmatrix} \cos\beta & 0 & -\sin\beta \\ 0 & 1 & 0 \\ \sin\beta & 0 & \cos\beta \end{bmatrix} \quad \mathbf{R}_{z} = \begin{bmatrix} \cos\gamma & \sin\gamma & 0 \\ -\sin\gamma & \cos\gamma & 0 \\ 0 & 0 & 1 \end{bmatrix} \tag{4.5}$$

For convenience, all quantities derived in the theory section will be done so in the rotating reference frame. All quantities will be converted to the inertial reference frame in the results section.

4.1.3 Wing Design

A wing is now fixed within the rotating coordinate frame (Fig. 4.3). For simplicity we model an idealized wing as a thin, planar semi-ellipse identical to the geometry presented by Berman and Wang [57]. Its chord width $c(r)$ can be expressed via an analytic function

$$c(r) = \frac{4\bar{c}}{\pi}\sqrt{1 - \frac{r^2}{R^2}} \tag{4.6}$$

where $\bar{c}$ is the mean chord width defined by $\bar{c} = \frac{\pi}{2b}$, b is the semi-minor axis of the ellipse and R is the total length of the wing (the semi-major axis of the ellipse). Variable r represents a reference line coincident with the y axis about which the wing velocity/acceleration is calculated during aerodynamic modeling. The upper edge of the wing is defined as the leading edge $x_{le}(r)$ and the lower edge of the wing is defined as the trailing edge $x_{te}(r)$. The wing is offset by a distance x_s along the x axis, defined as the distance between the y axis of rotation and the major axis of the elliptical wing.

4.1.4 Angular Momentum and Moments

Derivation of the angular momentum and moments for a rigid body rotating about a fixed point in three-dimensions is well understood. Within the rotating reference frame, the angular momentum $(\vec{H}_0)_{xyz}$ for a single wing is expressed as

$$(\vec{H}_0)_{xyz} = \mathbf{I}_0\vec{\Omega} \tag{4.7}$$

where $\mathbf{I}_0$ is the inertial tensor, which is constant with respect to the wing-fixed coordinate system. Assuming the wing is a flat, planar structure with negligible thickness, the inertial tensor $\mathbf{I}_0$ can be expressed as

$$\mathbf{I}_0 = \begin{bmatrix} I_{xx} & -I_{xy} & 0 \\ -I_{xy} & I_{yy} & 0 \\ 0 & 0 & I_{zz} \end{bmatrix} \tag{4.8}$$

where I_{xx}, I_{yy} and I_{zz} are the moments of inertia about the x, y and z axes respectively and I_{xy} is the product of inertia relative to the $x - y$ plane. The moments $(\vec{M}_0)_{xyz}$ are then determined by differentiating the angular momentum with respect to time, resulting in

$$(\vec{M}_0)_{xyz} = \vec{\Omega} \times \mathbf{I}_0\vec{\Omega} + \mathbf{I}_0\dot{\vec{\Omega}} \tag{4.9}$$

The moments above arise from the inertial forces of the wing. For conciseness, these moments will be referred to as the inertial moments throughout the remainder of the paper to differentiate them from aerodynamic moments.

Lastly, angular momentum and moments are related by the angular impulse $\vec{J}$, defined by $\vec{J} = \int_{t_1}^{t_2} \vec{M} dt$. The angular impulse serves as a convenient quantity in comparing aerodynamic and inertial torques over a period of time. The angular momentum and moments are related via the impulse-momentum equation

$$\int_{t_1}^{t_2} (\vec{M}_{0,total})_{xyz}\, dt = \Delta(\vec{H}_0)_{xyz} \tag{4.10}$$

where $(\vec{M}_{0,total})_{xyz}$ is the difference of aerodynamic and inertial moments, $(\vec{M}_{0,total})_{xyz} = (\vec{M}_{0,aero})_{xyz} - (\vec{M}_{0,inertial})_{xyz}$. The angular impulse will be abbreviated to impulse throughout this chapter.

4.1.5 Aerodynamic Forces and Moments

Owing to complex unsteady flows [58], the aerodynamic forces and moments are somewhat more difficult to estimate than the inertial moments derived above. While computational fluid dynamics (CFD) has been used with some success to quantify aerodynamic forces and moments, the method is computationally expensive and not conducive to parametric studies [51]. Thus we rely on a simpler, albeit approximate, Blade Element Momentum Theory (BEMT) that has been used with some success in earlier studies [59, 60, 57]. The method functions by discretizing a wing into infinitesimal airfoils. Local aerodynamic forces and moments acting on each foil are determined and then integrated to determine the net aerodynamic force and moment acting over the entire wing. While BEMT assumptions typically ignore critical aerodynamic phenomena such as leading edge vortices, spanwise flows and wing-wake interactions, the method provides reasonable order-of-magnitude estimates of aerodynamic forces and moments. It should be noted that several BEMT models are readily available – for this reason, the theoretical derivation presented here is rather brief [61, 53, 62].

For a more detailed explanation of individual terms, the reader is encouraged to refer to [54].

The general formulation for BEMT states

$$dF = Cq\,dS \tag{4.11}$$

where dF is a differential force acting on the discrete airfoil, C is an non-dimensional empirically measured aerodynamic coefficient, q is the dynamic pressure acting on the airfoil, and dS is a differential reference area. The dynamic pressure is defined by

$$q = \frac{1}{2}\rho_f \vec{V} \cdot \vec{V} \tag{4.12}$$

where ρ_f is the fluid density and $\vec{V}$ is the instantaneous fluid velocity vector varying along a reference line. The differential reference area dS is defined by

$$dS = c(r)dr \tag{4.13}$$

Using these definitions in conjunction with Eq. 4.11 is a convenient basis for evaluating aerodynamic forces and moments. The reference axis r shown in Fig. 4.3 is used to estimate the instantaneous fluid velocity at each discrete airfoil. Note that because r is coincident with y, all fluid velocity components are acting in-plane to each airfoil. Then, the position of each point on the wing along the reference line can be described by $\vec{r} = r\hat{e}_y$. Differentiating the position yields the velocity of each point along the reference line as

$$\vec{V} = r(\vec{\Omega} \times \hat{e}_y) = \underbrace{-r\omega_z}_{v_x}\hat{e}_x + \underbrace{r\omega_x}_{v_z}\hat{e}_z \tag{4.14}$$

Differentiating the velocity with respect to time yields the acceleration of each point along the reference line

$$\vec{a} = r[\vec{\Omega} \times (\vec{\Omega} \times \hat{e}_y) + \dot{\vec{\Omega}} \times \hat{e}_y] = \underbrace{r(\omega_x\omega_y - \dot{\omega}_z)}_{a_x}\hat{e}_x - \underbrace{r(\omega_x^2 + \omega_z^2)}_{a_y}\hat{e}_y + \underbrace{r(\omega_y\omega_z + \dot{\omega}_x)}_{a_z}\hat{e}_z \tag{4.15}$$

As most aerodynamic forces are dependent only on velocity, the acceleration described above is only necessary when considering added mass. Lastly, the angle of attack, denoted by AoA, is defined as the angle between the instantaneous fluid velocity and the positive x axis (Fig. 4.4). This parameter is crucial, as most empirically measured coefficients such as lift and drag coefficients vary significantly with the angle of attack. Mathematically, this takes the form

$$AoA = \tan^{-1}\left(-\frac{\omega_x}{\omega_z}\right) \tag{4.16}$$

It should be noted that when solving computationally via Matlab, the atan2 function is used in lieu of the atan function.

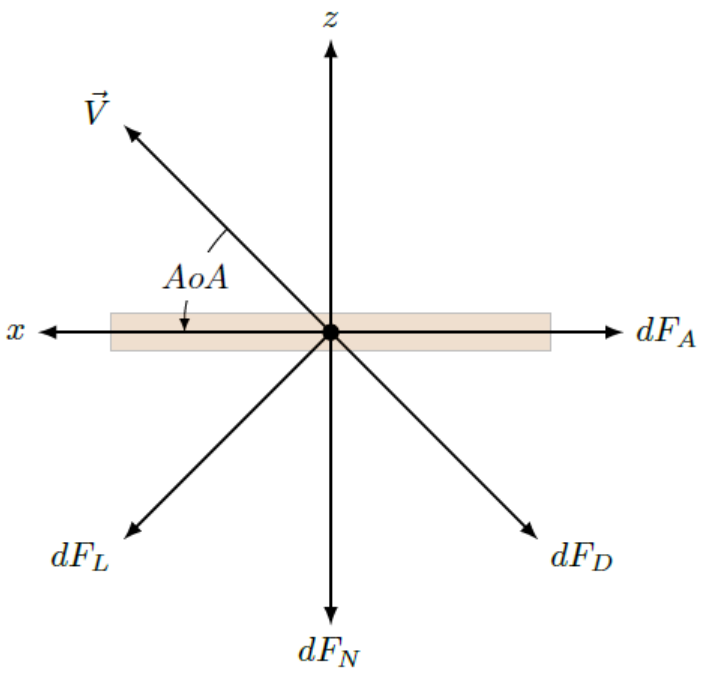

Figure 4.4: Aerodynamic forces acting on discrete airfoil

Lift, Drag, Normal and Axial Forces

First, lift, drag and their respective projections onto the normal and axial axes of a discrete airfoil are considered (Fig. 4.4). Note that the drag force acts in the opposite direction of the instantaneous wing velocity, as the induced fluid velocity is in the opposite direction of the wing velocity along the reference line defined in Fig. 4.3. The differential lift and drag can be modeled as

$$dF_{[\cdot]} = \frac{1}{2}\rho_f C_{[\cdot]}(\vec{V}\cdot\vec{V})c(r)dr = \frac{1}{2}\rho_f C_{[\cdot]}(\omega_x^2+\omega_z^2)r^2c(r)dr \tag{4.17}$$

where $[\cdot]$ is a place-holder for lift or drag. The the lift and drag coefficients are

$$C_L(AoA) = C_{L,max}\sin(2AoA) \tag{4.18}$$

$$C_D(AoA) = \left(\frac{C_{D,max}+C_{D,0}}{2}\right) - \left(\frac{C_{D,max}-C_{D,0}}{2}\right)\cos(2AoA) \tag{4.19}$$

where $C_{L,max}, C_{D,max}$ and $C_{D,0}$ are empirically measured coefficients specific to the wing used. The differential normal and axial forces may be determined by rotating the differential lift and axial forces by a positive rotation of AoA about the y axis. This results in

$$d\vec{F}_A = (dF_D\cos AoA - dF_L\sin AoA)[-\hat{e}_x] \tag{4.20}$$

$$d\vec{F}_N = (dF_D\sin AoA + dF_L\cos AoA)[-\hat{e}_z] \tag{4.21}$$

$d\vec{F}_A$ and $d\vec{F}_N$ can be integrated over the reference line r to yield the total normal and axial forces acting over the entire wing, but it is convenient to leave them in differential form for later evaluation of yaw and roll aerodynamic moments.

Pitching Axis Aerodynamic Moments

The pitching axis (y-axis) differential aerodynamic moments are modeled as

$$d\vec{M}_y = \frac{1}{2}\rho_f C_m(\omega_x^2+\omega_z^2)c(r)x_{CP}(r)r^2dr\,\hat{e}_y \tag{4.22}$$

where C_m is the dimensionless aerodynamic moment coefficient and X_{CP} is the distance from reference line r to the aerodynamic center of pressure. Specifically,

$$C_m(AoA) = C_L \cos AoA + C_D \sin AoA \tag{4.23}$$

$$X_{CP} = X_{LE}(r) + c(r)\hat{d}_{cp} \tag{4.24}$$

where $\hat{d}_{cp}$ is the dimensionless center of pressure as a function of AoA, approximated from [63] as

$$\hat{d}_{cp} = \frac{1}{4}|AoA| \tag{4.25}$$

Aerodynamic Damping Moments

The aerodynamic damping moment acts opposite ω_y and affects the net aerodynamic moment about the pitching axis. The spatial variation of aerodynamic damping $\delta(d\vec{M}_{rd})$ acting on a discrete airfoil is modeled as

$$\delta(d\vec{M}_{rd}) = \frac{1}{2}\rho_f C_{rd}\omega_y|\omega_y| \int_{x_{te}}^{x_{le}} |x|x^2 dx\, \hat{e}_y \tag{4.26}$$

where C_{rd} is the coefficient of rotational damping. The absolute value sign acting on ω_y ensures that the damping force always acts opposite to the rotational velocity about the pitching axis. Integrating spatially from the the wing trailing edge to the leading edge results in the differential aerodynamic damping acting on an airfoil

$$d\vec{M}_{rd} = \frac{1}{8}\rho_f C_{rd}\omega_y|\omega_y|(|x_{le}|x_{le}^3 - |x_{te}|x_{te}^3)\, \hat{e}_y \tag{4.27}$$

Added Mass

As the wing flaps, it accelerates some volume of fluid surrounding it, causing an added mass effect. Added mass affects roll/pitch aerodynamic moments and the aerodynamic force in the z direction. The differential added mass is modeled as

$$d\vec{F}_{z,am} = -[a_z r\lambda_z(r) + \dot{\omega}_y\lambda_{zw}(r)]dr\,\hat{e}_z \tag{4.28}$$

$$d\vec{M}_{y,am} = -[a_z r\lambda_{zw}(r) + \dot{\omega}_y\lambda_w(r)]dr\,\hat{e}_y \tag{4.29}$$

where the coefficients above are described by

$$\lambda_z = \pi\rho_f\left[\frac{c(r)}{2}\right]^2 \tag{4.30}$$

$$\lambda_{zw} = -\pi\rho_f\left[\frac{c(r)}{2}\right]^2 x_s \tag{4.31}$$

$$\lambda_w = -\pi\rho_f\left[\frac{c(r)}{2}\right]^2 x_s^2 + \frac{1}{8}\pi\rho_f\left[\frac{c(r)}{2}\right]^4 \tag{4.32}$$

Roll/Yaw Axis Aerodynamic Moments

Lastly, the aerodynamic moments acting about the roll and yaw axis are calculated. These moments are a result of the total forces acting in the x and z directions on the wing surface. Mathematically, this takes the form

$$\vec{M}_{aero} = \int_0^R \vec{r}\times d\vec{F}\,dr \tag{4.33}$$

where the total forces acting on a discrete airfoil are

$$d\vec{F} = d\vec{F}_A + d\vec{F}_N + d\vec{F}_{z,am} \tag{4.34}$$

4.1.6 Linearization

In general, the stroke deviation amplitude is much smaller than the amplitude of pitch and roll rotations in flying insects [3]. As a result, it is possible to linearize all terms described above about an operating point $(\gamma, \dot{\gamma}, \ddot{\gamma}) = (0, 0, 0)$, effectively reducing the stroke deviation to an infinitesimal rotation. Linearization allows us to carry out order analysis of each term, assuming finite rotations pitch and roll are of $\mathcal{O}(0)$ and the infinitesimal stroke deviation is

of $\mathcal{O}(1)$. We hypothesize the zeroeth order terms arise from primary flight muscles whereas first order terms are a result of the finer steering muscles modulating stroke deviation. This hypothesis is appealing, as steering muscles constitute only a fraction of the total muscle mass, which implies they are capable of producing lesser resultant moments than the larger power muscles [3].

The linearization of each term can be conducted by using a Taylor series expansion centered at the operating point $(\gamma, \dot{\gamma}, \ddot{\gamma}) = (0, 0, 0)$. As the expansion of each term can be somewhat arduous, the linearized form of each term is not presented in this chapter. A complete version of linearization methods is found in Appendix D. Instead, the linearized lift will serve as an example for the linearization of the other terms. The lift linearized about the operation point is equal to

$$F_L \approx \frac{1}{2}\rho_f \int_0^R r^2 c(r) dr$$
$$* \left[\underbrace{C_L V^2}_{\mathcal{O}(0)} + \underbrace{\sum_{i=1}^{2} \left(2C_L \left(v_x \frac{\partial v_x}{\partial \gamma^{(i)}} + v_z \frac{\partial v_z}{\partial \gamma^{(i)}} \right) + \frac{\partial C_L}{\partial AoA} \left(\frac{\partial v_z}{\partial \gamma^{(i)}} v_x - \frac{\partial v_x}{\partial \gamma^{(i)}} v_z \right) \right) \gamma^{(i)}}_{\mathcal{O}(1)} \right]_{\gamma, \dot{\gamma}=0} + \mathcal{O}(2) \tag{4.35}$$

where $\gamma^{(1)} = \gamma$ and $\gamma^{(2)} = \dot{\gamma}$. Note that lift is not a function of $\ddot{\gamma}$, and therefore need not be linearized about $\ddot{\gamma} = 0$. The inertial moments and added mass terms, on the other hand, will require further linearization about $\ddot{\gamma} = 0$. It should also be stressed that the rotation matrix $\mathbf{R}$ will have to be linearized as well when representing quantities in the inertial frame.

4.2 Results

Simulation parameters are introduced. We explore the effect stroke deviation angle has on net force and moment production. Averaged wing angular momentum is then calculated as a function of stroke deviation phase. A timed shift in deviation phase is presented and

aerodynamic impulses are compared with inertial impulses during this transient period.

It is emphasized that all simulation results presented are for a single representative insect wing with a relatively rigid set of kinematics. Therefore, while the results presented provide insight into the functional role of the stroke deviation, they should be extended to other insects/FWMAVs with caution. It is necessary to consider varying wing geometries and kinematics coupled with experimental validation to consider these results universal.

4.2.1 Simulation Parameters

All simulation parameters in this section are summarized in Table 5.1. These wing parameters are identical to those presented by Berman et al. [57] and are similar to those found by Hedrick et al [60] for the Hawkmoth *Manduca sexta*. The wing is offset along the positive x axis by $x_s = b$, which represents the scenario where the wing is recessed behind the y axis of rotation and the leading edge is coincident with the y axis at $r = 0$. The wing is discretized into 1000 evenly spaced blade elements.

Next, aerodynamic coefficient and rotation profiles are specified. Aerodynamic coefficients are taken from Whitney et al. [54]. Rotations are assumed harmonic functions of the form $n = n_0 \sin(\omega t + \phi_n)$, where n is a place holder for α, β, γ, the flap frequency of the wing is ω and ϕ_n represents a phase shift. Values for the rotation parameters are approximated from values published by Wilmott and Ellington [3].

All numerical results shown are solved via Matlab. All forces, moments and momentum terms are solved over a single wing beat period T using 1000 evenly spaced time steps unless otherwise specified. All integration (both spatial and temporal) is conducted numerically using trapezoidal integration. Spatial integration is conducted outside any timing loop to reserve computational power to facilitate large parameter sweeps.

4.2.2 Aerodynamic Forces

We first investigate the aerodynamic forces generated by the flapping wing. Note the relationship between the right wing inertial frame XYZ and the insect body frame $X_B Y_B Z_B$

Table 4.1: Summary of Simulation Parameters

Variable	**Description**	**Value**	**Unit**
R	Wing Span	51.9	mm
b	Maximum Chord Width	11.62	mm
x_s	Shift along x axis	11.62	mm
$\bar{c}$	Mean Chord Width	18.26	mm
A	Surface Area	947.7	mm^2
m_w	Wing Mass	47	mg
m	Insect Body Mass	1.648	g
ρ_f	Fluid Density	1.29	kg/m^3
$C_{L,max}$	Max Lift Coefficient	1.8	-
$C_{D,max}$	Max Drag Coefficient	3.4	-
$C_{D,0}$	Min Drag Coefficient	0.4	-
C_{rd}	Rotational Damping Coefficient	5	-
α_0	Roll Amplitude	60	degrees
β_0	Pitch Amplitude	45	degrees
γ_0	Stroke Deviation Amplitude	10	degrees
ϕ_α	Roll Phase	0	rad
ϕ_β	Pitch Phase	$\pi/2$	rad
ϕ_γ	Stroke Deviation Phase	Variable	rad
f	Flap Frequency	25	Hz
I_{xx}	MOI about x	31.65	g-mm^2
I_{yy}	MOI about y	7.88	g-mm^2
I_{zz}	MOI about z	39.46	g-mm^2
I_{xy}	$x-y$ Product of Inertia	11.98	g-mm^2

(Fig. 4.1). Hovering implies the upward average net vertical force is equal in magnitude to the downward average net vertical force from aerodynamic, inertial and gravity forces. Initially, the stroke deviation γ is set to zero, and the phase of pitch ϕ_β is varied from 0 to 2π. In the absence of stroke deviation, only terms of $\mathcal{O}(0)$ are present. The vertical force

from the single wing is averaged over a single wing beat period to determine the mean vertical force and doubled to account for the left wing which is assumed to flap symmetrically. Inertial reaction forces are not considered, as they tend to average to zero over the entire parameter space. Given the fixed rotation amplitudes (Tab. 5.1), maximum mean vertical force was achieved at a pitch phase in the neighborhood of $\phi_\beta = \pi/2$ – mean vertical force was 25% greater in magnitude than the total insect weight. This phase relationship between pitch and roll is consistent with that presented by Berman and Wang [57] and is maintained for the remainder of the paper.

Next, stroke deviation is included at amplitude $\gamma_0 = 10°$ and ϕ_γ is varied from 0 to 2π to determine its effect on aerodynamic force production. Figure 4.5 shows the total aerodynamic forces over a wingbeat period when $\phi_\gamma = \pi/2$. From the figure, it is apparent the average vertical force stems almost entirely from zeroeth order terms, while first order terms associated with stroke deviation average to nearly zero. Across the entire range ϕ_γ, forces associated with stroke deviation were found to constitute maximally 0.2% of total averaged vertical force. Additionally, stroke deviation did not significantly affect lateral averaged forces in the body X_B or Y_B directions.

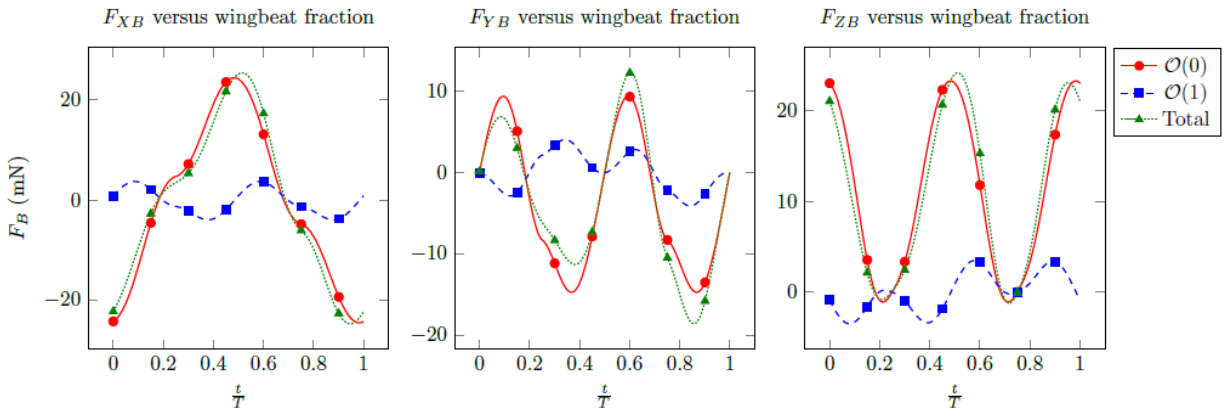

Figure 4.5: Body forces from single wing versus wingbeat fraction. Zeroeth order, first order and total aerodynamic forces when $\phi_\gamma = \pi/2$.

This result provides compelling insight into the role of power muscles and steering muscles in flying insects. We hypothesize power muscles dominate aerodynamic force production, which implies steering muscles associated with stroke deviation must serve some other functional role. To expound the role of the stroke deviation further, we address aerodynamic and inertial moments.

4.2.3 Averaged Moments

In order for a moment to reorient the insect body over the course of several wingbeats, the average value of the moment over that time span must be nonzero. In this section we identify how inertial and aerodynamic moments are affected by the stroke deviation angle.

First, we address symmetry between the left and right wings. Pitch and roll are assumed identical for both wings. Therefore, only the stroke deviation angle is capable of introducing left-right asymmetry. Consequently, the magnitude of the zeroeth order moments about all axes are identical between left and right wings. Moments due to zeroeth order terms about

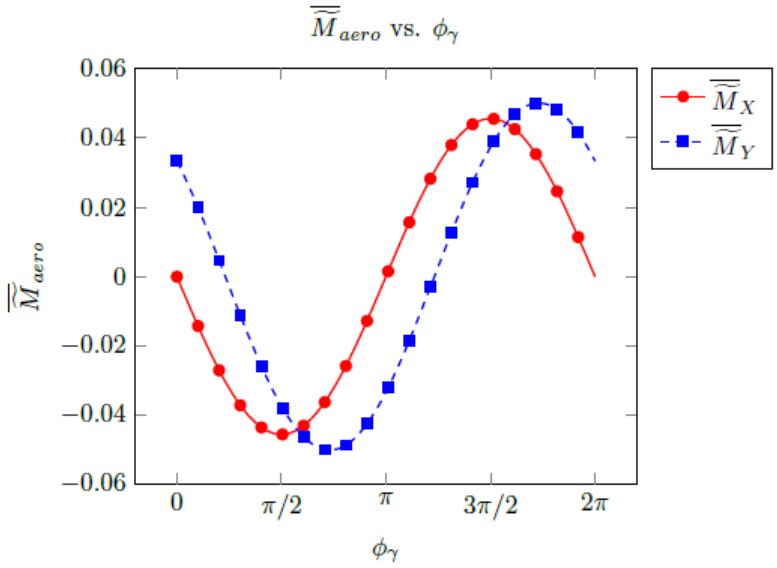

Figure 4.6: First order non-dimensional averaged aerodynamic moments as a function of ϕ_γ

X_L, X_R and Z_L, Z_R are equal and opposite, whereas moments about Y_L, Y_R are additive. Leveraging these symmetry arguments, we can investigate the total moments acting at fixed point O.

Stroke deviation amplitude is fixed to $\gamma_0 = 10^\circ$ and ϕ_γ is varied between 0 and 2π. Aerodynamic and inertial moments are calculated over a single wing beat period and subsequently averaged. Averaged values will be indicated by an overbar. All reported moment values are further non-dimensionalized, first by allowing $\tau = \omega t$ and then by dividing by lead coefficient I_{zz}. Non-dimensionalized values will be denoted by a tilde overscore. Presented moments are with respect to the XYZ right wing inertial frame rather than the body inertial frame.

The simulation shows that inertial moments, both zeroeth and first order, average to zero over a wing beat period. This implies that at steady-state, wing inertial moments do little to reorient the body. Zeroeth order aerodynamic moments about the X and Y axis average to zero. The zeroeth order aerodynamic moment about the Z axis is canceled due to symmetry. Conversely, first order average aerodynamic moments about X and Y vary significantly with ϕ_γ (Fig. 4.6), while first order aerodynamic moments about Z average to zero over the entire range of ϕ_γ.

The averaged first order moments show that stroke deviation angle can have a marked effect on steering the insect body, a claim that is well supported by biological evidence. For instance, researchers have correlated bilateral actuation of the 3AXM muscle (which modulates stroke deviation) to longitudinal pitch control in Hawkmoths [1, 48]. Changes in the body pitch were associated with the firing latency of the 3AXM muscle. While the the muscle firing latency is not fully indicative of stroke deviation phase, there likely exists a correlation between the two. Furthermore, unilateral actuation of the 3AXM muscle causes banked turns in flying beetles [2], and during steady-state rolling maneuvers the blowfly exhibits large phase differences between the strain in some of the left-right steering muscles [64].

Specific to our results, bilateral shifts in stroke deviation phase alter the net mean pitch moment while leaving the net mean roll moment unaffected due to left-right symmetry. The presence of a mean pitching moment implies the center of gravity of the insect must be

recessed from the wing axis of rotation – if the center of gravity is coincident with the Y wing axis of rotation, a mean pitch moment would cause the insect to topple end over end. Measurements by Cheng et al. [65] indicate the center of gravity of the Hawkmoth is recessed from the wing axis of rotation by approximately 25% of the total wingspan. It is plausible the mean body pitch angle is prescribed by the equilibrium of the pitching moment due to gravity and the aerodynamic pitching moment caused by the stroke deviation angle. This proves a simple mechanism for controlling body pitch angle via changes in the magnitude and phase of the stroke deviation.

Moreover, the results indicate unilateral phase shifts of the stroke deviation angle can induce banked turns. Should ϕ_γ of the right wing change independently from that of the left wing or visa versa, the result will be a net aerodynamic moment about both wing pitch and roll axes. It is possible to achieve a significant roll moment without a pitching moment, suggesting these two axes can be controlled independently. This can be achieved by increasing ϕ_γ of the right wing while subsequently decreasing ϕ_γ of the left wing. The magnitude of the induced moment will then rely on the initial operating phase of the stroke deviation angle. Depending on the magnitude and symmetry of the left-right stroke deviation phase shift, the mean pitching moment may also be maintained during roll maneuvers such that the equilibrium body pitch angle is unaffected.

4.2.4 Transient Effects

According to our simulation, phase changes in the stroke deviation angle have a substantial impact on the steady-state aerodynamic moments acting on the body. However, there must exist a transient period in which the stroke deviation phase transitions from an initial phase to some final phase. While inertial moments average to zero at steady-state, it is possible they have a larger influence during this transient period. To investigate this, averaged angular momentum of the right wing is calculated as ϕ_γ is varied from 0 to 2π for a fixed amplitude $\gamma_0 = 10^\circ$ (Fig. 4.7). Clearly, averaged wing angular momentum is sensitive to ϕ_γ. This signifies that during a phase shift from an initial phase ϕ_0 to a final phase ϕ_f, an

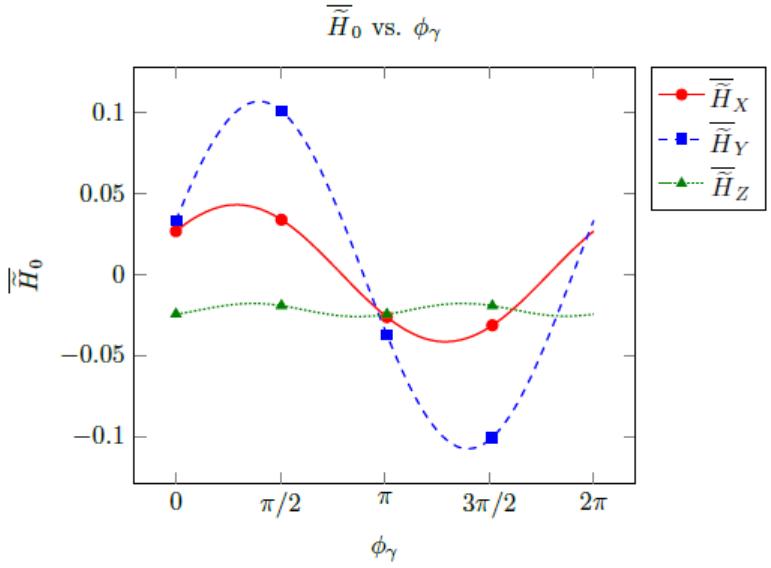

Figure 4.7: Non-dimensional averaged angular momentum as a function of ϕ_γ

impulse must have acted to cause the change of angular momentum. These results motivate a comparison between aerodynamic and inertial impulses during a phase-shifting transient period.

To compare aerodynamic/inertial impulses, a transient function $\phi_\gamma(t)$ is defined with the conditions $\phi_\gamma(0) = \phi_0$ and $\phi_\gamma(NT) = \phi_f$, where N is the number of wing beats during the transient period. As a result, the stroke deviation angle takes the form $\gamma = \gamma_0 \sin[\omega t + \phi_\gamma(t)]$. There are infinitely many transient functions that satisfy initial/final phase conditions, and each unique function may alter the resulting impulses. As an example, linear and fifth-order polynomials are introduced as candidates for $\phi_\gamma(t)$. The fifth-order transient function has the added benefit of being continuous at the $t = 0$ and $t = NT$ in both $\dot{\gamma}$ and $\ddot{\gamma}$, whereas the linear transient function causes discontinuous leaps in stroke deviation velocity and acceleration. Both transient functions and their influence on $\gamma, \dot{\gamma}, \ddot{\gamma}$ are shown in Fig. 4.8 over a single wingbeat.

Due to the continuity in derivatives of γ, the fifth-order polynomial is used moving

forward. An initial phase angle $\phi_0 = 0$ is assumed, and the final phase angle ϕ_f is varied between 0 and 2π in 100 evenly spaced spaced increments. Cases where $N = 1$ and $N = 5$ wingbeats are considered to illustrate how transient duration affects the magnitude of impulses. Impulses are calculated by numerically integrating the moments with respect to time. For the case where $N = 5$, 5000 evenly time steps are used. Zero order impulses are not considered – it is determined that they either integrate to zero or are canceled by wing symmetry. Presented results are again normalized with respect to time and by lead coefficient I_{zz}. The results are shown in Fig. 4.9. We emphasize the curves represented here will vary with the starting phase ϕ_0.

Simulations suggest an important result – inertial torques may play a critical role in

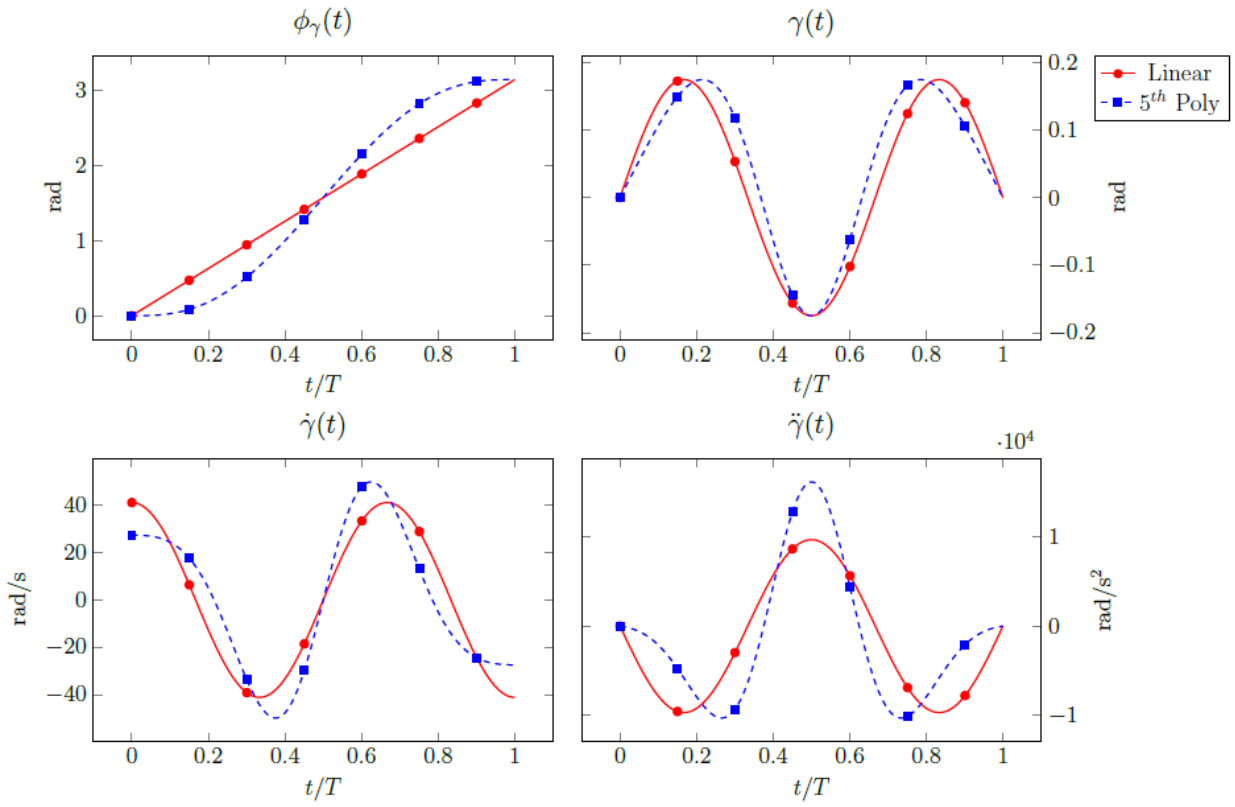

Figure 4.8: Example transient functions $\phi_\gamma(t)$ and their influence on stroke deviation

steering. This deviates from the notion that aerodynamic moments dominate body attitude changes in insects. Fig. 4.9 shows that for short transient periods, the magnitude of inertial impulses is comparable to that of aerodynamic impulses. In some cases, the two impulses act antagonistically thereby decreasing the net impulse acting on the insect body. Consider

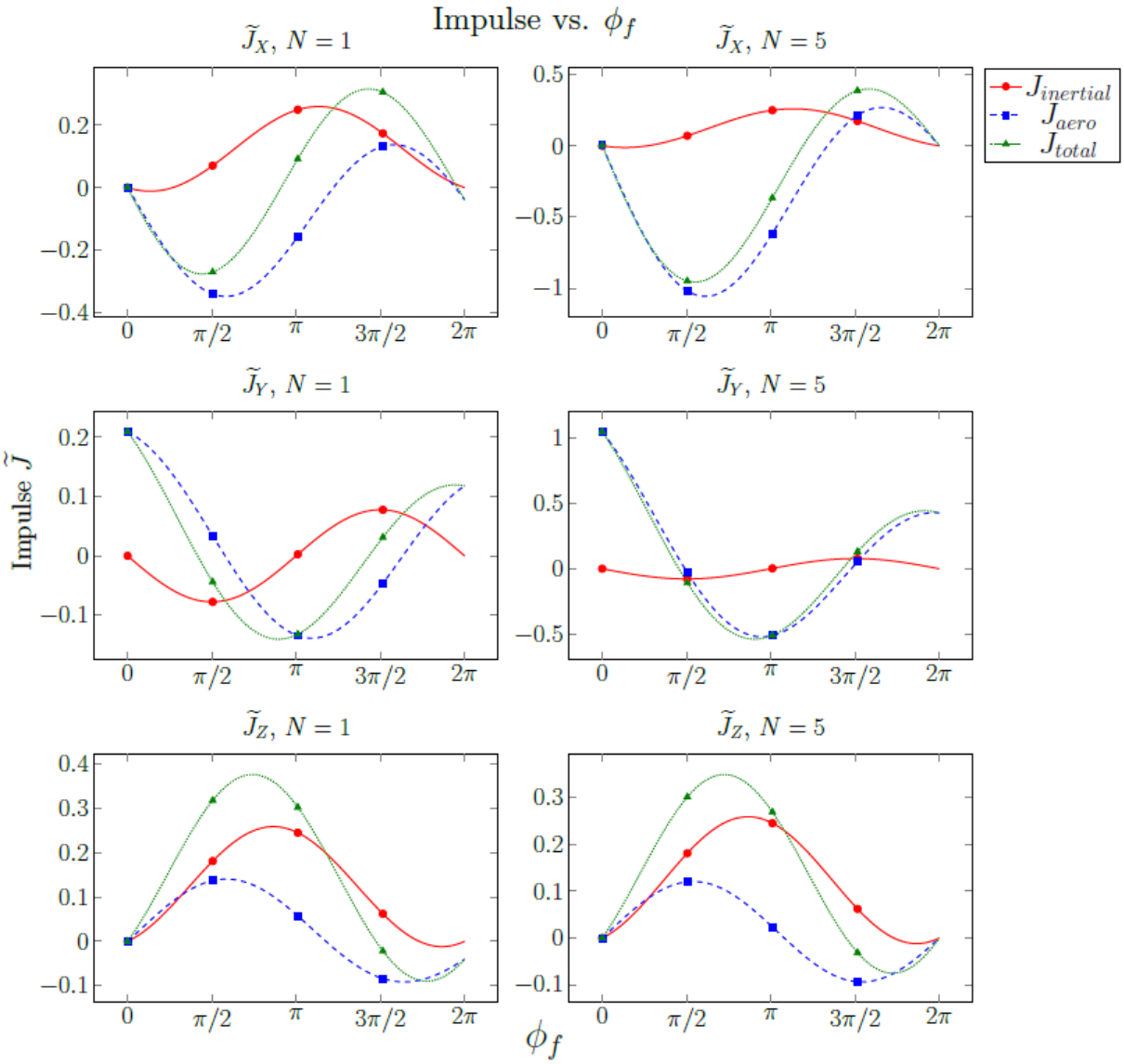

Figure 4.9: Aerodynamic, inertial and total impulses during transient phase shift from $\phi_0 = 0$ to variable ϕ_f over one and five wingbeats.

the phase shift from $\phi_\gamma = 0$ to $\phi_\gamma = \pi/2$ over a single wingbeat. $J_{Y,aero}$ and $J_{Y,inertial}$ act in opposite directions and have a reducing effect on the total impulse. As a result, the body will have a tendency to pitch about the negative Y axis, which is coincident with Y_B. This might prove to be a novel mechanism to slow the insect body to a halt after an abrupt rotation. It is possible that an insect beginning from rest (zero angular momentum) gains angular momentum during the transient period and then returns to a resting state once the the net impulse has integrated to zero. During other transient phase shifts, aerodynamic and inertial impulses tend to act synergistic.

Moreover, the simulation shows transient timing influences the relative contribution of aerodynamic and inertial torques. The magnitude of aerodynamic impulses increases significantly as transient becomes longer whereas inertial impulses are unaffected. This is likely due to the presence of averaged steady-state aerodynamic moments at different values of ϕ_γ (Fig. 4.6). This explains why the aerodynamic impulse about Z is insensitive to the transient length – the steady-state aerodynamic moment about Z averages to zero for all stroke deviation phase angles.

4.2.5 Scaling Effects

For the Hawkmoth *Manduca sexta*, inertial impulses were found comparable in magnitude to aerodynamic impulses during a transient stroke deviation phase shifts. Nonetheless, it is possible the contribution of aerodynamic and inertial impulses varies with the scale of the insect. To assess the scaling effect on aerodynamic/inertial impulses, wings of three different insects are considered – the Hawkmoth, bumblebee and fruitfly. Wing properties are acquired from Berman and Wang [57] and are shown in Table 4.2. Note the moments of inertia vary slightly from the published values in [57] due to the wing offset x_s.

While aerodynamic coefficients and rotation amplitudes vary modestly for each insect considered, it is convenient to assume uniformity for a more consistent comparison of aerodynamic and inertial impulses. Therefore, the rotation amplitudes and aerodynamic coef-

Table 4.2: Wing parameters for Hawkmoth, bumblebee and fruitfly

Parameter	**Hawkmoth**	**Bumblebee**	**Fruitfly**	**Unit**
R	51.9	13.2	2.02	mm
$\bar{c}$	18.26	4.02	0.67	mm
b	11.62	2.54	0.4265	mm
m_w	47	0.46	8.6×10^{-4}	mg
f	25	116	254	Hz
I_{xx}	31.65	0.0201	8.60×10^{-7}	g-mm^2
I_{yy}	7.88	0.0022	1.82×10^{-7}	g-mm^2
I_{zz}	39.64	0.0222	1.04×10^{-7}	g-mm^2
I_{xy}	11.98	0.0048	2.99×10^{-7}	g-mm^2

ficients shown in Tab. 5.1 are used for all three insects. The initial stroke deviation phase is fixed to $\phi_0 = 0$ and the final stroke deviation phase ϕ_f is varied from 0 to 2π in 100 evenly spaced intervals. Owing to the increased flap frequency seen in the bumblebee and fruitfly, 5000 evenly spaced time steps are used for these cases. 1000 evenly spaced time steps are maintained for the Hawkmoth. The aerodynamic and inertial impulses are calculated for each phase transition, where the phase transition occurs over a single wing beat ($N = 1$). Then, the maximum of the absolute value of the each impulse is calculated, and $max|\vec{J}_{inertial}|/max|\vec{J}_{aero}|$ is determined as a function of wing length R. As the maximum values for aerodynamic/inertial impulses likely do not correspond to the same ϕ_f, the RMS values of aerodynamic/inertial impulses over the entire range of ϕ_γ are calculated as well. $rms(\vec{J}_{inertial})/rms(\vec{J}_{aero})$ is also plotted as a function of wing length R. The results are shown in Fig. 4.10.

This simulation shows that under the given assumptions, inertial effects are less pro-

nounced for smaller flying insects. While not enough data points are considered to identify a clear mathematical trend, it appears the relative contribution of inertial impulses scales non-linearly. Inertial impulses about Z shows the largest variation for the various insects whereas the variation of inertial impulses about Y is much less. In any case, inertial impulses constitute a large percentage of the total impulse.

4.2.6 Body Yaw Angular Velocity

Airborne insects can achieve considerable angular velocity during aerial maneuvers. For example, the Hawkmoth *Manduca Sexta* has been measured at angular rates as large as $800°/s$ about the body yaw axis [66]. Consequently, it is prudent to assess the achievable angular velocity about at least one axis of the insect body using the model developed in this research.

Body rotations will cause an additional component of velocity to the wing, an effect that is not accounted for in this model. However, the maximum angular velocity of the wing

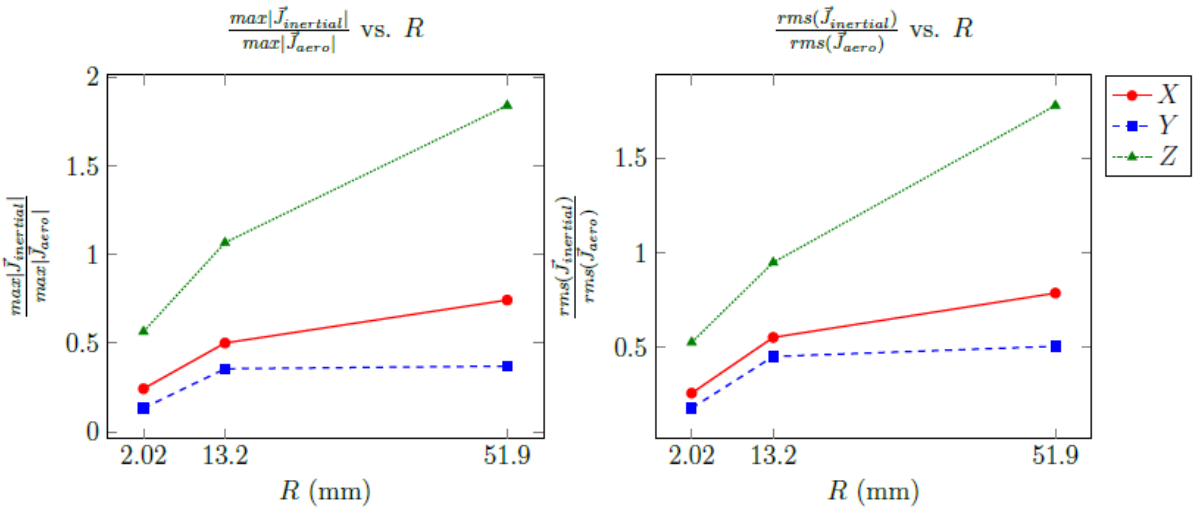

Figure 4.10: Comparison of aerodynamic and inertial impulses for insect wings of varying length scales.

(approximately 9500°/s about the roll axis) is significantly larger than the achievable angular velocity of the body. Therefore, body dynamics will only slightly affect net wing angular velocity and consequently, the net moment production. Thus, we choose to represent an idealized situation in which the body is permitted to rotate independently of the wings. We assume the only moments causing body rotation are the inertial and aerodynamic moments generated by the flapping wings. For this reason, angular velocity about Y_B is not considered. Body pitch angular velocity relies not only on gravity, but also on unmodeled abdominal flexion [67] which may affect net pitching moments. Furthermore, no reliable data was found regarding angular velocity or inertial properties about the body roll axis X_B for the Hawkmoth *Manduca Sexta*. Consequently, only angular velocity about the body yaw axis (Z_B) is considered.

To determine the body yaw angular velocity, we assume the insect body is coincident with the X_B axis. The body is then pinned such that it can rotate only about the Z_B axis. An initial stroke deviation phase ϕ_0 is selected and a timed phase shift to ϕ_f is introduced. The initial stroke deviation phase is set to $\phi_0 = \pi$ for two reasons. First, it represents a zero-crossing of the averaged aerodynamic moments about about X (Fig. 4.6), which is coincident with yaw body axis Z_B (Fig. 4.1). Operating at this zero-crossing is beneficial, as a phase advance/delay will correspond to a steady-state positive/negative averaged aerodynamic moment $\overline{\widetilde{M}}_X$. Second, $\phi_0 = \pi$ corresponds to a negative steady-state aerodynamic moment about Y (Fig. 4.6), representing the case where the averaged aerodynamic moment causes the insect body to be inclined and recessed from the wing leading edge.

With the initial stroke deviation phase ϕ_0 fixed, the final stroke deviation phase ϕ_f is varied from 0 to 2π in 100 evenly spaced increments. Transient durations of one and five wingbeats are considered. The impulse from the total moment during each phase transition is calculated, and the resulting body angular velocity $\omega_{Z,B}$ immediately following the transient is determined using the impulse-momentum relationship in Eq. 4.10. The insect body starts from rest (no angular momentum) and the insect moment of inertia about the yaw body axis $I_{ZZ,B}$ is taken from Hedrick et al. [66] for a value of $I_{ZZ,B} = 2.43\times10^{-7}$ kg-m^2. The achievable

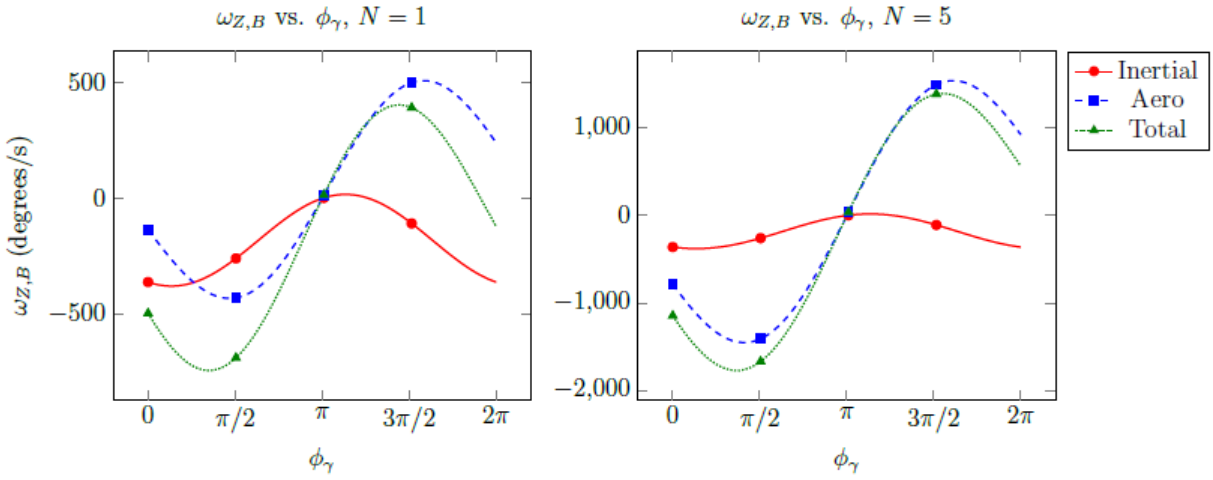

Figure 4.11: Aerodynamic and inertial contributions from single wing to $\omega_{Z,B}$ and total $\omega_{Z,B}$ immediately after transient phase shift from $\phi_0 = \pi$ to variable ϕ_f over one and five wingbeats.

body yaw angular velocities from a single wing are shown in Fig. 4.11. Contributions of inertial and aerodynamic impulses to $\omega_{Z,B}$ are shown separately.

According to the simulation results shown in Fig. 4.11, the insect can achieve the measured angular body yaw rate of $800°/s$ simply by adjusting the stroke deviation phase – a nontrivial amount of this angular velocity is generated by inertial torques. In the case where $N = 1$, this can be accomplished by advancing ϕ_γ of the right wing from π to approximately $5\pi/4$ while simultaneously reducing ϕ_γ of the left wing from π to $3\pi/4$. For the case where $N = 5$, a much smaller deviation from ϕ_0 can cause the same effect. Larger deviations induce body yaw angular velocities likely not realistic in insect flight. Similar to the inertial moments and impulses shown in Fig. 4.9, the contribution of aerodynamic moments to $\omega_{Z,B}$ increases with the duration of the phase shift whereas the contribution of inertial moments is unaltered.

4.3 Discussion

The entirety of the research presented shows that (1) modest changes in stroke deviation induce aerial maneuvers, and (2) inertial torques may play a much more profound role in steering and insect flight control than previously thought. Both of these key findings have important implications for FWMAV drive-train and control design.

First, FWMAV aerodynamic force production may be decoupled from control. Similar to biological mechanisms, lift/thrust production can be generated through a set of power actuators whereas steering can be relegated to smaller control actuators modulating stroke deviation. Finio et al. [68] suggested such stroke deviation actuators could be implemented on the Harvard Robobee. This design scheme allows power actuators to operate at an optimal frequency and magnitude and not deviate from this set-point to adjust vehicle attitude. This benefit is especially pronounced in the case of PZT actuators, where deviations in driving frequency or magnitude degrade actuator efficiency. Moreover, deviations in power actuator amplitude may adversely affect lift/thrust production. Separate control actuators may mitigate this problem. More specifically, active control over the stroke deviation angle allows FWMAVs to conscientiously adjust body pitch angle, a capability many designs do not possess. This is appealing to FWMAVs equipped with optical systems, as it allows vertical inspection objects without changing altitude. Additionally, stroke deviation actuation offers control authority over the wing roll axis, allowing vehicles to adjust course easily.

Perhaps more intriguingly, authority over the stroke deviation angle may facilitate inertial trajectory shaping. Our results show that abrupt changes in stroke deviation phase gives rise to inertial torques on the same order of magnitude as aerodynamic torques. While inertial attitude control has been implemented on larger vehicles [55], such mechanisms have yet to be realized on insect-scale aerial robotics. Such control may dramatically improve dexterity and agility of FWMAVs, with wing angular momentum serving as a quintessential design quantity. Of course, significant efforts must be made to assess the feasibility of inertial control on these micro systems. Stroke deviation actuators may require excessive

power to generate the quick phase changes necessary to generate large inertial imbalances. Large inertial torques may cause detrimental stresses on the vehicle airframe. Despite these practical matters, this research provides an exciting avenue for FWMAV designers moving forward.

Chapter 5

EFFECTS OF STRUCTURAL COMPLIANCE ON POWER CONSUMPTION

Scientists devote significant efforts towards understanding the effect of wing compliance on energy expenditure. Young et al. determined wing deformation benefited both power economy and aerodynamic performance in the desert locust *Schistocerca grega* [69]. This study utilized high-speed videography to capture both kinematics and deformation of the wing. Computational fluid dynamics (CFD) was used to evaluate aerodynamic forces, and the elastic deformation was prescribed based off videography results. Sun and Du conducted a similar study for hoverflies, concluding an elastic wing improved lift by about 10% and reduced aerodynamic power requirements by 5% compared with a rigid wing [70]. Medina et al. investigated structural compliance in a wing with similar deformation to that of the *Drosophila melanogaster*, finding compliance increased efficiency by as much as 19.5% [71]. For all these studies, however, calculating aerodynamic forces via CFD renders kinematic parametric studies computationally unfeasible. Alternatively, Lehmann et al. leveraged a reduced-order blade element aerodynamic model coupled with wing deformation measurements to determine the effect of elastic energy storage in the blowfly *Calliphora vicina*, finding span-wise bending indeed gives rise to appreciable potential energy storage [72]. Because this work treats the wing as an elastic beam, some of the physical phenomena associated with elastic planar wings rotating in three dimensions are lost. Moreover, in all studies mentioned, deformation was prescribed, thereby limiting insights into variable wing stiffness.

While there is evidence that structural deformation abates power expenditure in airborne insects, there remains a necessity to develop a reduced-order model fully characterizing the power expenditure of an elastic planar wing subject to three-dimensional rotation. The ob-

jective of the present work is to fulfill this need. The remainder of this chapter is organized as follows. First, we present an integrative model considering aerodynamic and inertial-elastic effects capable of estimating power requirements for flapping wings. The model is first applied to a simplified case of a *Manduca sexta* wing subject to one rotational degree of freedom in vacuum. This example elucidates the physical principals of elastic deformation on instantaneous power reduction. The model is subsequently applied to a more realistic scenario of a wing undergoing three-dimensional rotation in air. For this case, optimal wing kinematics and structural compliance for a hovering insect are determined. Lastly, some concluding remarks on how these results may benefit FWMAV performance are made.

5.1 Theory

Much of the theory necessary to characterize the power requirements of a flapping wing has been derived in chapters 2 and 4. We leverage the same planar elliptical presented in section 4.1.3, with the notable exception that the wing is no longer shifted along the x-axis ($x_s = 0$, Fig. 4.3). Under this configuration, the wing is symmetric about the y-axis, and product of inertia $I_{xy} = 0$. We employ the simple BEMT aerodynamic model derived in section 4.1.5. It is important recognize the underlying assumption to this aerodynamic model is a rigid wing; therefore, wing deformation will not affect aerodynamic force/moment production. For the structural model, we maintain the assumption that deformation arises from inertial-elastic forces rather than fluid loading.

The structural model is a modified form of Eq. 2.14. To be consistent with the aerodynamic model, we completely fix the rotating reference frame to the wing (Fig. 4.2), whereas previously the deformable structural model assumed stroke deviation occurred relative to the reference frame. With this adjustment, the structural model is determined as

$$\ddot{q_k} + \left[w_k^2 - (\omega_x^2 + \omega_y^2)\right] q_k = \dot{\vec{\Omega}} \cdot \vec{b_k} - \omega_z \, \vec{\Omega} \cdot \vec{a}_k \tag{5.1}$$

5.1.1 Instantaneous Power

With the aerodynamic moments and elastic deformation known and rigid-body motion prescribed, we derive the instantaneous power required for a flapping wing. The aerodynamic instantaneous power is simply calculated by

$$P_{aero}(t) = \vec{M}_{aero} \cdot \vec{\Omega} \tag{5.2}$$

While a similar approach may be taken to find the inertial instantaneous power, the inertial moments are presently unknown. The inertial moments for a rigid wing are easily determined, but including the moments due to elastic deformation adds undue complexity. Instead, we recognize that in the absence energy-dissipating structural damping, the net work done to the wing in a vacuum is simply the addition of kinetic and potential energy. Thus, differentiating the work with respect to time yields the inertial instantaneous power, or

$$P_{inertial}(t) = \frac{d}{dt}(T + V) \tag{5.3}$$

Kinetic and potential energy terms in Eqs. 2.6-2.7 can be decomposed into rigid and elastic components, as well as the inertial power. Finally, the total instantaneous power $P(t)$ required to flap the wing, including both inertial and aerodynamic loading, is described as the difference in aerodynamic and inertial power expressed by

$$P(t) = P_{aero}(t) - P_{inertial}(t) \tag{5.4}$$

In the above expression, it is assumed mechanical power is calculated from the moment of the wing acting on the body. Next, we present the root-mean-square (RMS) value of power. The RMS power is a crucial quantity for oscillatory systems, as the average power likely averages to zero. In terms of FWMAV design, a lower RMS power indicates extended battery life owing to reduced power expenditure. The RMS power for a continuous periodic signal is defined as

$$P_{RMS} = \sqrt{\frac{1}{T}\int_0^T [P(t)]^2\, dt} \tag{5.5}$$

Lastly, we define the compliance power ratio Λ to characterize the effect of wing compliance on RMS power. Λ is defined as the ratio of RMS power necessary for a rigid system to the RMS power necessary for a compliant system. We note that even for a compliant system, power is necessary for rigid body motion. The compliance power ratio is described by

$$\Lambda = \frac{P_{RMS,rigid}}{P_{RMS,total}} \tag{5.6}$$

Λ is a useful parameter in identifying whether wing compliance is advantageous or detrimental to power expenditure. If $\Lambda > 1$, the power necessary to drive an elastic system is less than that required to drive a rigid system. Conversely, if $\Lambda < 1$, more energy is required for the compliant system; in this case, elasticity adversely affects power consumption.

5.2 Example

In this section, we illustrate the utility of the derived model through two examples. First, we present relevant simulation parameters. We then consider the simple case of a wing subject to a single rotation in vacuum; this is intended to exemplify the effect of elastic deformation on inertial power. Next, we explore a more complex case of a wing rotating in three dimensions with aerodynamic forces present. The aim of this example is to optimize the wing kinematics and structural compliance to minimize power expenditure in a hovering insect.

5.2.1 Simulation Parameters

All simulation parameters used in the following examples are summarized in Table 5.1. We use a uniform thin planar wing idealized as an semi-ellipse with properties similar to the wing of the Hawkmoth *Manduca sexta*. Venation patterns are neglected. The wing span R, mean chordwidth $\bar{c}$, and wing mass m_w are identical to those presented by Berman and

Table 5.1: Summary of Simulation Parameters

Variable	**Description**	**Value**	**Unit**
R	Wing Span	51.9	mm
$\bar{c}$	Mean Chord Width	18.26	mm
A	Surface Area	947.7	mm^2
m_w	Wing Mass	47	mg
m	Insect Body Mass	1.648	g
ρ_f	Fluid Density	1.29	kg/m^3
$C_{L,max}$	Max Lift Coefficient	1.8	-
$C_{D,max}$	Max Drag Coefficient	3.4	-
$C_{D,0}$	Min Drag Coefficient	0.4	-
C_{rd}	Rotational Damping Coefficient	5	-
f	Flap Frequency	25	Hz
I_{xx}	MOI about x	31.38	g-mm^2
I_{yy}	MOI about y	1.57	g-mm^2
I_{zz}	MOI about z	32.95	g-mm^2
I_{xy}	$x-y$ Product of Inertia	0	g-mm^2
$\vec{a}_1$	Inertial Force Center of First Mode	-0.55 $\hat{e}_y$	-
ω_1	Natural Frequency of First Mode	Variable	Hz

Wang [57]. Empirically measured aerodynamic coefficients ($C_{L,max}, C_{D,max}, C_{D,0}, C_{rd}$) are taken from Whitney and Wood [54]. The Hawkmoth wingbeat frequency f, measured in Hertz, is estimated from Willmott and Ellington [3], and converted to rad/sec via $\omega = 2\pi f$. Moments and products of inertia are calculated analytically.

Next, the model wing is constructed in Abaqus FEA to determine the mode shapes and

inertial force center vectors. We limit our simulation to a single mode shape ϕ and modal response q; because we are consider only one vibration mode, the k subscript will be dropped for the remainder of the chapter. Inclusion of higher-order modes was found to have negligible effects on the examples presented, though these modes may have more pronounced effects if different simulation parameters are used. We match the mass characteristics of the wing by setting the wing density to $\rho = 1.2$ g/cm^3 and the thickness to $t = 41\,\mu$m. These values fall closely within the range of those published by Combes and Daniel [47]. Poisson's ratio is set to $\nu = 0$, as the actual value is unknown. Inclusion of a nonzero Poisson's ratio was determined to have a negligible effect. Lastly, the Young's Modulus E is left arbitrary. In all simulations we are critically interested in varying the wing compliance, which is accomplished by varying the natural frequency ω_1; the Young's Modulus may be back-calculated once a natural frequency is selected. Wing vibration modes are determined through Abaqus FEA. Calculated mode shapes are normalized with respect to the mass matrix. The first vibration mode is a bending mode, consistent with experimental modal testing conducted on *Manduca sexta* wings [73]. Vectors $\vec{a}_1$ and $\vec{b}_1$ for the first vibration mode are determined numerically using Matlab.

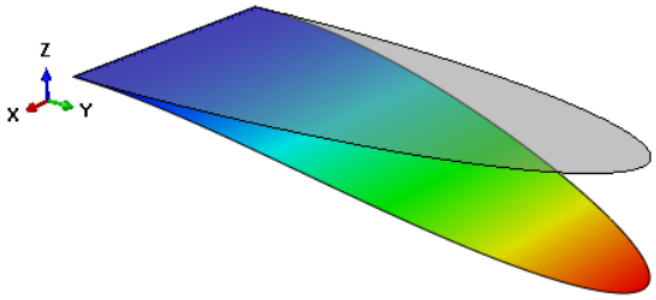

Figure 5.1: First vibration mode (bending) of the model wing superimposed on undeformed geometry.

5.2.2 Example One: Wing Subject to Roll in Vacuum

We first explore the effect of wing deformation on inertial power expenditure assuming the wing is subject to only roll ($\alpha \neq 0, \beta = \gamma = 0$) without aerodynamic loading. We assume roll undergoes simple harmonic harmonic motion, or $\alpha = \alpha_0 \sin \omega t$, where α_0 is the rotation amplitude. Given the limitations of our analytic solution methods described hereafter, we confine roll to a small-amplitude rotation of $\alpha_0 = 10°$. We normalize Eq. 2.14 with respect to time by allowing $\tau = \omega t$. Under these conditions, Eq. 2.14 collapses to the simpler form of

$$\frac{d^2 q(\tau)}{d\tau^2} + \left[\Phi^2 - \alpha_0^2 \cos^2(\tau)\right] q(\tau) = \alpha_0 A_y \sin(\tau) \tag{5.7}$$

where Φ is defined as the ratio of the natural frequency to the driving frequency, or $\Phi = \omega_1/\omega$. Though the form is deceptively simple, the time-varying stiffness renders a closed-form analytic solution unattainable. Thus, we rely on approximate analytic solutions to garner physical insight into the system. We consider (1) a time-averaged solution and (2) a perturbation solution using uniform expansion. Both these results can be compared to the numeric solution of Eq. 5.7 solved using Matlab. We consider only steady-state solutions, neglecting transient free vibration of the wing.

Solution Methods

The time-averaged solution is addressed first. We achieve an approximate solution to Eq. 5.7 by averaging the time-varying stiffness term, allowing

$$K_{avg}^2 = \frac{1}{2\pi} \int_0^{2\pi} \left[\Phi^2 - \alpha_0^2 \cos^2(\tau)\right] d\tau = \left[\Phi^2 - \frac{\alpha_0^2}{2}\right] \tag{5.8}$$

Substituting this time-invariant stiffness into Eq. 5.7 yields a linear time-invariant (LTI) second-order differential equation. The steady-state solution to this ordinary differential equation, denoted q_{avg}, is simply

$$q_{avg}(\tau) = \frac{\alpha_0 A_y \sin(\tau)}{K_{avg}^2 - 1} \tag{5.9}$$

Next, the perturbation solution, labeled q_{pert}, is explained. Unlike the time-averaged solution, the perturbation solution captures some effects of the time-varying stiffness, which may have important physical implications. Provided α_0 is sufficiently small, we can use it as a perturbation parameter and write the modal response as a uniform expansion such that

$$q_{pert}(\tau) = q_0(\tau) + \alpha_0\, q_1(\tau) + \alpha_0^2\, q_2(\tau) + \mathcal{O}(\alpha_0^3) \tag{5.10}$$

We consider solutions up to $\mathcal{O}(\alpha_0^3)$; due to the small magnitude of α_0, solutions of higher order are negligible. After substituting Eq. 5.10 and its derivatives with respect to τ into Eq. 5.7, we collect terms of order α_0 and solve for the ordered modal responses separately. The perturbation solution yields

$$q_{pert}(\tau) = \alpha_0 A_y[(C_1 + \alpha_0^2\, C_2)\sin\tau + \alpha_0^2\, C_3 \sin 3\tau] + \mathcal{O}(\alpha_0^3) \tag{5.11}$$

where the coefficients determined above are given by

$$C_1 = \frac{1}{\Phi^2 - 1}; \qquad C_2 = \frac{C_1}{4}\left(\frac{1}{\Phi^2 - 1}\right); \qquad C_3 = \frac{C_1}{4}\left(\frac{1}{\Phi^2 - 9}\right) \tag{5.12}$$

From the perturbation solution, it is clear time-varying stiffness gives rise to a harmonic at 3τ in the modal response. Should higher orders of α_0 be considered, higher-order harmonics 5τ, 7τ, etc. will appear. These harmonics are only significant should α_0 become large.

Lastly, we solve Eq. 5.7 numerically. As we are interested principally in the steady-state response, we impart a small amount of modal damping ($\zeta = 0.01$) to allow the free vibration of the wing to diminish. Equation 5.7 is solved numerically using the built-in Matlab ODE45 solver. The equation is solved over 50 cycles to ensure steady-state with 1000 evenly spaced time-steps for each cycle. All relevant quantities in the following section are extracted from the last simulation cycle to reduce artifacts of free vibration.

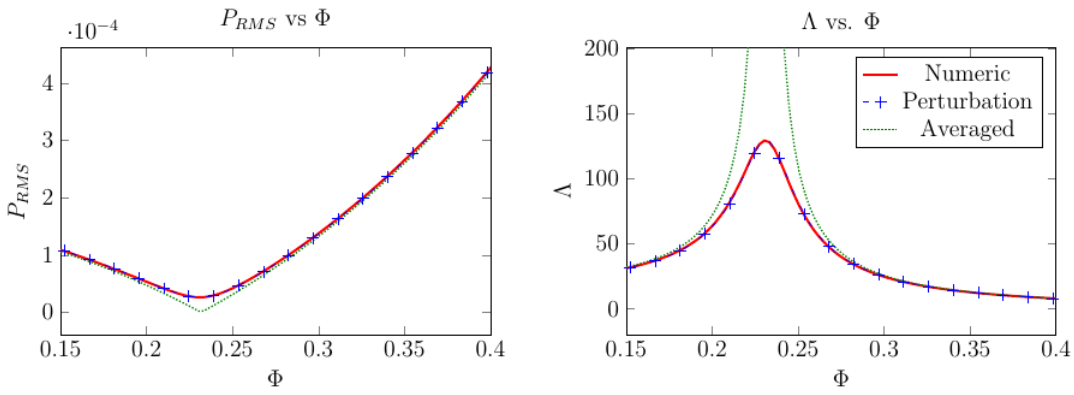

Figure 5.2: $P_{RMS}(\tau)$ as a function of Φ for three modal solution methods.

Power Considerations

With the analytic and numeric solutions at hand, the effect of elastic deformation on power consumption is investigated. The structural compliance of the wing is varied from $0 \leq \Phi \leq 5$ in 500 evenly-spaced increments, representing a range of fundamental frequencies from $0\,\text{Hz} \leq \omega_1 \leq 125\,\text{Hz}$. The inertial instantaneous power is calculated using Eq. 5.3. The time-normalized RMS total inertial power, $P_{RMS}(\tau)$, is determined as a function of Φ over the considered interval using all three solution methods. Simultaneously, we calculate the RMS power necessary to drive the rigid system such that the compliance ratio Λ defined in Eq. 5.6 can be determined as a function of Φ. We find total inertial RMS power has a global minimum when $\Phi \approx 0.23$ and a local minimum when $\Phi \approx 2.99$; consequently, Λ is maximized at these points. The perturbation solution reflects a singularity when $\Phi = 3$, which implies poor agreement between perturbation and numeric simulations around this point. Consequently, we focus our attention on the global RMS power minimum at $\Phi \approx 0.23$, where the perturbation method more accurately describes system behavior. Total RMS power and the compliance power ratio Λ around $\Phi \approx 0.23$ are shown for all three solution methods in Fig. 5.2.

All solution methods qualitatively capture the global minimum in RMS power when

$\Phi \approx 0.23$. However, only perturbation and numeric solutions reflect quantitative agreement. This suggests the time-varying stiffness has a marked effect, and therefore averaging the stiffness misses some characteristics of the wing response. Therefore, we elect to use the more accurate perturbation solution to analyze the wing behavior for the remainder of this section.

We next seek to identify how wing elasticity reduces overall power consumption. It can be shown that, using the expression for inertial power in Eq. 5.3 and accounting for the simplifications in this example, the power reduces to

$$P_{inertial}(\tau) = (I_{xx}\,\alpha'' + A_y\,\ddot{q})\,\alpha' + \mathcal{O}(q^2) \tag{5.13}$$

where the $'$ superscript denotes a derivative with respect to τ. Power terms of $\mathcal{O}(q^2)$ are neglected, as they correlate to the infinitesimal deformation and are comparatively small. We expand Eq. 5.13 in rigid and elastic component form to

$$P_{inertial}(\tau) = \underbrace{-\frac{\alpha_0^2}{2}\,I_{xx}\sin 2\tau}_{P_{rigid}(\tau)} \underbrace{-\frac{\alpha_0^2}{2}A_y^2\left[(C_1 + \alpha_0 C_2 + 9\alpha_0 C_3)\sin 2\tau + 9\alpha_0 C_3 \sin 4\tau\right]}_{P_{elastic}(\tau)} \tag{5.14}$$

P_{rigid} oscillates at 2τ, while $P_{elastic}$ oscillates at both 2τ and 4τ. Given the frequency content, it seems plausible a component of $P_{elastic}$ may entirely negate P_{rigid} under proper conditions. To further explore this, we collect coefficients of $\sin 2\tau$ in Eq. 5.14, equate them to zero and rearrange as follows.

$$\frac{I_{xx}}{A_y^2} = -[C_1 + \alpha_0(C_2 + 9C_3)] \tag{5.15}$$

Above, the left-hand-side represents a constant ratio between the moment of inertia about x and the $\hat{e}_y$ component of $\vec{a}_1$. In essence, this is a ratio describing the rigid moment of inertia to the elastic inertial force center. The right-hand-side of the equation represents a complicated function of Φ and α_0. Thus, the point at which $P_{elastic}$ cancels P_{rigid} depends not only on wing geometry and stiffness, but on rotation amplitude as well. We aim to identify

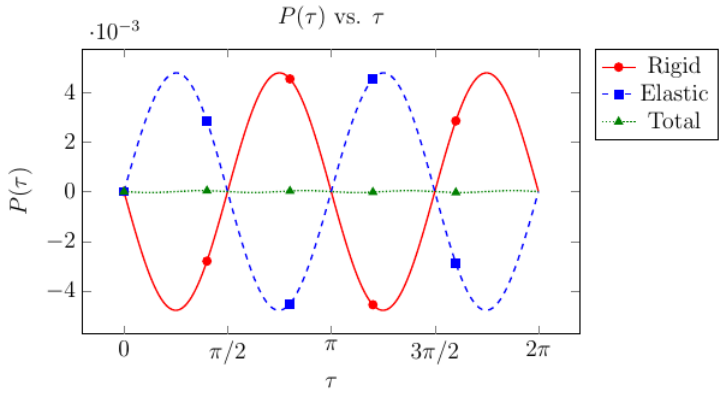

Figure 5.3: $P(\tau)$ versus τ at Φ =0.23, corresponding to a global minimum in RMS power

if the RMS power minimum in Fig 5.2 relates to a point where rigid inertial power is entirely canceled by elastic inertial power. We plot the rigid, elastic and total components of inertial power as a function of τ when $\Phi = 0.23$ (Fig. 5.3).

When $\Phi = 0.23$, the elastic power almost entirely negates rigid inertial power by merit of a π phase difference between 2τ components. The remaining 4τ component of elastic power is small, which implies compliance has substantially reduced energetic expenditures at steady-state. While it is tempting to extrapolate these results to consider increased rotation amplitudes, doing so violates the underlying assumption in the perturbation solution. Therefore, when considering large rotation amplitudes in the subsequent section, we must rely on numeric simulation only.

5.2.3 Example Two: Wing Rotating in Three Dimensions in Air

In this section, we present a wing subject to three-dimensional rotation under both aerodynamic and inertial-elastic forcing. As an analytic expression for elastic deformation is not readily attainable, we rely on numerical results only for this example. Nonetheless, some of the principles outlined in the previous section offer insight into the results presented hereafter.

We wish to determine the optimal wing kinematics and structural compliance necessary to minimize RMS power in a hovering insect. It is acknowledged a similar study has been conducted for a rigid wing [57]. However, given the addition of wing elasticity, power consumption may be further reduced. All rotations are assumed harmonic functions of the form $n = n_0 \sin(\omega t + \phi_n)$, where n_0 is a placeholder for rotation amplitudes in Fig. 4.2, and ϕ_n represents the phase of rotations. Vector $\vec{x}$ represents all parameters being optimized, where

$$\vec{x} = [\alpha_0 \ \beta_0 \ \phi_\beta \ \gamma_0 \ \phi_\gamma \ \omega_1]^T \tag{5.16}$$

Note that the roll phase ϕ_α is not included in the optimization parameters. Only relative phase of rotations is significant, and thus only two phase angles are necessary. The objective of this optimization is to reduce power consumption, specifically as it relates to battery life in FWMAVs. A constraint equation must also be established; otherwise, the optimal power-saving kinematics would dictate no flapping at all. We choose the identical lift condition as a constraint, and the optimization problem is written as

$$\begin{aligned} \underset{\vec{x}}{\text{minimize}} \quad & P_{RMS}(\vec{x}) \\ \text{subject to} \quad & \frac{< 2F_z >}{mg} = 1 \end{aligned} \tag{5.17}$$

where $< 2F_z >$ denotes the net vertical force produced by two wings averaged over a single wing-beat period, m denotes the total insect mass and g denotes the acceleration due to gravity. We bound the optimization parameters within reasonable anatomical limits given by

$$-180^\circ \leq \alpha_0, \quad \beta_0, \quad \gamma_0 \leq 180^\circ \tag{5.18}$$

$$0 \text{ Hz} \leq \quad \omega_1 \quad \leq 500 \text{ Hz} \tag{5.19}$$

Above, the natural frequency is constrained to half the sampling frequency used for numerical solutions. This upper bound in natural frequency is substantially higher than biologically

Table 5.2: Summary of Simulation Parameters

Parameter	**Optimization Result**	**Biological Value**	**Unit**
α_0	59.5	60	degrees
β_0	68.7	45	degrees
ϕ_β	1.58	$\pi/2$	rad
γ_0	-0.47	5	degrees
ϕ_γ	6.2	N/A	rad
ω_1	84.6	60 (air), 85 (vacuum)	Hz

measured values. Constraining the rotation phase angles resulted in optimizer complications, though it is simple to wrap the values within a $0 \leq \phi_n \leq 2\pi$ interval.

To determine the optimal solution, we use Matlab Optimization toolbox's built in fmincon function. The modal response and corresponding elastic deformation are determined numerically by solving Eq. 2.14; the equation of motion is no longer normalized with respect to time so that quantitative observations can be made. Details of this numeric solution are found in the previous section. Aerodynamic forces are determined using the blade-element aerodynamic model, and the total power is determined by Eq. 5.4. To ensure the optimization algorithm has indeed converged on a global solution within parameter bounds, we seed the optimizer at many random initial guesses. The optimization results, and their comparisons to approximated biological values presented in [3] and [74], are presented in Table 5.2.

Taking into consideration the significantly simplified model wing and approximate blade-element aerodynamic model, the optimized parameters match the biological values quite well, in particular the roll amplitude and natural frequency. We compare our natural frequency estimate to that determined by experimental modal testing in vacuum, as our model neglects fluid-structure interaction. Of the remaining parameters, the most glaring discrepancy is

pitch amplitude, which is addressed separately in the next paragraph. The yaw amplitude converges to a near-zero value. If optimizer tolerances are reduced (at the expense of an increase in computation time), the yaw amplitude further reduces. Sensitivity analysis around γ_0 shows that an increase in amplitude has a negligible effect on lift, consistent with the results presented in [75]. Despite these findings, the presence of wing yaw in biological fliers should not be ignored; this degree of freedom likely serves some other functional role, such as stabilization or maneuvering during flight [75]. Nonetheless, given the single constraint on sufficient lift, the results for yaw rotation are satisfactory.

The more disconcerting result is the over-estimation of the pitch amplitude, roughly 20° over the biologically measured value. We rely on biological data from the *Manduca sexta* in hover to explain this discrepancy. Insect wings are highly torsionally flexible, indicating the pitch angle along the wing span is not constant. High-speed videography reveals the pitch amplitude along the chord near the wing-tip is approximately 30° higher than the pitch amplitude of the chord closer to the wing-root [3]. The increased angle-of-attack near the wing-tip will drastically affect lift production and likely aerodynamic power. Unfortunately, the simple blade-element model assumes a rigid wing, and therefore cannot effectively capture torsional deformation. Conversely, the structural model is capable of accounting for torsion, however inclusion of a torsional mode had little influence on the kinematics determined through the optimization routine. Another potential source of error falls on the assumption that pitch undergoes simple harmonic motion. Several researchers utilize more complex rotation functions to account for asymmetric pitching between the wing upstroke and downstroke [60, 76]. This asymmetry is observed in nature [3], and may have both consequences on aerodynamic forces and inertial/aerodynamic power. Lastly, we point to the natural variation a means of discrepancy. The mean chordwidth, wing span, insect body mass, and kinematics all vary between insects. We are confined by idealized parameters, and consequently, convergence on a perfect solution is unlikely. Nonetheless, the presented methodology proves a useful tool for estimating optimal kinematics and structural compliance, particularly within a more controlled environment such as FWMAV design.

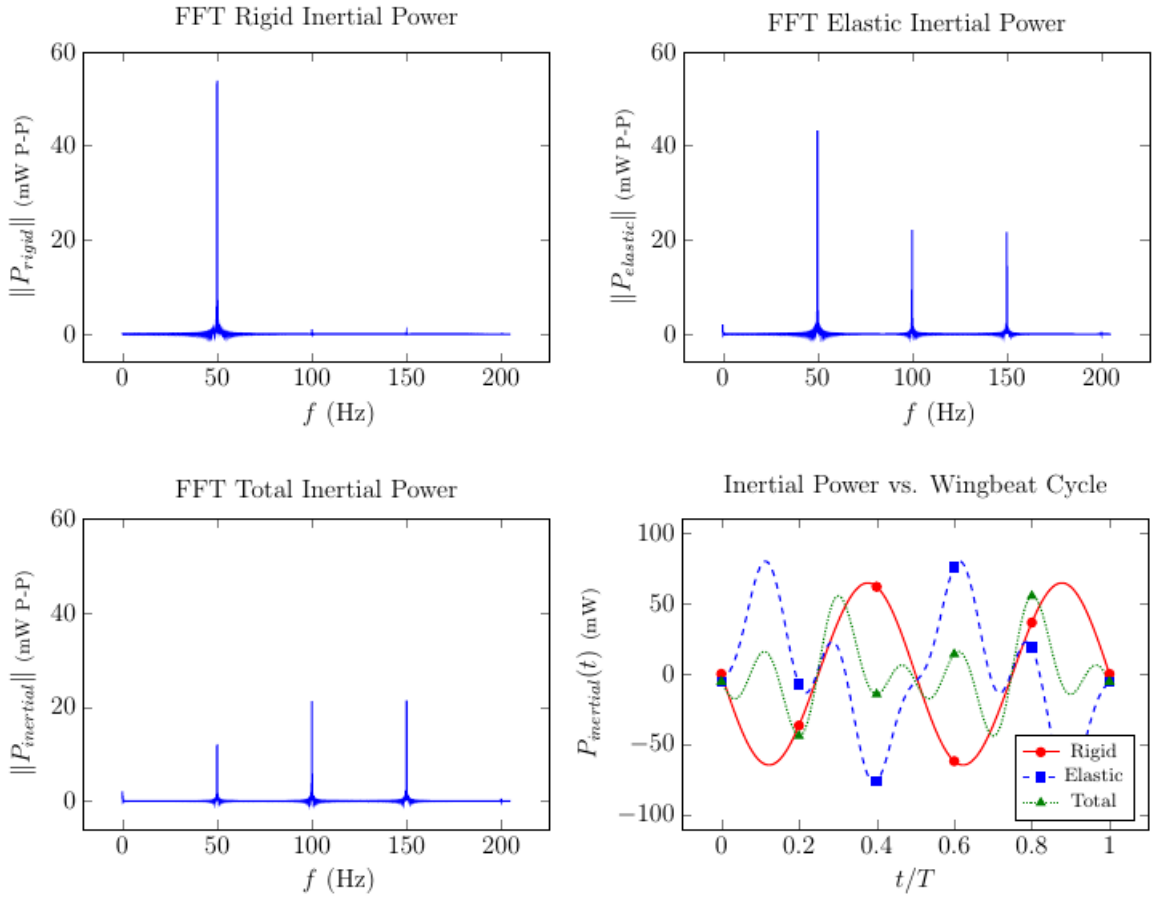

Figure 5.4: Inertial power in frequency and time domains.

With the optimal parameters determined, we turn our attention to total power consumption. Utilizing the parameters from Table 5.2 and neglecting yaw, we determine the instantaneous inertial, aerodynamic and total power as a function of the wingbeat cycle. The simulation is conducted for both rigid and compliant systems so deformation effects can be investigated. We first scrutinize total inertial power ($P_{inertial} = P_{rigid} + P_{elastic}$), or the power required to rotate the wing three-dimensionally in vacuum. Inertial powers in frequency and time domains are shown in Fig 5.4.

Simulation results show the dominate frequency component for both rigid and elastic

inertial powers occurs at 2ω. Interestingly, the total inertial power at 2ω is less than the individual rigid/elastic components, implying a phase difference between the two. Indeed, the relative phase between elastic and rigid powers at 2ω is nearly π, and as a result these components interact destructively. This trend is similar to that observed in the simple case of the wing rolling in vacuum, where a component of the elastic power completely canceled rigid power. In this case, however, perfect cancellation of rigid power cannot be achieved. Perfect cancellation requires larger rotation amplitudes, and increased rotation amplitudes are accompanied by increased lift; increased lift violates the constraint dictating net lift equals identically insect weight. Simply put, there exists only a narrow band of kinematic parameters capable of producing identically sufficient lift. Given this fact, it seems plausible kinematic parameters can be optimized independent of structural compliance, with the structural compliance determined via a grid search once kinematic parameters are established. The remaining components of the total inertial power arise from the elastic inertial power at 4ω and 6ω. At these frequencies, rigid power magnitude is small. It appears wing elasticity distributes power more homogeneously over a larger frequency band, and as a consequence, RMS inertial power is reduced.

We now focus on the most important quantity: total system power including aerodynamic and inertial-elastic components. Total system power is determined for the optimal configuration (Tab. 5.2). The aerodynamic, rigid system and elastic system powers are shown in time and frequency domains in Fig 5.5.

Fig. 5.5 shows the total power requirements (both RMS and maximum instantaneous) are less for the elastic system compared to the rigid system. The rigid system shows an appreciable power requirement at $f = 50$ Hz (twice the flapping frequency). However, due to the inertial power cancellation illustrated previously, the power requirement at $f = 50$ Hz for the total system is almost entirely from aerodynamic effects. Aerodynamic forces also cause the large DC offset seen in total power requirements. The remaining power is contained almost entirely at $f = 100, 150$ Hz and arises from inertial power required for elastic deformation. Under the optimal configuration shown in Tab. 5.2, the compliance

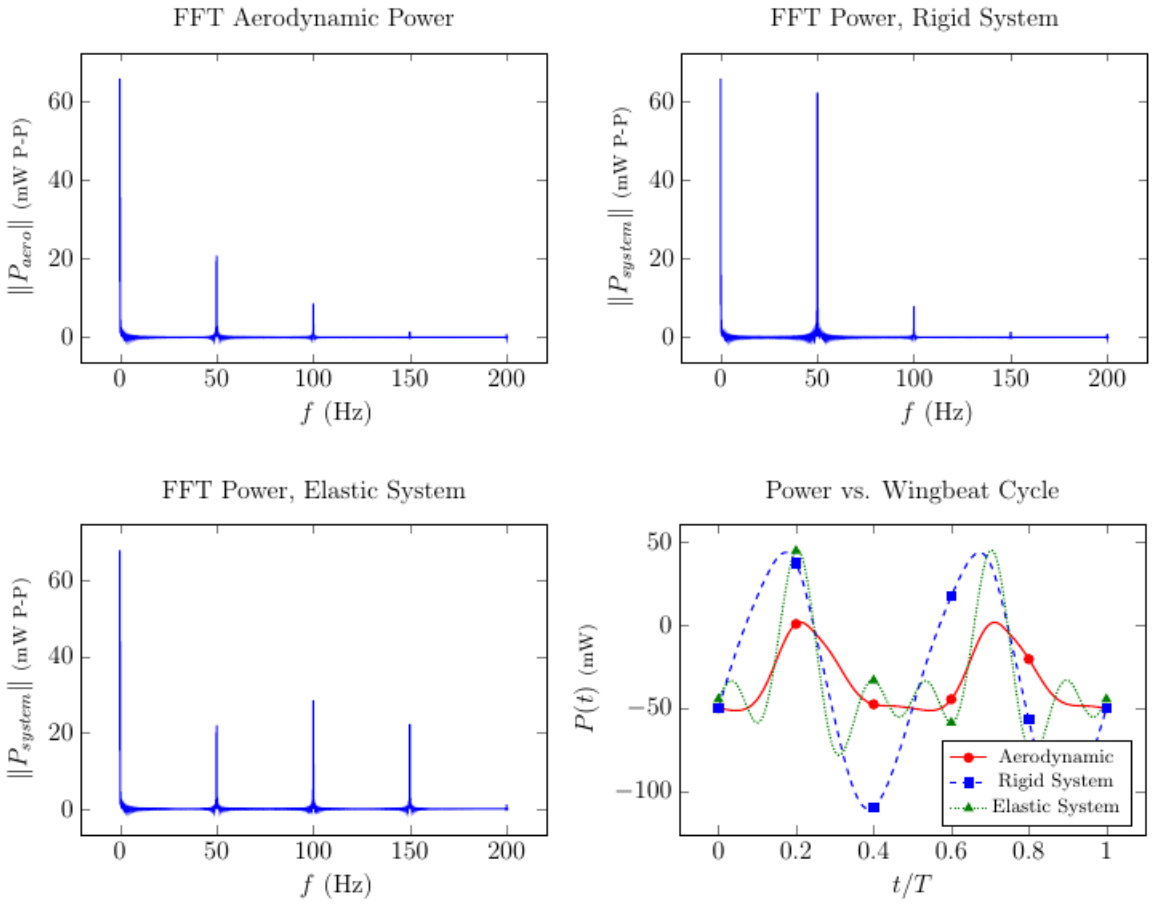

Figure 5.5: Aerodynamic, rigid system, and elastic system power in frequency and time domains.

power ratio is $\Lambda = 1.32$, representing a 25% reduction in the RMS power necessary for rigid-wing flight. Considering the power necessary to flap two elastic wings and total insect mass (Tab. 5.1), this translates into a net power per body mass requirement of $P_{max} = 95$ W/kg for Hawkmoth *Manduca sexta* flight. This maximum power estimate is on the same order of magnitude as the power produced by the largest flight muscle in the *Manduca sexta* [77], inspiring some confidence in the quantitative accuracy of simulation results.

Lastly, we conduct a sensitivity analysis about the optimal natural frequency to identify

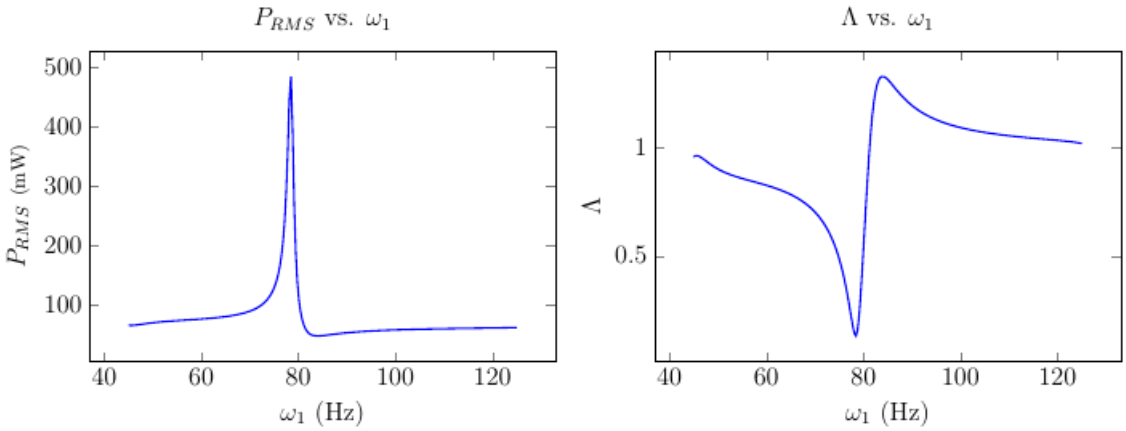

Figure 5.6: Total RMS Power and compliance ratio as functions of natural frequency using optimized kinematics.

the range of natural frequencies where $\Lambda \geq 1$. Again, the optimal parameters from Table 5.2 are used, with yaw set to zero. Both total RMS power and compliance power ratio are shown as functions of the natural frequency ω_1 in Fig. 5.6. The results show a clear minimum at the optimized value of $\omega_1 = 84.6$ Hz, representing the maximum 25% reduction in RMS power. Moreover, in the range where $\omega_1 \geq 84.6$ Hz, the compliance power ratio is greater than one. As the natural frequency grows, the compliance power ratio asymptotically approaches one; this represents the case where the wing is becoming rigid. Nonetheless, there is a broad range of natural frequencies where compliance benefits can be leveraged, an important implication for FWMAV wing design.

5.3 Discussion

The entirety of the results illustrate that wing flexibility can decrease energetic expenditures. These findings corroborate the conclusions of several other researchers investigating power expenditure in insect flight [72, 70, 71], with our estimate suggesting wing compliance reduces power expenditures up to 25% under specific conditions. For realistic flight conditions, simulation results suggest these energetic benefits are realized when $\omega/\omega_1 \leq 0.3$, identically

the condition proposed by Dai, Luo and Doyle [78]. Perhaps not by coincidence, many flapping insects exhibit a similar driving frequency to fundamental frequency ratio [79]. Thus, in the development of small-scale power-efficient FWMAVs, flying insect can potentially serve as design paradigms, with the methodology derived here guiding optimal wing design.

Most critically, our results rely on detailed knowledge of wing mode shapes and natural frequencies. These parameters are functions of several variables, including material stiffness, density, and mass distribution. While mode shapes and natural frequencies can be estimated via finite element analysis, it is crucial to validate computational results with experimental modal testing. We believe modal testing should be an integral component to any wing design where elastic deformation is nontrivial. However, structural characterization should not supersede evaluation of aerodynamic performance. First and foremost, wing designs should be tested under varying kinematics to ensure sufficient lift and thrust are attainable. Such aerodynamic forces rely largely on wing surface area distribution and camber, with mass distribution and stiffness (and effectively, elastic deformation) playing secondary roles. Once desirable aerodynamic performance is achieved, structural compliance can be modified to reduce inertial power expenditures. This can be achieved through several means, where the simplest approach involves varying Young's moduli through material selection. However, given the finite range of materials suitable for wing design, material variation alone is likely insufficient. Instead, emphasis should be placed on the geometry of the forewing strut, the analog to the dominate load-bearing radial vein in insects [80]. The radial vein, running along the leading edge, is generally thicker than the remainder of the wing and may significantly affect span-wise rigidity. In terms of FWMAV wing design, even modest variation in forewing strut effective diameter affects structural stiffness while leaving total wing surface area relatively unchanged. Thus, conscientious design of the forewing strut, both in material in geometry, allows control over wing fundamental frequency with only secondary effects impacting aerodynamics. Of course, an increase in strut effective diameter could adversely affect wing mass, though it likely has a negligible contribution to vehicle mass as a whole.

Despite the promise of these preliminary findings, there are several aspects for power min-

imization beyond wing design which must be considered. Our model neglects coupling between wing and drive-train components, treating the FWMAV actuator as a periodic source. The Harvard Robobee uses piezoelectric actuators to generate gross wing motion [81], and the actuator itself has some elasticity. Should the resonant properties of the wing and actuator be similar, the two systems shall behave as coupled oscillators. This result by itself is not necessarily harmful; in fact, coupled oscillator behavior may further mitigate energetic requirements. However, should this behavior be observed, the model in this paper should be reformulated to account for the elastic behavior of the actuator. Furthermore, the presented work assumes all rotational degrees of freedom are controlled. In reality, many FWMAVs utilize passive pitch, allowing the wing inertia to pitch the wing rather than an independent actuator. This mechanism may also improve power efficiency, as the angle-of-attack is achieved passively rather than actively. If a FWMAV relies on passive pitch, the equation of motion for the pitch angle β should treated as a variable to be solved for. Lastly, wing length scale must be considered. The example presented considers the comparatively large Hawkmoth *Manduca sexta*. Many insects have wing spans an order of magnitude smaller. Researchers conjecture smaller insects benefit only marginally from elastic wings owing to the reduced inertial costs of flapping [33]. This hypothesis makes intuitive sense, as inertial forces are of similar magnitude compared to aerodynamic forces in small insects; inertial forces tend to exceed aerodynamic forces at larger scales [75]. Thus, there are several engineering decisions that must be made while creating power-efficient drivetrains, highlighting the degree of complexity associated with insect-scale robotic design. The framework derived in this paper offers a general tool for energy-minimizing compliant wing design; modified forms of this framework should be employed on an application-to-application basis.

Chapter 6

CONCLUSION

In Chapter 2, a comprehensive dynamic model of an insect wing is developed treating the wing as a deformable body subject to three dimensional rotation about a fixed point on the insect's body. A coordinate frame that rotates with the finite pitch and roll rotations is established. A third yaw rotation is assumed small, and is allowed to rotate independently of the coordinate frame. The kinetic and potential energies are formulated, and the set of uncoupled differential equations describing the time response of each mode shape (determined by finite element analysis) is determined by Lagrange's equation. There are several advantages to such a formulation. First, the model is able to estimate the time-dependent strain components on the wing. Second, the model allows any complex geometry to be implemented readily. Third, the resulting model has reduced order— the order of the model is the number of mode shapes retained.

The model is then applied to the forewing of the *Manduca sexta*. Coriolis, Euler, and centrifugal forces are identified excitation terms responsible for the elastic deformation of the wing. The Coriolis force tends to dominate the first mode whereas the centrifugal force tends to dominate the second mode. Numerical integration indicates a beat phenomenon occurs in both the first and second modal responses. A time-invariant approximation shows the beat phenomenon is a result of the interaction of free vibration and Coriolis forcing in the first mode, and the interaction of free vibration and centrifugal forcing in the second mode. The sensitivity of the beat phenomenon in the fundamental mode is explored. The beat phenomenon is relatively insensitive to various yaw amplitudes and non-zero initial conditions, but decays gradually in the presence of damping. Resetting of initial conditions or slight variations of the yaw amplitude cause the beat phenomenon to persist even in the

presence of damping.

The total time-dependent normal and shear strain components are calculated at a point of interest near the base of the wing. The shear strain component is determined to be significantly larger than the normal strain components. In all cases, the strain components exhibit a beat phenomenon. This result suggests the *Manduca sexta* may use strain frequency data associated with the beat phenomenon to help identify flight status. In the context of MAVs, similar strain-based control systems may be developed to replace or supplement traditional acceleromater-based control systems. This can potentially increase MAV performance by reducing weight, size, and power consumption.

In Chapter 3, we presented experimental studies of a rotating wing. An aluminum triangular model wing was placed in a custom two-axis rotation stage, and experiments took place in and out of vacuum conditions to decouple aerodynamic and inertial effects. Temporal strain was measured at a point near the wing root. The derived reduced-order model utilized only two modal degrees-of-freedom and estimated the strain within reasonable accuracy. This is a dramatic improvement over a rigorous FEA approach, which requires excessive computational resources. The inertial-elastic model may be beneficial in studies where a large parameter space is considered and minimizing computational load is preeminent. Moreover, the model may be extended to include more complex geometries, namely the geometry of a FWMAV forewing.

The experiment also showed gyroscopic forces indeed have a substantial effect on dynamic bending. While gyroscopic forces do excite torsional modes, a claim made by Eberle et al. [45], the results presented show a far more significant contribution of gyroscopic forces to bending modes, particularly as a result pitching. These gyroscopic forces (related to the wing yaw) occurred at twice the driving frequency, which falls near the first resonance frequency of the *Manduca sexta* [39]. Even without the resonance phenomena, the experimental work shows gyroscopic forces are as much as four times the inertial forces in the pitch-yaw orientation. Should the resonance phenomena be leveraged in the design of a FWMAV wing, it may be plausible to realize a highly sensitive strain-based gyroscope.

In Chapter 4, we presented an integrated aerodynamic/inertial-elastic rotating wing model to assess to relative contribution of aerodynamic and inertial moments on steering maneuvers in insect flight. Insects exhibit a strong correlation between aerial maneuvers and stroke deviation actuation. To investigate the mechanisms underlying this correlation, we developed an integrated aerodynamic/inertial model of flapping wings to predict forces, torques and impulses that arise from stroke deviations. The model is linearized by the small stroke deviation angle such that zeroeth order terms are contingent only on wing pitch and roll whereas first order terms rely on all three rotations. The stroke deviation amplitude is fixed, and the phase is varied to represent changes in insect steering muscle firing latency.

The results elucidate the functional role of the stroke deviation angle, which is strongly correlated to steering muscle activity. The stroke deviation angle has an insignificant effect on aerodynamic force production – rather, lift and thrust largely relied on symmetric wing pitch and roll. Variance of the stroke deviation phase has a large effect on the steady-state averaged aerodynamic moments acting at the fixed point, which are necessary to reorient the insect body. These results corroborate observations in which steering muscle activity was correlated to various aerial maneuvers [48].

The angular momentum of the wing was also found to vary with the stroke deviation phase, motivating a closer look into the transient period during which the stroke deviation varies phase. During the transient period, both inertial and aerodynamic impulses play significant roles, with the latter in growing in magnitude as the duration of the transient period increases. Such a result suggests that, in contrast to prevailing views that only aerodynamic forces are implicated in flight control, inertial moments generated by steering muscles facilitate changes in body orientation, particularly if phase shifts occur on sub wing beat timescales. Simulations show inertial effects become less pronounced for smaller flying insects. Additionally, achievable body yaw rates fell within anatomical limits for most temporal phase shifts.

Insights into how the stroke deviation angle can benefit FWMAV drive-train and control system design were given. The addition of an actuator modulating stroke deviation is pur-

ported to decouple lift/thrust production from and steering mechanisms. The benefit of such a deconvolution is the ability to maintain power actuators at an optimal set point. Thus, power actuators can be utilized to generate gross wing trajectory, whereas smaller control actuators can be used to finely modify wing kinematics thereby inducing aerial maneuvers. These aerial maneuvers can further be refined by leveraging inertial mechanisms arising from quick shifts in stroke deviation phase.

Lastly, Chapter 5 investigated the effect of wing structural compliance on power expenditures in insect flight. Flying insects minimize power expenditure by converting some wing kinetic energy to stored strain energy during the wingbeat cycle. To determine the effect of compliance on energy efficiency, we derived a model estimating the power necessary to actuate an elastic planar wing in air. A rigid-body approximation is used to estimate aerodynamic power. The model is applied to two examples: (1) a simple case of a wing rolling in a vacuum, and (2) a more complex case of a wing rotating in three dimensions in air.

The simple example indicates that under certain circumstances, wing deformation reduces both RMS and peak instantaneous powers. This reduction is contingent on time-varying wing stiffness, and is achieved when rigid-body power is fully or partially counteracted by the power associated with elastic deformation. Excessive deformation is detrimental; while rigid-body power is entirely negated, large bending incurs additional energetic penalties. The range of power-reducing natural frequencies is a function of several parameters, including rotation amplitude, moment of inertia, and location of the vibratory inertial force center.

Next, we optimized the kinematics and structural compliance of an elastic wing rotating in three dimensions in air. We constrained the optimization problem such that sufficient lift is produced for hover and minimized total RMS power. The wing kinematics and stiffness converged closely to experimentally measured values for the Hawkmoth *Manduca sexta*, with the largest discrepancy occurring in pitch amplitude; we believe this disparity arises from unmodeled torsional flexibility. Under the optimal configuration, wing compliance reduces total RMS power requirements by as much as 25% by virtue of elastic deformation abating total inertial power. The optimal natural frequency is only modestly sensitive, and a range

of natural frequencies where $\omega_1 \geq 84.6$ Hz offers benefits in power reduction.

Lastly, we comment on how these findings benefit FWMAV wing design. Most notably, our results emphasize the necessity of experimental modal testing to determine wing natural frequencies and mode shapes. Natural frequencies can readily be tuned by adjusting the effective diameter or material of the forewing strut. This should be conducted after the aerodynamic performance of the wing is evaluated; minor variations in structural compliance are speculated to have only a secondary effect on aerodynamic forces.

We hope the ideas presented in this dissertation will inspire new technologies and facilitate the advancement of FWMAVs, and offer novel insights into the complicated mechanisms of insect flight. I have thoroughly enjoyed taking part in this wonderfully complex research, and hope to continue to advance my own understanding of this exciting topic for years to come.

BIBLIOGRAPHY

[1] Noriyasu Ando and Ryohei Kanzaki. Changing motor patterns of the 3rd axillary muscle activities associated with longitudinal control in freely flying hawkmoths. *Zoological science*, 21(2):123–130, 2004.

[2] Hirotaka Sato, Tat Thang Vo Doan, Svetoslav Kolev, Ngoc Anh Huynh, Chao Zhang, Travis L Massey, Joshua Van Kleef, Kazuo Ikeda, Pieter Abbeel, and Michel M Maharbiz. Deciphering the role of a coleopteran steering muscle via free flight stimulation. *Current Biology*, 25(6):798–803, 2015.

[3] Alexander P Willmott and Charles P Ellington. The mechanics of flight in the hawkmoth manduca sexta. i. kinematics of hovering and forward flight. *Journal of Experimental Biology*, 200(21):2705–2722, 1997.

[4] J. Gago, C. Douthe, R.E. Coopman, P.P. Gallego, M. Ribas-Carbo, J. Flexas, J. Escalona, and H. Medrano. UAVs challenge to assess water stress for sustainable agriculture. *Agricultural Water Management*, 153:9–19, may 2015.

[5] Lionel Heng, Dominik Honegger, Gim Hee Lee, Lorenz Meier, Petri Tanskanen, Friedrich Fraundorfer, and Marc Pollefeys. Autonomous visual mapping and exploration with a micro aerial vehicle. *Journal of Field Robotics*, 31(4):654–675, jun 2014.

[6] Alexander E. MacDonald. A global profiling system for improved weather and climate prediction. *Bull. Amer. Meteor. Soc.*, 86(12):1747–1764, dec 2005.

[7] Daniel Mellinger, Michael Shomin, Nathan Michael, and Vijay Kumar. Cooperative grasping and transport using multiple quadrotors. In *Springer Tracts in Advanced Robotics*, pages 545–558. Springer Science Business Media, 2013.

[8] Adam P. Tobias. *Experimental methods to characterize nonlinear vibration of flapping wing micro air vehicles*. PhD thesis, Air Force Institute of Technology, 2007.

[9] Srijaya Mohan and G Sridharan. Emerging technologies for micro unmanned air vehicles (review paper). *Defence Science Journal*, 51(3):223–228, 2002.

[10] Wang Zheng-jie and Li Wei. A solution to cooperative area coverage surveillance for a swarm of mavs. *International Journal of Advanced Robotic Systems*, 10(398):1–8, 2013.

[11] Bruno A. Roccia, Sergio Preidikman, Julio C. Massa, and Dean T. Mook. Development of a kinematical model to study the aerodynamics of flapping-wings. *International Journal of Micro Air Vehicles*, 2011.

[12] Alper Bozkurt, Robert F Gilmour Jr, and Amit Lal. Balloon-assisted flight of radio-controlled insect biobots. *Biomedical Engineering, IEEE Transactions on*, 56(9):2304–2307, 2009.

[13] Robotic bird flies at pack expo 2012, providing control insights. *Control Engineering*, 59(12):19, 2012.

[14] G C H E de Croon, M A Groen, C De Wagter, B Remes, R Ruijsink, and B W van Oudheusden. Design, aerodynamics and autonomy of the DelFly. *Bioinspir. Biomim.*, 7(2):025003, May 2012.

[15] Matthew Keennon, Karl Klingebiel, and Henry Won. Development of the nano hummingbird: A tailless flapping wing micro air vehicle. In *50th AIAA Aerospace Sciences Meeting including the New Horizons Forum and Aerospace Exposition*. American Institute of Aeronautics and Astronautics (AIAA), jan 2012.

[16] R.J. Wood. Liftoff of a 60mg flapping-wing mav. In *Intelligent Robots and Systems*.

[17] David B. Mayo and J. Gordon Leishman. Comparison of the hovering efficiency of rotating wing and flapping wing micro air vehicles. *J. Am. Helicopter Society*, 55(2):025001, 2010.

[18] Mostafa Nabawy and William James Crowther. Is flapping flight aerodynamically efficient? 2014.

[19] Umberto Pesavento and Z. Jane Wang. Flapping wing flight can save aerodynamic power compared to steady flight. *Phys. Rev. Lett.*, 103(11), sep 2009.

[20] WSN Trimmer. Microrobots and micromechanical systems. *Sensors Actuators*, 1989.

[21] Xiang-Xiang Jin, Hai-Feng Bai, and Cheng-De Li. A taxonomic study of ooctonus (hymenoptera, mymaridae) from heilongjiang, china. *ZooKeys*, 479:25–36, jan 2015.

[22] V. Kumar and N. Michael. Opportunities and challenges with autonomous micro aerial vehicles. *The International Journal of Robotics Research*, 31(11):1279–1291, aug 2012.

[23] Sawyer B Fuller, E Farrell Helbling, Pakpong Chirarattananon, and Robert J Wood. Using a mems gyroscope to stabilize the attitude of a fly-sized hovering robot. In *IMAV 2014: International Micro Air Vehicle Conference and Competition 2014, Delft, The Netherlands, August 12-15, 2014*. Delft University of Technology, 2014.

[24] M. F. Land and T. S. Collett. Chasing behaviour of houseflies (fannia canicularis). *Journal of Comparative Physiology*, 89(4):331–357, 1974.

[25] Robert J Wood. The first takeoff of a biologically inspired at-scale robotic insect. *Robotics, IEEE Transactions on*, 24(2):341–347, 2008.

[26] T.L. Daniel and S.A. Combes. Into thin air: contributions of aerodynamic and inertial-elastic forces to wing bending in the hawkmoth manduca sexta. *The Journal of Experimental Biology*, 2003.

[27] T Nakata, H Liu, Y Tanaka, N Nishihashi, X Wang, and A Sato. Aerodynamics of a bio-inspired flexible flapping-wing micro air vehicle. *Bioinspir. Biomim.*, 6(4):045002, nov 2011.

[28] B. H. Dickerson, Z. N. Aldworth, and T. L. Daniel. Control of moth flight posture is mediated by wing mechanosensory feedback. *Journal of Experimental Biology*, 217(13):2301–2308, apr 2014.

[29] Tanvi Deora, Amit Kumar Singh, and Sanjay P. Sane. Biomechanical basis of wing and haltere coordination in flies. *Proceedings of the National Academy of Sciences*, 112(5):1481–1486, jan 2015.

[30] Michael H Dickinson and Michael S Tu. The function of dipteran flight muscle. *Comparative Biochemistry and Physiology Part A: Physiology*, 116(3):223–238, 1997.

[31] Tanvi Deora, Amit Kumar Singh, and Sanjay P Sane. Biomechanical basis of wing and haltere coordination in flies. *Proceedings of the National Academy of Sciences*, 112(5):1481–1486, 2015.

[32] Simon Sponberg, Thomas L Daniel, and Adrienne L Fairhall. Dual dimensionality reduction reveals independent encoding of motor features in a muscle synergy for insect flight control. *PLoS Comput Biol*, 11(4):e1004168, 2015.

[33] CP Ellington. The aerodynamics of hovering insect flight. vi. lift and power requirements. *Philosophical Transactions of the Royal Society of London B: Biological Sciences*, 305(1122):145–181, 1984.

[34] Torkel Weis-Fogh. A rubber-like protein in insect cuticle. *Journal of Experimental Biology*, 37(4):889–907, 1960.

[35] Elliot W Hawkes and David Lentink. Fruit fly scale robots can hover longer with flapping wings than with spinning wings. *Journal of The Royal Society Interface*, 13(123):20160730, 2016.

[36] Christopher T. Orlowski and Anouck R. Girard. Modeling and simulation of nonlinear dynamics of flapping wing micro air vehicles. *AIAA Journal*, 2011.

[37] Satish K. Chimakurthi and Carlos E. S. Cesnik. Flapping-wing structural dynamics formulation basedon a corotational shell finite element. *AIAA Journal*, 2011.

[38] Alexander P. Willmott and Charles P. Ellington. The mechanics of flight in the hawkmoth manduca sexta. *The Journal of Experimental Biology*, 1997.

[39] Aaron G. Norris, Anthony N. Palazotto, and Richard G. Cobb. Experimental structural dynamic characterization of the hawkmoth (manduca sexta) forewing. *International Journal of Micro Air Vehicles*, 2013.

[40] Travis W. Sims. *A Structural Dynamic Analysis of a Manduca Sexta Forewing*. PhD thesis, Air Force Institute of Technology, 2010.

[41] Mark A. Frye. Encoding properties of the wing hinge stretch receptor in the hawkmoth manduca sexta. *The Journal of Experimental Biology*, 2001.

[42] Moble Benedict Pranay Seshadri and Inderjit Chopra. Understanding micro air vehicle flapping-wing aerodynamics using force and flowfield measurements. *Journal of Aircraft*, 2013.

[43] Mustafa Percin Shuanghou Deng, Bas van Oudheusden, Bart Remes, and Hester Bijl. Experimental investigation on the aerodynamics of a bio-inspired flexible flapping wing micro air vehicle. *International Journal of Micro Air Vehicles*, 2014.

[44] Gregory Paker Bret Stanford, Jose Miranda and Philip Beran. The complicating effect of uncertain flapping wing kinematics on model validation. *International Journal of Micro Air Vehicles*, 2011.

[45] P. G. Reinhall A. L. Eberle, B. H. Dickerson and T. L. Daniel. A new twist on gyroscopic sensing: body rotations lead to torsion in flapping, flexing insect wings. *Journal of the Royal Society*, 2015.

[46] Inderjit Chopra Ria Malhan, Moble Benedict. Experimental studies to understand the hover and forward flight performance of a mav-scale flapping wing concept. *Journal of the American Helicopter Society*, 2012.

[47] SA Combes and TL Daniel. Flexural stiffness in insect wings i. scaling and the influence of wing venation. *Journal of experimental biology*, 206(17):2979–2987, 2003.

[48] Hao Wang, Noriyasu Ando, and Ryohei Kanzaki. Active control of free flight manoeuvres in a hawkmoth, agrius convolvuli. *Journal of Experimental Biology*, 211(3):423–432, 2008.

[49] Claire N Balint and Michael H Dickinson. The correlation between wing kinematics and steering muscle activity in the blowfly calliphora vicina. *Journal of experimental biology*, 204(24):4213–4226, 2001.

[50] Jiang Hao Wu and Mao Sun. Unsteady aerodynamic forces of a flapping wing. *Journal of Experimental Biology*, 207(7):1137–1150, 2004.

[51] Mao Sun and Jian Tang. Lift and power requirements of hovering flight in drosophila virilis. *Journal of Experimental Biology*, 205(16):2413–2427, 2002.

[52] Hikaru Aono, Satish Kumar Chimakurthi, Pin Wu, E Sallstrom, Bret K Stanford, C Cesnik, Peter Ifju, Lawrence Ukeiley, and Wei Shyy. A computational and experimental study of flexible flapping wing aerodynamics. In *48th AIAA aerospace sciences meeting including the new horizons forum and aerospace exposition*, pages 4–7, 2010.

[53] QT Truong, QV Nguyen, VT Truong, HC Park, DY Byun, and NS Goo. A modified blade element theory for estimation of forces generated by a beetle-mimicking flapping wing system. *Bioinspiration & biomimetics*, 6(3):036008, 2011.

[54] JP Whitney and RJ Wood. Aeromechanics of passive rotation in flapping flight. *Journal of Fluid Mechanics*, 660:197–220, 2010.

[55] J Colorado, Antonio Barrientos, Claudio Rossi, and C Parra. Inertial attitude control of a bat-like morphing-wing air vehicle. *Bioinspiration & biomimetics*, 8(1):016001, 2012.

[56] Jonathan P Dyhr, Kristi A Morgansen, Thomas L Daniel, and Noah J Cowan. Flexible strategies for flight control: an active role for the abdomen. *Journal of Experimental Biology*, 216(9):1523–1536, 2013.

[57] Gordon J Berman and Z Jane Wang. Energy-minimizing kinematics in hovering insect flight. *Journal of Fluid Mechanics*, 582:153–168, 2007.

[58] Sanjay P Sane. The aerodynamics of insect flight. *Journal of experimental biology*, 206(23):4191–4208, 2003.

[59] Sanjay P Sane and Michael H Dickinson. The aerodynamic effects of wing rotation and a revised quasi-steady model of flapping flight. *Journal of experimental biology*, 205(8):1087–1096, 2002.

[60] Tyson L Hedrick and TL Daniel. Flight control in the hawkmoth manduca sexta: the inverse problem of hovering. *Journal of Experimental Biology*, 209(16):3114–3130, 2006.

[61] Toshiyuki Nakata, Hao Liu, and Richard J Bomphrey. A cfd-informed quasi-steady model of flapping-wing aerodynamics. *Journal of Fluid Mechanics*, 783:323–343, 2015.

[62] Sanjay P Sane and Michael H Dickinson. The control of flight force by a flapping wing: lift and drag production. *Journal of experimental biology*, 204(15):2607–2626, 2001.

[63] William B Dickson, Andrew D Straw, Christian Poelma, and Michael H Dickinson. An integrative model of insect flight control. In *Proceedings of the 44th AIAA Aerospace Sciences Meeting and Exhibit*, pages 31–38, 2006.

[64] Simon M Walker, Daniel A Schwyn, Rajmund Mokso, Martina Wicklein, Tonya Müller, Michael Doube, Marco Stampanoni, Holger G Krapp, and Graham K Taylor. In vivo time-resolved microtomography reveals the mechanics of the blowfly flight motor. *PLoS Biol*, 12(3):e1001823, 2014.

[65] Bo Cheng, Xinyan Deng, and Tyson L Hedrick. The mechanics and control of pitching manoeuvres in a freely flying hawkmoth (manduca sexta). *Journal of Experimental Biology*, 214(24):4092–4106, 2011.

[66] Tyson L Hedrick, Bo Cheng, and Xinyan Deng. Wingbeat time and the scaling of passive rotational damping in flapping flight. *Science*, 324(5924):252–255, 2009.

[67] Armin J Hinterwirth and Thomas L Daniel. Antennae in the hawkmoth manduca sexta (lepidoptera, sphingidae) mediate abdominal flexion in response to mechanical stimuli. *Journal of Comparative Physiology A*, 196(12):947–956, 2010.

[68] Benjamin M Finio, John P Whitney, and Robert J Wood. Stroke plane deviation for a microrobotic fly. In *Intelligent Robots and Systems (IROS), 2010 IEEE/RSJ International Conference on*, pages 3378–3385. IEEE, 2010.

[69] John Young, Simon M Walker, Richard J Bomphrey, Graham K Taylor, and Adrian LR Thomas. Details of insect wing design and deformation enhance aerodynamic function and flight efficiency. *Science*, 325(5947):1549–1552, 2009.

[70] Gang Du and Mao Sun. Effects of wing deformation on aerodynamic forces in hovering hoverflies. *Journal of Experimental Biology*, 213(13):2273–2283, 2010.

[71] Albert Medina, Jeff D Eldredge, Jihoon Kweon, and Haecheon Choi. Illustration of wing deformation effects in three-dimensional flapping flight. *AIAA Journal*, 53(9):2607–2620, 2015.

[72] Fritz-Olaf Lehmann, Stanislav Gorb, Nazri Nasir, and Peter Schützner. Elastic deformation and energy loss of flapping fly wings. *Journal of Experimental Biology*, 214(17):2949–2961, 2011.

[73] Travis W Sims, Anthony N Palazotto, and Aaron Norris. A structural dynamic analysis of a manduca sexta forewing. *International Journal of Micro Air Vehicles*, 2(3):119–140, 2010.

[74] Aaron G Norris, Anthony N Palazotto, and Richard G Cobb. Experimental structural dynamic characterization of the hawkmoth (manduca sexta) forewing. *International Journal of Micro Air Vehicles*, 5(1):39–54, 2013.

[75] Mark Jankauski, T.L. Daniel, and I.Y. Shen. Asymmetries in wing inertial and aerodynamic torques contribute to steering in flying insects. *Bioinspiration and Biomimetics*, 2017.

[76] Brian T Hinson and Kristi A Morgansen. Gyroscopic sensing in the wings of the hawkmoth manduca sexta: the role of sensor location and directional sensitivity. *Bioinspiration & biomimetics*, 10(5):056013, 2015.

[77] Michael S Tu and Thomas L Daniel. Submaximal power output from the dorsolongitudinal flight muscles of the hawkmoth manduca sexta. *Journal of Experimental Biology*, 207(26):4651–4662, 2004.

[78] Hu Dai, Haoxiang Luo, and James F Doyle. Dynamic pitching of an elastic rectangular wing in hovering motion. *Journal of Fluid Mechanics*, 693:473, 2012.

[79] Ngoc San Ha, Quang Tri Truong, Nam Seo Goo, and Hoon Cheol Park. Relationship between wingbeat frequency and resonant frequency of the wing in insects. *Bioinspiration & biomimetics*, 8(4):046008, 2013.

[80] A Roland Ennos. The importance of torsion in the design of insect wings. *Journal of Experimental Biology*, 140(1):137–160, 1988.

[81] Kevin Y Ma, Pakpong Chirarattananon, Sawyer B Fuller, and Robert J Wood. Controlled flight of a biologically inspired, insect-scale robot. *Science*, 340(6132):603–607, 2013.

[82] G.K. Batchelor. *An Introduction to Fluid Dynamics*. Cambridge, 1967.

[83] R.C. Michelson and S. Reece. Update on flapping wing micro air vehicle research. In *Proceedings of 13th Bristol International RPV Conference*.

[84] Robin J Wootton. The mechanical design of insect wings. *Scientific American*, 1990.

[85] Yuan-Fang Chou Jen-San Chen, Jeng-Yu Chen. On the natural frequencies and mode shapes of dragonfly wings. *Journal of Sound and Vibration*, 2007.

[86] Aaron G. Norris. *Investigation of Reinforced Membrane Wings for Use in Flapping Wing Micro Air Vehicles*. PhD thesis, Air Force Institute of Technology, .

[87] Ron Galant, James B. Skeath, Steve Paddock, David L. Lewis, and Sean B. Carroll. Expression pattern of a butterfly *achaete-scute* homolog reveals the homology of butterfly wing scales and insect sensory bristles. *Current Biology*, 1998.

[88] Michael H Dickinson and Michael S Tu. The function of dipteran flight muscle. *Comparative Biochemistry and Physiology Part A: Physiology*, 116(3):223–238, mar 1997.

[89] Mark Jankauski and IY Shen. Dynamic modeling of an insect wing subject to three-dimensional rotation. *International Journal of Micro Air Vehicles*, 6(4):231–251, 2014.

[90] J Gago, C Douthe, RE Coopman, PP Gallego, M Ribas-Carbo, J Flexas, J Escalona, and H Medrano. Uavs challenge to assess water stress for sustainable agriculture. *Agricultural Water Management*, 153:9–19, 2015.

[91] Lionel Heng, Dominik Honegger, Gim Hee Lee, Lorenz Meier, Petri Tanskanen, Friedrich Fraundorfer, and Marc Pollefeys. Autonomous visual mapping and exploration with a micro aerial vehicle. *Journal of Field Robotics*, 31(4):654–675, 2014.

[92] Alexander E MacDonald. A global profiling system for improved weather and climate prediction. *Bulletin of the American Meteorological Society*, 86(12):1747, 2005.

[93] Joel M Grasmeyer, Matthew T Keennon, et al. Development of the black widow micro air vehicle. *Progress in Astronautics and aeronautics*, 195:519–535, 2001.

[94] Sawyer B Fuller, Michael Karpelson, Andrea Censi, Kevin Y Ma, and Robert J Wood. Controlling free flight of a robotic fly using an onboard vision sensor inspired by insect ocelli. *Journal of The Royal Society Interface*, 11(97):20140281, 2014.

[95] Guido CHE de Croon, MA Groen, Christophe De Wagter, Bart Remes, Rick Ruijsink, and Bas W van Oudheusden. Design, aerodynamics and autonomy of the delfly. *Bioinspiration & biomimetics*, 7(2):025003, 2012.

[96] Matthew Keennon, Karl Klingebiel, Henry Won, and Alexander Andriukov. Development of the nano hummingbird: A tailless flapping wing micro air vehicle. In *AIAA aerospace sciences meeting*, pages 1–24. AIAA Reston, VA, 2012.

[97] John William Sutton Pringle. The gyroscopic mechanism of the halteres of diptera. *Philosophical Transactions of the Royal Society of London B: Biological Sciences*, 233(602):347–384, 1948.

[98] Michael H Dickinson. Haltere–mediated equilibrium reflexes of the fruit fly, drosophila melanogaster. *Philosophical Transactions of the Royal Society of London B: Biological Sciences*, 354(1385):903–916, 1999.

[99] Bradley H Dickerson, Zane N Aldworth, and Thomas L Daniel. Control of moth flight posture is mediated by wing mechanosensory feedback. *Journal of Experimental Biology*, 217(13):2301–2308, 2014.

[100] AL Eberle, BH Dickerson, PG Reinhall, and TL Daniel. A new twist on gyroscopic sensing: body rotations lead to torsion in flapping, flexing insect wings. *Journal of the Royal Society Interface*, 12(104):20141088, 2015.

[101] Bruno A Roccia, Sergio Preidikman, Julio C Massa, and Dean T Mook. Development of a kinematical model to study the aerodynamics of flapping-wings. *International Journal of Micro Air Vehicles*, 3(2):61–88, 2011.

[102] Christopher T Orlowski and Anouck R Girard. Modeling and simulation of nonlinear dynamics of flapping wing micro air vehicles. *AIAA journal*, 49(5):969–981, 2011.

[103] Satish K Chimakurthi, Carlos E S. Cesnik, and Bret K Stanford. Flapping-wing structural dynamics formulation based on a corotational shell finite element. *AIAA journal*, 49(1):128–142, 2011.

[104] Hao Wang, Yoshinobu Inada, and Hao Liu. A numerical analysis of inertial torques in the steering maneuvers of hovering drosophila. *JSME International Journal Series C*, 48(4):499–512, 2005.

[105] S Sponberg and TL Daniel. Abdicating power for control: a precision timing strategy to modulate function of flight power muscles. *Proceedings of the Royal Society of London B: Biological Sciences*, page rspb20121085, 2012.

[106] Robert C Michelson and Steven Reece. Update on flapping wing micro air vehicle research-ongoing work to develop a flapping wing, crawling entomopter. In *13th Bristol International RPV/UAV Systems Conference Proceedings, Bristol England*, volume 30, pages 30–1, 1998.

[107] Malcolm Burrows, Darron A Cullen, Marina Dorosenko, and Gregory P Sutton. Mantises exchange angular momentum between three rotating body parts to jump precisely to targets. *Current Biology*, 25(6):786–789, 2015.

[108] A Roland Ennos. A comparative study of the flight mechanism of diptera. *Journal of Experimental Biology*, 127(1):355–372, 1987.

[109] Mark Jankauski and IY Shen. Experimental studies of an inertial-elastic rotating wing in air and vacuum. *International Journal of Micro Air Vehicles*, 8(2):53–63, 2016.

Appendix A

EXTENDED DERIVATION OF EQUATION OF MOTION

The purpose of this appendix is to catalog the mathematical derivation of the Inertial-Elastic rotating wing model described in Chapter 2. For a detailed description of the terms outlined in this appendix, please refer to Chapter 2.

Rotating Reference Frame

Referring to Figure 2.1, the first finite rotation, α occurs about the $I, I^{'}$ axis and the second finite rotation, β, occurs about the $J^{'}, J^{''}$ axis. Thus, the angular velocity of the rotating coordinate frame can simply be described as

$$\vec{\Omega} = \dot{\alpha} I^{'} + \dot{\beta} J^{''} \tag{A.1}$$

The position vector $\vec{R}_n$ is drawn in the fully rotated coordinate frame (Fig. 2.2), which

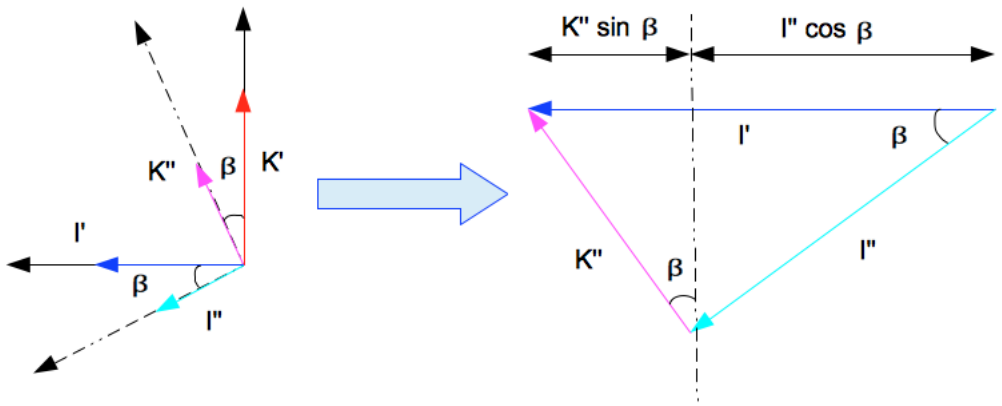

Figure A.1: Geometric sketch representing $I^{'}$ in fully rotated coordinate frame

necessitates $I^{'}$ be represented in the same frame. A straightforward geometric argument is made relating $I^{'}$ to the fully rotated frame. Figure A.1 shows the coordinate frame after the finite α rotation as viewed from along the $J^{'}, J^{''}$ axis. The solid lines indicate the coordinate frame that has been rotated once whereas the dashed lines show the fully rotated coordinate frame after the subsequent finite β rotation. Unit position vectors are superimposed on the axes for both frames. Clearly, the unit position vector $I^{'}$ can be represented mathematically in the fully rotated coordinate frame as $I^{'} = \cos\beta I^{''} + \sin\beta K^{''}$. This relationship can be substituted into Equation A.1 which results in the total angular velocity $\vec{\Omega}$ expressed in the fully rotated coordinate frame axes as

$$\vec{\Omega} = \dot{\alpha} cos\beta I^{''} + \dot{\beta} J^{''} + \dot{\alpha} sin\beta K^{''} \tag{A.2}$$

Lagrange's Equation

Lagrange's equation is employed on the kinetic and potential energy terms shown in Equations 2.6-2.7 using the modal response $q_k(t)$ as the generalized coordinate. Lagrangian mechanics is ideal for this formulation, as reaction forces and moments need not be determined explicitly as in Newtonian mechanics. In the general form, assuming no damping or non-conservative forces, Lagrange's equation is written as

$$\frac{d}{dt}(\frac{\partial T}{\partial \dot{q_k}}) - \frac{\partial T}{\partial q_k} + \frac{\partial V}{\partial q_k} = 0 \tag{A.3}$$

Due to the complexity of the kinetic energy T, the individual terms are expanded ($T = \sum_{i=1}^{6} T_i$) and processed through Lagrange's equation independently. The details of this process are cataloged in the following sections. The boxed result signifies a non-zero result to be included in the overall equation of motion governing the modal response.

$T_1 = \frac{1}{2}\int(\vec{\Omega}\times\vec{R}_n)\cdot(\vec{\Omega}\times\vec{R}_n)dm$

$$T_1 = \frac{1}{2}\int(\vec{\Omega}\times\vec{R}_n)\cdot(\vec{\Omega}\times\vec{R}_n)dm = \frac{1}{2}\vec{\Omega}\cdot\vec{I}_o\cdot\vec{\Omega} \tag{A.4}$$

$$\vec{I}_o = \int[(\vec{R}_n\cdot\vec{R}_n)\vec{I} - \vec{R}_n\vec{R}_n]dm \tag{A.5}$$

$$\frac{\partial T_1}{\partial q_k} = \frac{1}{2}\vec{\Omega}\cdot\frac{\partial\vec{I}_o}{\partial q_k}\cdot\vec{\Omega} \tag{A.6}$$

$$\frac{\partial\vec{I}_o}{\partial q_k} = (2\vec{R}_n\cdot\frac{\partial\vec{R}_n}{\partial q_k})\vec{I} - \frac{\partial\vec{R}_n}{\partial q_k}\vec{R}_n - \vec{R}_n\frac{\partial\vec{R}_n}{\partial q_k} \tag{A.7}$$

$$\frac{\partial\vec{R}_n}{\partial q_k} = \phi_k(\vec{r}_1)K'' \tag{A.8}$$

$$\int\vec{R}_n\cdot\frac{\partial\vec{R}_n}{\partial q_k}dm = \int W(\vec{r}_1,t)\phi_k(\vec{r}_1)dm = q_k(t) \tag{A.9}$$

$$\ldots = K''\int\phi_k(\vec{r}_1)r\hat{e}_r dm + K''\gamma\int\phi_k(\vec{r}_1)r\hat{e}_\theta dm + K''\int\phi_k(\vec{r}_1)\sum_{k=1}^{\infty}\phi_k(\vec{r}_1)q_k(t)dmK'' \tag{A.10}$$

$$\int\frac{\partial\vec{R}_n}{q_k}\vec{R}_n dm = \vec{a}_k K'' + \gamma K''\vec{b}_k + K''K''q_k(t) \tag{A.11}$$

$$\int\vec{R}_n\frac{\partial\vec{R}_n}{q_k}dm = \vec{a}_k K'' + \vec{b}_k\gamma K'' + K''K''q_k(t) \tag{A.12}$$

$$\frac{\partial\vec{I}_o}{\partial q_k} = 2q_k(t)(I''I'' + J''J'') - K''(\vec{a}_k + \gamma\vec{b}_k) - (\vec{a}_k + \gamma\vec{b}_k)K'' \tag{A.13}$$

$$\frac{\partial T_1}{\partial\dot{q}_k} = 0 \tag{A.14}$$

$$\boxed{\frac{\partial T_1}{\partial q_k} = (\dot{\alpha}^2 cos^2\beta + \dot{\beta}^2)q_k - (K''\cdot\vec{\Omega})[\vec{\Omega}\cdot(\vec{a}_k + \gamma\vec{b}_k)]} \tag{A.15}$$

$T_2 = \frac{1}{2}\int(\dot{\gamma}r\vec{e_\theta})\cdot(\dot{\gamma}r\vec{e_\theta})dm$

$$I_{zz} = \int(r^2\vec{e_\theta})dm \tag{A.16}$$

$$T_2 = \frac{1}{2}\dot{\gamma}^2 I_{zz} \tag{A.17}$$

$$\frac{\partial T_2}{\partial\dot{q}_k} = \frac{\partial T_2}{\partial q_k} = 0 \tag{A.18}$$

$T_3 = \frac{1}{2}\int[\dot{W}(\vec{r}_1,t)\vec{e_z}]\cdot[\dot{W}(\vec{R},t)\vec{e_z}]dm$

$$T_3 = \frac{1}{2}\int[\dot{W}(\vec{r}_1,t)\vec{e_z}]\cdot[\dot{W}(\vec{r}_1,t)\vec{e_z}]dm = \frac{1}{2}\sum_{k=1}^{\infty}\dot{q_k}^2(t) \tag{A.19}$$

$$\frac{\partial T_3}{\partial q_k} = 0 \tag{A.20}$$

$$\boxed{\frac{d}{dt}(\frac{\partial T_3}{\partial \dot{q_k}}) = \ddot{q_k}} \tag{A.21}$$

$T_4 = \int[\vec{\Omega}\times\vec{R}_n]\cdot(\dot{\gamma}r\vec{e_\theta})dm$

$$T_4 = \dot{\gamma}\int\vec{\Omega}\cdot(\vec{r}_1\times\vec{e_\theta}\,r dm) \tag{A.22}$$

$$T_4 = \dot{\gamma}\int\vec{\Omega}\cdot[(r\vec{e_r}+\gamma r\vec{e_\theta}+W(\vec{r}_1,t)\vec{e_z})\times\vec{e_\theta}]\,r\,dm \tag{A.23}$$

$$T_4 = \dot{\gamma}\vec{\Omega}\cdot\int(r^2\vec{e_z}-W(\vec{r}_1,t)\vec{e_r})dm \tag{A.24}$$

$$T_4 = \dot{\gamma}\vec{\Omega}\cdot[I_{zz}\vec{e_z}-\sum_{k=1}^{\infty}\vec{a_k}q_k(t)] \tag{A.25}$$

$$\frac{\partial T_4}{\partial \dot{q_k}} = 0 \tag{A.26}$$

$$\boxed{\frac{\partial T_4}{\partial q_k} = -\dot{\gamma}\vec{\Omega}\cdot\vec{a_k}} \tag{A.27}$$

$T_5 = \int (\Omega \times \vec{R}_n) \cdot \dot{W}(\vec{r}_1, t)\vec{e_z}\, dm$

$$T_5 = \vec{\Omega} \cdot \int \vec{R}_n \times \dot{W}(\vec{r}_1, t)\vec{e_z}\, dm \tag{A.28}$$

$$T_5 = \vec{\Omega} \cdot \int [r\vec{e_r} + \gamma r\vec{e_\theta} + W(\vec{r}_1, t)\vec{e_z}] \times \sum_{k=1}^{\infty} \phi_k(\vec{r}_1)\dot{q}_k(t)\vec{e}_z dm \tag{A.29}$$

$$T_5 = \vec{\Omega} \cdot \sum_{k=1}^{\infty} \dot{q}_k(t) \int (-r\phi_k(\vec{r}_1)\vec{e_\theta} + \gamma r\phi_k(\vec{r}_1)\vec{e_r}) dm \tag{A.30}$$

$$T_5 = \vec{\Omega} \cdot \sum_{k=1}^{\infty} (-\vec{b_k} + \gamma\vec{a}_k) \tag{A.31}$$

$$\frac{\partial T_5}{\partial q_k} = 0 \tag{A.32}$$

$$\frac{d}{dt}(\frac{\partial T_5}{\partial \dot{q}_k}) = \frac{d}{dt}[\vec{\Omega} \cdot (\gamma\vec{a_k} - \vec{b_k})] \tag{A.33}$$

$$\boxed{\frac{d}{dt}[\vec{\Omega} \cdot (\gamma\vec{a_k} - \vec{b_k})] = \dot{\vec{\Omega}} \cdot (\gamma\vec{a_k} - \vec{b_k}) + \dot{\gamma}\vec{\Omega} \cdot \vec{a}_k} \tag{A.34}$$

$T_6 = \int (\dot{\gamma} r\vec{e_\theta}) \cdot [\dot{W}(\vec{r}_1, t)\vec{e_z}] dm$

$$\frac{\partial T_6}{\partial \dot{q}_k} = \frac{\partial T_6}{\partial q_k} = 0 \tag{A.35}$$

$V = \frac{1}{2}\int_v S(W, W) dv$

$$V = \frac{1}{2}\int_v S(W, W) dv = \frac{1}{2}\sum_{k=1}^{\infty} q_k^2(t)\omega_k^2 \tag{A.36}$$

$$\boxed{\frac{\partial V}{\partial q_k} = \omega_k^2 q_k(t)} \tag{A.37}$$

Total Equation of Motion Governing the Modal Response

By rearranging the boxed terms outlined in the previous subsections, the total equation of motion governing $q_k(t)$ can be written as

$$\ddot{q}_k + [w_k^2 - (\dot{\alpha}^2 cos^2\beta + \dot{\beta}^2)]q_k = -\dot{\vec{\Omega}} \cdot (\gamma\vec{a_k} - \vec{b_k}) - (K'' \cdot \vec{\Omega})[\vec{\Omega} \cdot (\vec{a_k} + \gamma\vec{b_k})] - 2\dot{\gamma}\vec{\Omega} \cdot \vec{a_k} \tag{A.38}$$

Appendix B

APPROXIMATE ANALYTIC SOLUTION TO EQUATION OF MOTION

To determine the approximate solution to the the equation of motion described in Equation 2.14, the following approximations are employed:

$$w_k^2 - (\dot{\alpha^2} cos^2\beta + \dot{\beta}) \approx w_k^2 - 0.5(\alpha_0^2 + \beta_0^2)\omega^2 = \omega_{avg}^2 \tag{B.1}$$

$$cos\beta = J_0(\beta_0) + \sum_{n=2,even}^{\infty} 2J_n(\beta_0)cos(n\omega_d t) \approx J_0(\beta_0) \tag{B.2}$$

$$sin\beta = \sum_{n=1,odd}^{\infty} 2J_n(\beta_0)sin(n\omega_d t) \approx 2J_1(\beta_0)sin\omega_d t \tag{B.3}$$

Next, $\vec{a}_k$, $\vec{b}_k$, $\vec{\Omega}$ and $dot\vec{\Omega}$ are expanded to:

$$\vec{a}_k = [A_I, A_J, 0] \tag{B.4}$$

$$\vec{b}_k = [B_I, B_J, 0] \tag{B.5}$$

$$\vec{\Omega} = [\dot{\alpha}cos\beta, \dot{\beta}, \dot{\alpha}sin\beta] \tag{B.6}$$

$$\dot{\vec{\Omega}} = [\ddot{\alpha}cos\beta - \dot{\alpha}\dot{\beta}sin\beta, \ddot{\beta}, \ddot{\alpha}sin\beta + \dot{\alpha}\dot{\beta}cos\beta] \tag{B.7}$$

Given the approximations above, Equation 2.14 can be solved individually for the Coriolis, Euler and centrifugal forces. Due to the linearity, each response may be summed together to yield the entire response. The details for the solution to each excitation term is summarized as follows. Several constants are defined within each subsection to simplify the expressions.

Centrifugal Force

$$E_1 = -(K^{''} \cdot \vec{\Omega})\,[\vec{\Omega} \cdot (\vec{a_k} + \gamma \vec{b_k})] \tag{B.8}$$

$$E_1 = -(A_I + \gamma B_I)\dot{\alpha}^2 cos\beta sin\beta - (A_J + \gamma B_J)\dot{\alpha}\dot{\beta} sin\beta \tag{B.9}$$

$$T_1 = -A_I \dot{\alpha}^2 cos\beta sin\beta \tag{B.10}$$

$$T_2 = -\gamma B_I \dot{\alpha}^2 cos\beta sin\beta \tag{B.11}$$

$$T_3 = -A_J \dot{\alpha}\dot{\beta} sin\beta \tag{B.12}$$

$$T_4 = -\gamma B_J \dot{\alpha}\dot{\beta} sin\beta \tag{B.13}$$

$$T_1 = -A_I \alpha_0^2 \omega^2 cos^2(\omega t) cos\beta sin\beta \tag{B.14}$$

$$T_1 = -A_I \alpha_0^2 \omega^2 cos^2(\omega t)[J_0(\beta_0)][2J_1(\beta_0) sin\omega t] \tag{B.15}$$

$$T_1 = -2A_I \alpha_0^2 \omega^2 J_0(\beta_0) J_1(\beta_0) cos^2(\omega t) sin(\omega t) \tag{B.16}$$

$$C_1 := 2A_I \alpha_0^2 \omega^2 J_0(\beta_0) J_1(\beta_0) \tag{B.17}$$

$$T_1 = -C_1 cos^2(\omega t) sin(\omega t) \tag{B.18}$$

$$\ddot{q_k} + \omega_{ave}^2 q_k = T_1 = -\frac{1}{4} C_1 [sin(\omega t) + sin(3\omega t)] \tag{B.19}$$

$$\boxed{q_1 = (\frac{C_1}{4}) \frac{[\omega sin(\omega_{avg} t) - \omega_{avg} sin(\omega t)]}{\omega_{avg}^3 - \omega_{avg}\,\omega^2} - (\frac{C_1}{4}) \frac{[\omega_{avg} sin(3\omega t) - 3\omega sin(\omega_{avg} t)]}{\omega_{avg}^3 - 9\omega_{avg}\,\omega^2}} \tag{B.20}$$

$$T_2 = -\gamma B_I \dot{\alpha}^2 cos\beta sin\beta \tag{B.21}$$

$$T_2 = -2B_I \gamma_0 \alpha_0^2 \omega^2 J_0(\beta_0) J_1(\beta_0) sin^2(\omega t) cos^2(\omega t) \tag{B.22}$$

$$C_2 := 2B_I \gamma_0 \alpha_0^2 \omega^2 J_0(\beta_0) J_1(\beta_0) \tag{B.23}$$

$$T_2 = -\frac{1}{8} C_2 [1 - cos(4\omega t)] \tag{B.24}$$

$$\ddot{q_k} + \omega_{ave}^2 q_k = T_2 = -\frac{1}{8} C_2 [1 - cos(4\omega t)] \tag{B.25}$$

$$\boxed{q_2 = (\frac{C_2}{8}) \frac{[cos(\omega_{avg} t) - 1]}{\omega_{avg}^2} + (\frac{C_2}{8}) \frac{[cos(4\omega t) - cos(\omega_{avg} t)]}{\omega_{avg}^2 - 16\omega^2}} \tag{B.26}$$

$$\tag{B.27}$$

$$T_3 = -A_J \dot{\alpha} \dot{\beta} sin\beta \tag{B.28}$$

$$C_3 := 2A_J \alpha_0 \beta_0 \omega^2 J_1(\beta_0) \tag{B.29}$$

$$T_3 = -\frac{1}{4} C_3 [sin(\omega t) + sin(3\omega t)] \tag{B.30}$$

$$\ddot{q_k} + \omega_{ave}^2 q_k = T3 = -\frac{1}{4} C_3 [sin(\omega t) + sin(3\omega t)] \tag{B.31}$$

$$\boxed{q_3 = (\frac{C_3}{4}) \frac{[\omega sin(\omega_{avg} t) - \omega_{avg} sin(\omega t)]}{\omega_{avg}^3 - \omega_{avg}\, \omega^2} - (\frac{C_3}{4}) \frac{[\omega_{avg} sin(3\omega t) - 3\omega sin(\omega_{avg} t)]}{\omega_{avg}^3 - 9\omega_{avg}\, \omega^2}} \tag{B.32}$$

$$T_4 = -\gamma B_J \dot{\alpha} \dot{\beta} sin\beta \tag{B.33}$$

$$C_4 := 2B_J \gamma_0 \alpha_0 \beta_0 \omega^2 J_1(\beta_0) \tag{B.34}$$

$$T_4 = -\frac{1}{8} C_4 [1 - cos(4\omega t)] \tag{B.35}$$

$$\ddot{q_k} + \omega_{ave}^2 q_k = T4 = -\frac{1}{8} C_4 [1 - cos(4\omega t)] \tag{B.36}$$

$$\boxed{q_4 = (\frac{C_4}{8}) \frac{[cos(\omega_{avg} t) - 1]}{\omega_{avg}^2} + (\frac{C_4}{8}) \frac{[cos(4\omega t) - cos(\omega_{avg} t)]}{\omega_{avg}^2 - 16\omega^2}} \tag{B.37}$$

$$\boxed{q_{k,centrifugal} = \sum_{n=1}^{4} q_n} \tag{B.38}$$

Coriolis Force

$$E_2 = -2\dot{\gamma}\vec{\Omega} \cdot \vec{a_k} \tag{B.39}$$

$$E_2 = -2\dot{\gamma}(A_I\dot{\alpha}cos\beta + A_J\dot{\beta}) \tag{B.40}$$

$$E_2 = -2A_I\alpha_0\gamma_0\omega^2cos^2(\omega t)cos\beta - 2A_J\beta_0\gamma_0\omega^2cos^2(\omega t) \tag{B.41}$$

$$E_2 = -2A_IJ_0(\beta_0)\alpha_0\gamma_0\omega^2cos^2(\omega t) - 2A_J\beta_0\gamma_0\omega^2cos^2(\omega t) \tag{B.42}$$

$$C_1 = A_I\alpha_0\gamma_0\omega^2J_0(\beta_0) \tag{B.43}$$

$$C_2 = A_J\beta_0\gamma_0\omega^2 \tag{B.44}$$

$$T_1 = -C_1 \tag{B.45}$$

$$T_2 = -C_1cos(2\omega t) \tag{B.46}$$

$$T_3 = -C_2 \tag{B.47}$$

$$T_4 = -C_2cos(2\omega t) \tag{B.48}$$

$$\ddot{q_n} + \omega_{ave}^2 q_n = T_n \tag{B.49}$$

$$\boxed{q_1 = C_1\frac{cos(\omega_{avg}t) - 1}{\omega_{avg}^2}} \tag{B.50}$$

$$\boxed{q_2 = C_1\frac{cos(\omega_{avg}t) - cos(2\omega t)}{\omega_{avg}^2 - 4\omega^2}} \tag{B.51}$$

$$\boxed{q_3 = C_2\frac{cos(\omega_{avg}t) - 1}{\omega_{avg}^2}} \tag{B.52}$$

$$\boxed{q_4 = C_2\frac{cos(\omega_{avg}t) - cos(2\omega t)}{\omega_{avg}^2 - 4\omega^2}} \tag{B.53}$$

$$\boxed{q_{k,Coriolis} = \sum_{n=1}^{4} q_n} \tag{B.54}$$

Euler Force

$$E_3 = -\dot{\vec{\Omega}} \cdot (\gamma \vec{a_k} - \vec{b_k}) \tag{B.55}$$

$$E_3 = -[\ddot{\alpha}cos\beta - \dot{\alpha}\dot{\beta}sin\beta, \ddot{\beta}, \ddot{\alpha}sin\beta + \dot{\alpha}\dot{\beta}cos\beta] \cdot [\gamma A_I - B_I, \gamma A_J - B_J, 0] \tag{B.56}$$

$$E_3 = (\gamma A_I - B_I)(\dot{\alpha}\dot{\beta}sin\beta - \ddot{\alpha}cos\beta) + (\gamma A_J - B_J)(-\ddot{\beta}) \tag{B.57}$$

$$C_1 := A_I \gamma_0 \alpha_0 \beta_0 \omega^2 J_1(\beta_0) \tag{B.58}$$

$$T_1 = \frac{1}{4} C_1 [1 - cos(4\omega t)] \tag{B.59}$$

$$\boxed{q_1 = \frac{C_1}{2\omega_{avg}^2} sin^2(\frac{\omega_{avg} t}{2}) + \frac{C_1}{4(\omega_{avg}^2 - 16\omega^2)} [cos(\omega_{avg} t) - cos(4\omega t)]} \tag{B.60}$$

$$C_2 := A_I \gamma_0 \alpha_0 \omega^2 J_0(\beta_0) \tag{B.61}$$

$$T_2 = \frac{1}{4} C_1 [1 - cos(2\omega t)] \tag{B.62}$$

$$\boxed{q_2 = \frac{C_2}{\omega_{avg}^2} sin^2(\frac{\omega_{avg} t}{2}) + \frac{C_2}{2(\omega_{avg}^2 - 4\omega^2)} [cos(\omega_{avg} t) - cos(2\omega t)]} \tag{B.63}$$

$$C_3 = B_I \alpha_0 \beta_0 \omega^2 J_1(\beta_0) \tag{B.64}$$

$$T_3 = -\frac{1}{2} C_3 [sin(\omega t) + sin(3\omega t)] \tag{B.65}$$

$$q_3 = \frac{C_3}{2(\omega_{avg}^3 - \omega_{avg}\omega^2)} [\omega sin(\omega_{avg} t) - \omega_{avg} sin(\omega t)] - \frac{C_3}{2(\omega_{avg}^3 - 9\omega_{avg}\omega^2)} [\omega_{avg} sin(3\omega t) - 3\omega sin(\omega_{avg} t)] \tag{B.66}$$

$$C_4 = B_I \alpha_0 \omega^2 J_0(\beta_0) \tag{B.67}$$

$$T_4 = -C_4 sin(\omega t) \tag{B.68}$$

$$\boxed{q_4 = \frac{C_4}{\omega_{avg}^3 - \omega_{avg}\omega^2}[\omega sin(\omega_{avg} t) - \omega_{avg} sin(\omega t)]} \tag{B.69}$$

$$C_5 = A_J \beta_0 \gamma_0 \omega^2 \tag{B.70}$$

$$T_5 = \frac{1}{2} C_5 [1 - cos(2\omega t)] \tag{B.71}$$

$$\boxed{q_5 = \frac{C_5}{\omega_{avg}^2} sin^2(\frac{\omega_{avg} t}{2}) + \frac{C_5}{2(\omega_{avg}^2 - 4\omega^2)}[cos(\omega_{avg} t) - cos(2\omega t)]} \tag{B.72}$$

$$\tag{B.73}$$

$$C_6 = B_J \beta_0 \omega^2 \tag{B.74}$$

$$T_6 = -C_6 sin(\omega t) \tag{B.75}$$

$$\boxed{q_6 = \frac{C_6}{\omega_{avg}^3 - \omega_{avg}\omega^2}[\omega sin(\omega_{avg} t) - \omega_{avg} sin(\omega t)]} \tag{B.76}$$

Appendix C

WING MODEL MATLAB CODE

```
1  %Mark Jankauski%
2  clear all; clc;close all;
3  tic
4
5  %% SUMMARY %%
6
7  % The purpose of this script is to demonstrate how to numerically solve the
8  % equation of motion governing the modal response of the wing.  Wing
9  % geometry, mode shapes, and natural frequencies are determined using
10 % Abaqus FEA.  The user inputs are rotation profiles and total time.  ...
       The default
11 % rotation is sinusoidal, but can be changed by the user should other
12 % rotations be of interest.  The script is heavily commented so the user
13 % can change parameters as necessary.
14
15 % This example is for the aluminum triangular wing used for the
16 % experimental validation.  Three vibration modes are considered, but could
17 % be extended to include more modes if necessary.
18
19 % The output of this script is the strain at the selected point near the
20 % wing root as a function of time, and the magnitude of the strain as a
21 % function of frequency.
22
23 % The most common error for a user unfamiliar with the script is indexing.
24 % Be sure that the index numbers in the script correspond to the correct
```

```
25 % columns in the .inp and .rpt files generated using FEA
26
27
28 %% INPUT PARAMETERS%%
29
30 % In this section, the amplitudes and frequencies of the rotation profiles
31 % are input.  The script assumes sinusoidal rotations.  This is also where
32 % modal damping is considered.  Lastly, the total length of the simulation
33 % and the time step is input.
34
35 N=3;                    %Enter the number of modes considered here%
36
37 %The value for 'node' corresponds to the node number that most closely
38 %matches the physical location where the strain is being evaluated
39 node=19006;
40
41 %Frequency Parameters%
42 w_a=5;                 %Alpha Rotation Freq, Hz%
43 w_b=5;                 %Beta Rotataion Freq, Hz%
44 w_g=5;                 %Gamma Rotation Freq, Hz%
45
46 %Rotation parameters%
47
48 %For the experimental set-up, rotation amplitudes are measured in quarter
49 %counts (qc).  The number of qc/revolution is specific to the encoder.  For
50 %the encoder used, there are 2000 qc/ revolution. Inputs subscripted ...
       with a
51 %_ph correspond to the phase of the sinusoidal rotation.
52
53 A=250;                  %Amplitude of roll, main rotation, qc%
54 A_ph=0;                 %Phase shift of roll rotation, rad%
55 B=200;                  %Amplitude or pitch, secondary rotation, qc%
56 B_ph=0;                 %Phase shift of pitch rotation, rad%
```

```
57 G=0;                    %Amplitude of yaw, tertiary rotation, qc%
58 G_ph=0;                 %Phase shift of yaw rotation, rad%
59
60 %Time Parameters
61 t0=0;                   %The starting time of the simulation
62 tf=2;                   %The final time of the simulation
63 h=0.001;                %The time step used for the simulation
64 td=t0:h:tf;             %Creates a linear array of time for the simulation%
65
66 %Natural frequencies%
67
68 %The natural frequencies (in Hz) are input here, in ascending order.  These
69 %are determined via Abaqus FEA and are input manually.  Three modes are
70 %considered, corresponding to three natural frequencies.
71
72 w_n=[20 146 175.56];
73
74 %Modal damping
75
76 %The modal damping ratios are input here.  The damping ratio may be a
77 %scalar quantity if all modes are equally damped.  To have non-uniform
78 %damping ratios, input each damping ratio in the array.  The example is
79 %currently undamped, for zed=0.
80
81 zed=[0 0 0];
82
83 %Unit conversions
84
85 %Natural frequencies and driving frequencies are converted from Hz to
86 %rad/sec
87
88 w_a=w_a*2*pi;
89 w_b=w_b*2*pi;
```

```
90  w_g=w_g*2*pi;
91  w_n=w_n*2*pi;
92
93  %The rotation amplitudes are converted from qc to radians
94  A=A*(2*pi)/(2000); B=B*(2*pi)/(2000); G=G*(2*pi)/(2000);
95
96  %The total modal damping term is evaluated
97  damp=2*zed.*w_n;
98
99  %% DATA IMPORT%
100
101 % The necessary data from the FEM model is input here.  The files are
102 % summarized as follows
103
104 % Imports the geometry of the wing in x-y-z coordinates.  This data is
105 % found in the .inp file generated when submitting a job to Abaqus CAE.
106 % The .inp is converted to a .txt, and all extraneous information in the
107 % file is deleted
108 Geo=load('Wing_Geometry.txt');
109
110 % Imports the nodal mass of the wing.  To determine the nodal mass in FEA,
111 % all degrees of freedom are constrained and a unit load is applied in the
112 % downward z-direction, such that the reaction force at each node
113 % corresponds to the nodal mass.  An .rpt file is then generated reporting
114 % the reaction force at each node.  This .rpt file is converted to a .txt,
115 % and all information except the node number and z-component of the
116 % reaction force is deleted
117 Node_Mass=load('Nodal_Mass.txt');
118
119 %Imports the x-y-z coordinates of the first three vibration modes of the
120 %wing.  The x,y coordinates are treated as zero, as in-plane ...
        deformation is
121 %neglected.  It is important to normalize the mode shapes with respect to
```

```
122 %the mass matrix to remain consistent with formulation.  The Mode files are
123 %generated by creating a .rpt file after solving the mode shapes in Abaqus.
124 %Exraneous information is deleted, leaving the modal coordinates
125
126 Mode_1=load('Mode1.txt');
127 Mode_2=load('Mode2.txt');
128 Mode_3=load('Mode3.txt');
129
130
131
132 %% DATA INDEXING%
133
134 %In this section, the data from the Abaqus report files are indexed such
135 %that they can easily be used in the script.  Any translation or rotation
136 %of the geometry can be applied in this section.  No rotation is considered
137 %here, as the CAE model is built in the x-y plane
138
139 X_cor=Geo(:,2); Y_cor=Geo(:,3); Z_cor=Geo(:,4); %Creates x,y,z arrays ...
       from imported geometry
140
141 X_shift=0;          %Non-zero input shifts the wing in the x direction
142 Y_shift=0;          %Non-zero input shifts the wing in the y direction
143
144 %Adds the x,y shifts to the total geometry
145 X_cor=X_cor+X_shift;
146 Y_cor=Y_cor+Y_shift;
147
148 %Indexes the nodal mass from the imported data.  If the nodal mass was
149 %found correctly, the absolute value is unnecessary
150 Node_Mass=abs(Node_Mass(:,2));
151
152 %Initialize an empty matrix for mode shape data%
153 Mode=zeros(length(Geo),N);
```

```
154
155 %Assembles mode shape data into a single Modal matrix%
156 Mode(:,1)=Mode_1(:,2); Mode(:,2)=Mode_2(:,2); Mode(:,3)=Mode_3(:,2);
157
158
159 %% INDEX STRAINS
160
161 % The modal strain evaluated at the location of interest is indexed here.
162 % The '5' index corresponds to the strain in the y-direction.  By changing
163 % this index, you can evaluate the x-component of normal strain or shear
164 % strain.  The index number depends on how the .rpt files were generated.
165
166 ST1=Mode_1(node,5);
167 ST2=Mode_2(node,5);
168 ST3=Mode_3(node,5);
169
170
171 %% PLOT MODE SHAPES
172
173 %As a sanity check, this line of code plots the wing geometry in 3D space.
174 %This helps visualize that any translations or rotations of the CAE model
175 %were done correctly.
176
177  tri=delaunay (X_cor,Y_cor);
178
179     figure()
180     trisurf ( tri, X_cor, Y_cor, Z_cor );
181     xlabel('x')
182     ylabel('y')
183     zlabel('z')
184     title('Base Wing Geometry')
185     xlim([-0.11 0.11])
186     ylim([0 0.15])
```

```
187     view(150,24)
188
189
190 %% INERTIAL FORCE CENTER CALCULATIONS%
191
192 %This section calculates A_k and B_k for each mode shape.  A_k corresponds
193 %to a vector from the fixed point of rotation to the inertial force center
194 %of the k^th mode, and B_k corresponds to a 90 degree counter-clockwise
195 %rotation from A_k.  See the model formulation for more details.
196
197 A_k=zeros(N,3); %Initialize 3xN A_k matrix
198 B_k=zeros(N,3); %Initialize 3xN B_k matrix
199
200 %Create A_k vector matrix%
201 for i=1:N
202     A_k(i,1)=sum(Mode(:,i).*X_cor.*Node_Mass); %Populates I'' field
203     A_k(i,2)=sum(Mode(:,i).*Y_cor.*Node_Mass); %Populates J'' field
204 end
205
206 %Create B_k vector matrix
207 for i=1:N
208     B_k(i,1)=sum(Mode(:,i).*-Y_cor.*Node_Mass); %Populates I'' field
209     B_k(i,2)=sum(Mode(:,i).*X_cor.*Node_Mass); %Populates J'' field
210 end
211
212
213 %% ROTATION PARAMETER CALCULATIONS
214
215 %The rotation profiles are calculated here from the input rotation
216 %amplitudes and frequencies.  The time derivatives are calculated
217 %analytically.  Currently, all rotations are assumed sinusoidal. The user
218 %change the form of the driving rotations if desired.
219
```

```
220 %Driving roll function and its time derivatives%
221
222 Alpha=A*sin(w_a*td+A_ph);
223 Alpha_D=A*w_a*(cos(w_a*td+A_ph));       %First time derivative of roll
224 Alpha_DD=-A*w_a^2*(sin(w_a*td+A_ph));   %Second time derivative of roll
225
226 %Driving pitch function and its time derivatives%
227 Beta=B*sin(w_b*td+B_ph);
228 Beta_D=B*w_b*cos(w_b*td+B_ph);          %First time derivative of pitch
229 Beta_DD=-B*w_b^2*sin(w_b*td+B_ph);      %Second time derivative of pitch
230
231 %Driving yaw function and its time derivatives%
232 Gamma=G*sin(w_g*td+G_ph);
233 Gamma_D=G*w_g*cos(w_g*td+G_ph);         %First time derivative of yaw
234 Gamma_DD=-G*w_g^2*sin(w_g*td+G_ph);     %Second time derivative of yaw
235
236 %Instantaneous angular velocity and acceleration vectors are calculated
237 %from the rotation trajectories.  These expressions are valid even if a
238 %non-sinusoidal rotation is considered.
239
240 W_a=[(Alpha_D.*cos(Beta))',(Beta_D)',(Alpha_D.*sin(Beta))'];
241 W_a_d=[(Alpha_DD.*cos(Beta)-Alpha_D.*Beta_D.*sin(Beta))',...
242       (Beta_DD)',(Alpha_DD.*sin(Beta)+Alpha_D.*Beta_D.*cos(Beta))'];
243
244 %% TIME VARYING STIFFNESS%
245
246 %The time varying stiffnesses for all natural frequencies are calculated
247 %here%
248
249 Stiffness=zeros(N,length(td)); %Initialize time-varying stiffness matrix%
250
251 %Calculates the time-varying stiffness for each mode considered
252 for i=1:N
```

```
253     Stiffness(i,:)=w_n(i)^2-((Alpha_D.^2).*(cos(Beta).^2)+(Beta_D.^2));
254 end
255
256
257 %% EXCITATION PARAMETERS%
258
259 %The Euler, Coriolis, Centrifugal and total excitations are calculated
260 %here.  See the model formulation for a detailed mathematical description
261 %of each of the excitation terms.
262
263 %Initialize excitation matrices%
264 Euler_Force=zeros(N,length(td));
265 Centrifugal_Force=zeros(N,length(td));
266 Coriolis_Force=zeros(N,length(td));
267
268 %Calculate the excitations for each mode shape%
269 for i=1:N %indexing through the number of mode shapes
270
271     for j=1:length(td) %indexing through the time span
272     Euler_Force(i,j)=-dot(W_a_d(j,:),(Gamma(j)*A_k(i,:)-B_k(i,:))); ...
            %Euler Force calculation
273     Centrifugal_Force(i,j)=-dot([0,0,1],W_a(j,:))*dot(W_a(j,:),(A_k(i,:)...
274     +Gamma(j)*B_k(i,:))); %Centrifugal force calculation
275     Coriolis_Force(i,j)=-2*Gamma_D(j)*dot(W_a(j,:),A_k(i,:)); %Coriolis ...
            Force calculation
276     end
277 end
278
279 Total_Excitation=Euler_Force+Centrifugal_Force+Coriolis_Force; %Sums ...
       all components of the excitation%
280
281 %% SOLVE FOR RESPONSES
282
```

```
283 %This section is used to calculate each modal response seperately using the
284 %Wing_Func.  For more details on the Wing_Func, open the function file.
285 [T1 q1]=ode45(@(t,y) ...
       Wing_Func(t,y,td,Total_Excitation(1,:),Stiffness(1,:),damp(1)),td,[0,0]);
286 [T2 q2]=ode45(@(t,y) ...
       Wing_Func(t,y,td,Total_Excitation(2,:),Stiffness(2,:),damp(2)),td,[0,0]);
287 [T3 q3]=ode45(@(t,y) ...
       Wing_Func(t,y,td,Total_Excitation(3,:),Stiffness(3,:),damp(3)),td,[0,0]);
288
289 %The modal responses are multiplied by the modal strain to give a physical
290 %strain value
291 q1=q1(:,1).*ST1;
292 q2=q2(:,1).*ST2;
293 q3=q3(:,1).*ST3;
294
295 %Each of the physical strains are summed together to give the total
296 %physical strain (again, considering 3 mode shapes)
297 Q=q1+q2+q3;
298
299 %The physical strain is multiplied by 10^6 to convert strain to microstrain
300 Q=Q*10^6;
301
302 %This portion of the script takes the FFT and determines the magnitude of
303 %the strain (in microstrain) as a function of frequency
304
305 h=T1(2)-T1(1);          %Determines time step from simulation time
306 Fs = h^-1;              % Sampling frequency
307 T = 1/Fs;               % Sample time
308 L = length(T1);         % Length of signal
309 t = (0:L-1)*T;
310
311 NFFT = 2^nextpow2(L);               % Next power of 2 from length of y
312 Y = fft(Q,NFFT)/L;
```

```
313 f = Fs/2*linspace(0,1,NFFT/2+1);    %Sets up the array of frequencies
314 Y=2*abs(Y(1:NFFT/2+1));             %Determines the magnitude of the strain
315
316
317 %Plots the magnitude of the microstrain as a function of frequency in Hz
318 figure()
319 plot(f,Y)
320 title('FFT of Strain (Theory)')
321 xlabel('Frequency (Hz)')
322 ylabel('|Microstrain|')
323 xlim([0 20])
324
325 %Plots the microstrain versus time signal
326 figure()
327 plot(T1,Q)
328 xlabel('Time (sec)')
329 ylabel('Strain (Microstrain)')
330 title('Strain vs. Time')
331
332 toc
```

Appendix D

LINEARIZATION OF AERO/INERTIAL MODEL

This appendix is documents the linearization of force and moment terms about operating point $(\gamma, \dot{\gamma}, \ddot{\gamma}) = (0, 0, 0)$ via a Taylor Series Expansion. Second order terms (those of γ^2) are neglected. We begin by showing angular velocity $\vec{\Omega}$ and angular acceleration $\dot{\vec{\Omega}}$ and their respective derivatives in $\gamma^{(i)}$ evaluated at $(\gamma, \dot{\gamma}, \ddot{\gamma}) = (0, 0, 0)$.

$$\vec{\Omega}|_{\gamma,\dot{\gamma}=0} = \dot{\alpha}\cos\beta\,\hat{e}_x + \dot{\beta}\,\hat{e}_y + \dot{\alpha}\sin\beta\,\hat{e}_z \tag{D.1}$$

$$\frac{\partial\vec{\Omega}}{\partial\gamma}|_{\gamma,\dot{\gamma}=0} = \dot{\beta}\,\hat{e}_x + -\dot{\alpha}\cos\beta\,\hat{e}_y \tag{D.2}$$

$$\frac{\partial\vec{\Omega}}{\partial\dot{\gamma}}|_{\gamma,\dot{\gamma}=0} = \hat{e}_z \tag{D.3}$$

$$\dot{\vec{\Omega}}|_{\gamma,\dot{\gamma},\ddot{\gamma}=0} = (\ddot{\alpha}\cos\beta - \dot{\alpha}\dot{\beta}\sin\beta)\hat{e}_x + \ddot{\beta}\,\hat{e}_y + (\ddot{\alpha}\sin\beta + \dot{\alpha}\dot{\beta}\cos\beta)\hat{e}_z \tag{D.4}$$

$$\frac{\partial\dot{\vec{\Omega}}}{\partial\gamma}|_{\gamma,\dot{\gamma},\ddot{\gamma}=0} = \ddot{\beta}\,\hat{e}_x + (-\ddot{\alpha}\cos\beta + \dot{\alpha}\dot{\beta}\sin\beta)\hat{e}_y \tag{D.5}$$

$$\frac{\partial\dot{\vec{\Omega}}}{\partial\dot{\gamma}}|_{\gamma,\dot{\gamma},\ddot{\gamma}=0} = \dot{\beta}\,\hat{e}_x - \dot{\alpha}\cos\beta\hat{e}_y \tag{D.6}$$

$$\frac{\partial\dot{\vec{\Omega}}}{\partial\ddot{\gamma}}|_{\gamma,\dot{\gamma},\ddot{\gamma}=0} = \hat{e}_z \tag{D.7}$$

Next, the rotation matrix transpose $\mathbf{R}^T$ and its derivative in γ evaluated at $(\gamma, \dot{\gamma}, \ddot{\gamma}) = (0, 0, 0)$ are

$$\mathbf{R}^T|_{\gamma=0} = \begin{bmatrix} \cos\beta & 0 & \sin\beta \\ \sin\alpha\sin\beta & \cos\alpha & -\cos\beta\sin\alpha \\ -\cos\alpha\sin\beta & \sin\alpha & \cos\alpha\cos\beta \end{bmatrix} \tag{D.8}$$

$$\frac{\partial \mathbf{R}^T}{\partial \gamma}|_{\gamma=0} = \begin{bmatrix} 0 & -\cos\beta & 0 \\ \cos\alpha & -\sin\alpha\sin\beta & 0 \\ -\sin\alpha & \cos\alpha\sin\beta & 0 \end{bmatrix} \tag{D.9}$$

Note that the rotation matrix $\mathbf{R}$ does not have derivatives in $\dot{\gamma}$ or $\ddot{\gamma}$. With these definitions in place, we can begin evaluating physical terms. We begin with the angular momentum $\vec{H}_0$ and the inertial moments $\vec{M}_0$ linearized about $(\gamma, \dot{\gamma}, \ddot{\gamma}) = (0, 0, 0)$.

$$\vec{H}_0 \approx \mathbf{R}^T \mathbf{I}_0 \vec{\Omega}|_{\gamma,\dot{\gamma}=0} + \left[\sum_{i=1}^{2} \left(\frac{\partial \mathbf{R}^T}{\partial \gamma^{(i)}} \mathbf{I}_0 \vec{\Omega} + \mathbf{R}^T \mathbf{I}_0 \frac{\partial \vec{\Omega}}{\partial \gamma^{(i)}} \right) \gamma^{(i)} \right]_{\gamma=\dot{\gamma}=0} \tag{D.10}$$

$$\begin{aligned} \vec{M}_0 \approx \mathbf{R}^T & (\vec{\Omega} \times \mathbf{I}_0 \vec{\Omega} + \mathbf{I}_0 \dot{\vec{\Omega}})_{\gamma,\dot{\gamma},\ddot{\gamma}=0} \\ & + \mathbf{R}^T \left[\sum_{i=1}^{3} \left(\frac{\partial \vec{\Omega}}{\partial \gamma^{(i)}} \times \mathbf{I}_0 \vec{\Omega} + \vec{\Omega} \times \mathbf{I}_0 \frac{\partial \vec{\Omega}}{\partial \gamma^{(i)}} + \mathbf{I}_0 \frac{\partial \dot{\vec{\Omega}}}{\partial \gamma^{(i)}} \right) \gamma^{(i)} \right]_{\gamma,\dot{\gamma},\ddot{\gamma}=0} \\ & + \left[\frac{\partial \mathbf{R}^T}{\partial \gamma} (\vec{\Omega} \times \mathbf{I}_0 \vec{\Omega} + \mathbf{I}_0 \dot{\vec{\Omega}})\, \gamma \right]_{\gamma,\dot{\gamma},\ddot{\gamma}=0} \end{aligned} \tag{D.11}$$

Next, we can linearize the aerodynamic moments and forces. As mentioned in the body of the paper, the lift force F_L and drag force F_D are linearized by

$$\begin{aligned} F_{[\cdot]} \approx \frac{1}{2}\rho_f & \int_0^R r^2 c(r) dr \\ & * \left[\mathbf{R}^T C_{[\cdot]} V^2 + \frac{\partial \mathbf{R}^T}{\partial \gamma} C_{[\cdot]} V^2 \gamma + \mathbf{R}^T \right]_{\gamma,\dot{\gamma}=0} \\ & + \left[\sum_{i=1}^{2} \underbrace{\left(2C_{[\cdot]} \left(v_x \frac{\partial v_x}{\partial \gamma^{(i)}} + v_z \frac{\partial v_z}{\partial \gamma^{(i)}} \right) + \frac{\partial C_{[\cdot]}}{\partial AoA} \left(\frac{\partial v_z}{\partial \gamma^{(i)}} v_x - \frac{\partial v_x}{\partial \gamma^{(i)}} v_z \right) \right) \gamma^{(i)}}_{\frac{\partial C_{[\cdot]} V^2}{\partial \gamma^{(i)}}} \right]_{\gamma,\dot{\gamma}=0} \end{aligned} \tag{D.12}$$

where $[\cdot]$ is a placeholder for lift or drag. The normal and axial forces are then

$$\vec{F}_A \approx \frac{1}{2}\rho_f \int_0^R r^2 c(r) dr *$$
$$\left[\mathbf{R}^T \sum_{i=1}^{2} \left(\frac{\partial C_D V^2}{\partial \gamma^{(i)}} \cos AoA + C_D V^2 \frac{\partial \cos AoA}{\partial \gamma^{(i)}} - \frac{\partial C_L V^2}{\partial \gamma^{(i)}} \sin AoA - C_L V^2 \frac{\partial \sin AoA}{\partial \gamma^{(i)}} \right) \gamma^{(i)} \right]_0$$
$$+ \frac{1}{2}\rho_f \int_0^R r^2 c(r) dr \left[\frac{\partial \mathbf{R}^T}{\partial \gamma} \left(F_D \cos AoA - F_L \sin A0A \right) \right]_{\gamma, \dot{\gamma}=0} \gamma[-\hat{e}_x]$$
$$+ \frac{1}{2}\rho_f \int_0^R r^2 c(r) dr \left[\mathbf{R}^T \left(F_D \cos AoA - F_L \sin A0A \right) \right]_{\gamma, \dot{\gamma}=0} [-\hat{e}_x] \quad \text{(D.13)}$$

$$\vec{F}_N \approx \frac{1}{2}\rho_f \int_0^R r^2 c(r) dr *$$
$$\left[\mathbf{R}^T \sum_{i=1}^{2} \left(\frac{\partial C_D V^2}{\partial \gamma^{(i)}} \sin AoA + C_D V^2 \frac{\partial \sin AoA}{\partial \gamma^{(i)}} + \frac{\partial C_L V^2}{\partial \gamma^{(i)}} \cos AoA + C_L V^2 \frac{\partial \cos AoA}{\partial \gamma^{(i)}} \right) \gamma^{(i)} \right]_0$$
$$+ \frac{1}{2}\rho_f \int_0^R r^2 c(r) dr \left[\frac{\partial \mathbf{R}^T}{\partial \gamma} \left(F_D \sin AoA + F_L \cos AoA \right) \right]_{\gamma, \dot{\gamma}=0} \gamma[-\hat{e}_z]$$
$$+ \frac{1}{2}\rho_f \int_0^R r^2 c(r) dr \left[\mathbf{R}^T \left(F_D \sin AoA + F_L \cos AoA \right) \right]_{\gamma, \dot{\gamma}=0} [-\hat{e}_z] \quad \text{(D.14)}$$

where

$$\frac{\partial \sin AoA}{\partial \gamma^{(i)}} = \cos AoA \frac{\left(\frac{\partial v_z}{\partial \gamma^{(i)}} v_x - \frac{\partial v_x}{\partial \gamma^{(i)}} v_z \right)}{V^2} \quad \text{(D.15)}$$

$$\frac{\partial \cos AoA}{\partial \gamma^{(i)}} = -\sin AoA \underbrace{\frac{\left(\frac{\partial v_z}{\partial \gamma^{(i)}} v_x - \frac{\partial v_x}{\partial \gamma^{(i)}} v_z \right)}{V^2}}_{\frac{\partial AoA}{\partial \gamma^{(i)}}} \quad \text{(D.16)}$$

The aerodynamic pitching moment is linearized by

$$\vec{M}_y \approx \frac{1}{2}\rho_f \int_0^R c(r)\, r^2 \\ * \left[\mathbf{R}^T C_m V^2 X_{CP} + \frac{\partial \mathbf{R}^T}{\partial \gamma} C_m V^2 X_{CP}\, \gamma\right] \\ + \left[\mathbf{R}^T \sum_{i=1}^{2} \left(\frac{\partial C_m}{\partial \gamma^{(i)}} V^2 X_{CP} + C_m \frac{\partial V^2}{\partial \gamma^{(i)}} X_{CP} + C_m V^2 \frac{\partial X_{CP}}{\partial \gamma^{(i)}}\right) \gamma^{(i)}\right]_{\gamma,\dot{\gamma}=0} dr[\hat{e}_y] \quad \text{(D.17)}$$

where

$$\frac{\partial C_m}{\partial \gamma^{(i)}} \\ \frac{\partial C_L}{\partial AoA}\frac{\partial AoA}{\partial \gamma^{(i)}}\cos AoA + C_L \frac{\partial \cos AoA}{\partial \gamma^{(i)}} + \frac{\partial C_D}{\partial AoA}\frac{\partial AoA}{\partial \gamma^{(i)}}\sin AoA + C_D \frac{\partial \sin AoA}{\partial \gamma^{(i)}} \quad \text{(D.18)}$$

$$\frac{\partial V^2}{\partial \gamma^{(i)}} = 2\left(v_x \frac{\partial v_x}{\partial \gamma^{(i)}} + v_z \frac{\partial v_z}{\partial \gamma^{(i)}}\right) \quad \text{(D.19)}$$

$$\frac{\partial X_{CP}}{\partial \gamma^{(i)}} = \frac{c(r)}{4}\frac{AoA}{|AoA|}\frac{\partial AoA}{\partial \gamma^{(i)}} \quad \text{(D.20)}$$

The rotational damping moment is then linearized via

$$\vec{M}_{rd} = \frac{1}{8}\rho_f C_{rd} \int_0^R (|x_{le}|x_{le}^3 - |x_{te}|x_{te}^3)\, dr \\ * \left[\mathbf{R}^T \omega_y|\omega_y| + \frac{\partial \mathbf{R}^T}{\partial \gamma}\omega_y|\omega_y|\gamma + \mathbf{R}^T \sum_{i=1}^{2}\left(\frac{\partial \omega_y}{\partial \gamma^{(i)}}|\omega_y| + \frac{\omega_y^2}{|\omega_y|}\frac{\partial \omega_y}{\partial \gamma^{(i)}}\right)\gamma^{(i)}\right]_{\gamma,\dot{\gamma}=0} \hat{e}_y \quad \text{(D.21)}$$

Lastly, added mass terms are linearized as

$$\vec{F}_{z,am} \approx -\int_0^R \mathbf{R}^T[a_z r\lambda_z(r) + \dot{\omega}_y \lambda_{zw}(r)]dr\, \hat{e}_z \\ -\int_0^R \left[\frac{\partial \mathbf{R}^T}{\partial \gamma}[a_z r\lambda_z(r) + \dot{\omega}_y\lambda_{zw}(r)]\gamma + \mathbf{R}^T \sum_{i=1}^{3}\left(\frac{\partial a_z}{\partial \gamma^{(i)}} r\lambda_z(r) + \frac{\partial \dot{\omega}_y}{\partial \gamma^{(i)}}\lambda_{zw}(r)\right)\gamma^{(i)}\right]_0 dr\, \hat{e}_z \quad \text{(D.22)}$$

$$\vec{M}_{y,am} \approx -\int_0^R \mathbf{R}^T[a_z r\lambda_{zw}(r) + \dot{\omega}_y\lambda_w(r)]dr\,\hat{e}_y$$
$$-\int_0^R \left[\frac{\partial \mathbf{R}^T}{\partial\gamma}[a_z r\lambda_{zw}(r) + \dot{\omega}_y\lambda_w(r)]\gamma + \mathbf{R}^T\sum_{i=1}^{3}\left(\frac{\partial a_z}{\partial\gamma^{(i)}}r\lambda_{zw}(r) + \frac{\partial\dot{\omega}_y}{\partial\gamma^{(i)}}\lambda_w(r)\right)\gamma^{(i)}\right]_0 dr\,\hat{e}_y \tag{D.23}$$